Spring 2022

sUAS and Deep Learning for High-Resolution Monitoring of Tidal Marshes in Coastal South Carolina

Grayson R. Morgan

sUAS and Deep Learning for High-Resolution Monitoring of Tidal Marshes in Coastal South Carolina

by

Grayson R. Morgan

Bachelor of Science
Brigham Young University, 2018

Master of Science
University of South Carolina, 2020

Submitted in Partial Fulfillment of the Requirements

For the Degree of Doctor of Philosophy in

Geography

College of Arts and Sciences

University of South Carolina

2022

Accepted by:

Cuizhen Wang, Major Professor

Michael E. Hodgson, Committee Member

Zhenlong Li, Committee Member

Steven R. Schill, Committee Member

Tracey L. Weldon, Interim Vice Provost and Dean of the Graduate School

DEDICATION

I dedicate this work to the people who have made this happen. This includes but is not limited to: My wife, Lindsey; my children, Evelyn, Johnny, and Lola; numerous other family members; and most importantly my God.

ACKNOWLEDGEMENTS

This page would be substantially longer than a page if I could acknowledge all who have been instrumental in this process. I want to especially thank my family for their support and love. I want to especially thank Dr. Wang who has been there every step of the way of the dissertation and was so willing to help and provide guidance. Special Thanks to Dr. Hodgson, Dr. Li, and Dr. Schill for their insightful comments and direction. Also, special thanks to my dad, Daniel R. Morgan, for being my flight crew and essentially getting this dissertation complete with me. I couldn't have done it without him. Thank you to all who have studied these things before me and made it possible to continue. It would be a mistake to not thank the entire geography department at UofSC who have made me feel home the last few years. Thank you all!

ABSTRACT

Tidal marshes are dynamic environments, now more than ever threatened by both natural and anthropogenic forces. Best practices for monitoring tidal marshes, as well as the environmental factors that affect them, have been studied for more than 40 years. With recent technological advances in remote sensing, new capabilities for monitoring tidal marshes have emerged. One of these new opportunities and challenges is hyper-spatial resolution imagery (<10 cm) that can be captured by small unmanned aerial systems (sUAS). Aside from enhanced visualization, structure-from-motion (SfM) technology can derive dense point clouds from overlapped sUAS images for high resolution digital elevation models (DEMs). Furthermore, Deep Learning (DL) algorithms, patterned after the brain's neural networks, provide effective and efficient analysis of mass amounts of pixels in high-resolution images. In this dissertation, I seek to apply these developing geospatial technologies—sUAS and DL—to map, monitor, and model marsh vegetation. First, sUAS and coastal vegetation related literature was extensively reviewed to provide a secure foundation to build upon. Second, an above ground biomass (AGB) model of the tidal marsh vegetation *Spartina Alterniflora* was developed using high resolution sUAS imagery to assess marsh distribution and healthiness in the estuary. We determined that the best RGB-based index for mapping S. Alterniflora biomass was the Excess Green Index (ExG), and using a quadratic relationship we achieved an R^2 of 0.376. Third, with a time series of sUAS missions, tidal marsh wrack was monitored before and after a hurricane event to map and monitor its

short- and long-term effects of tidal wrack deposition on vegetation. sUAS proved to be an exceptionally capable tool for this study, revealing that 55% of wrack stayed within 10 m of a water body and wrack may persist for only 3-4 months over the same location after a hurricane event. Finally, deep learning remote sensing techniques were applied to county-wide NAIP aerial imagery to map Land Use/ Land Cover (LULC) changes of Beaufort County, South Carolina from 2009 to 2019, and to assess if and why marsh losses or gains may have occurred around the county from coastal development. We discovered that the DL U-net classifier performed the best (92.4% overall accuracy) and the largest changes in the county have come by way of forest loss for urban growth (7,000 ha), which will impact the coastal marshes over time. This dissertation advances the theoretical and application-based use of sUAS and DL to benefit application driven GIScientists and coastal managers in the coastal marsh realm to mitigate future negative impacts and expand our understanding of how we can protect such majestic environments.

TABLE OF CONTENTS

LIST OF TABLES

LIST OF FIGURES

LIST OF ABBREVIATIONS

AGB ..... Above Ground Biomass

AOI ..... Area of Interest

CHM ..... Canopy Height Model

DL ..... Deep Learning

GCP ..... Ground Control Points

GNSS ..... Global Navigation Satellite System

LULC ..... Land use/Land cover

ML ..... Machine Learning

NIWB ..... North Inlet Winyah Bay

RF ..... Random Forest

RGB ..... Red, Green and Blue

sUAS ..... small unmanned aerial system

SVM ..... Support Vector Machine

CHAPTER 1

INTRODUCTION

South Carolina is home to approximately 30% of all salt marsh extent along the Atlantic coast of the United States, totaling about 350,000 acres (Morganello and Rose, 2013). These extensive marsh habitats provide a variety of ecosystem services, such as filtering out toxins and sediment, slowing and absorbing storm surges, and serving as nursery grounds for a variety of animal species. They also provide valuable resources for commercial entities, as 75% of animals harvested as seafood spend at least some of their lifetime in the waters in and around the salt marshes. As ecotourism grows in the state, marsh habitats also provide scenic locations for recreational kayakers and boaters. Arguably most importantly, the areas serve as carbon sinks, mitigating some of the effects of increased CO_2 in the atmosphere.

Some studies have sought to provide quantitative valuation of tidal marshes, though this can be difficult due to their complex nature. According to Purcell et al., (2020), South Carolina salt marshes and coastal wetlands provide services in the four ecosystem service categories: provisioning, regulating, cultural, and supporting. Each of these categories, though not all marketed services, provide valuable resources to coastal communities. For example, the salt marshes serve as nursery habitat to many species, especially shrimp. South Carolina's commercial fishing industry that relies upon these environments and generates $42 million dollars annually to the state economy (Willis and

Straka, 2016). The regulating services provided by the salt marshes (like shoreline stabilization and wave attenuation) are all valued slightly differently. Water quality enhancement by salt marshes were estimated to range from $99 to $5,551 per acre depending on the treatment in Louisiana (Breaux et al.,1995). A study in California estimated that the value of sequestering carbon by salt marshes would be between $56 and $1,861 per hectare per year (Ballard et al., 2016). While both of these measures were not developed for South Carolina, they are an indication that the value of South Carolina's salt marsh is also high. Tourism also contributes to a cultural tourism revenue of approximately $9 billion annually (Purcell et al., 2020). The value of these ecosystems, though sometimes difficult to quantify, are apparent in their contribution to the economy in various ways.

It has been reported that South Carolina has lost 27% of its original wetlands in the past 250 years (State Wetland Protection, 2008). Despite our current understanding of the benefits coastal wetlands— especially marshes— provide, marshes continue to be negatively affected by anthropogenic influences. Extreme weather events and sea level rise threaten other impacts as well. Consistent, flexible, and effective monitoring techniques are essential for obtaining essential knowledge of how these systems change over time and how they can be protected in the Anthropocene. Traditional *in situ* methods for monitoring tidal marsh, though effective, require significant time, human, and technological resources that can strain government agencies and coastal managers. Monitoring tidal marshes using satellite and aerial remote sensing has been extensively studied to reduce the amount of *in situ* resources required to observe changes in such a dynamic environment (Hardisky et al., 1986; Jensen et al., 1993; Phinn et al., 1998;

Leahy et al., 2005; Tiner et al., 2015; Mo et al., 2019). However, difficulties with tides, cost, data size, and marsh vegetation phenology hinder our ability to use the traditional remote sensing methods for continuous monitoring. Furthermore, available data are often captured for a different purpose or have lower temporal or spatial resolutions than are ideal for studies related to the marsh environment. (Tiner et al., 2015).

Rapidly developing and application driven geospatial technologies— specifically small unmanned aerial systems (sUAS) remote sensing and deep learning image classification techniques—have improved the opportunities for effective and efficient tidal marsh monitoring. While sUAS have a rather robust military pedigree, their use by civilians began more recently (Hardin and Jensen, 2011; Hugenholtz et al., 2012). Deemed a 'personal remote sensing device,' sUAS are considered an on-demand remote sensing tool with adjustable temporal and spatial resolutions (Jensen, 2018). The applications of such flexible tools have been diverse, and coastal wetland applications are on the rise (Terwilliger et al., 2015; Bhardwaj et al., 2016; Hugenholtz et al., 2013; Jensen, 2018; Klemas, 2015; Koh and Wich, 2012). A subsection of Machine Learning (ML), Deep Learning (DL) is able to perform artificial intelligence functions with extensive training resources. The recent popularity and success of DL in other disciplines and applications, including speech recognition (Hinton et al., 2012) and medical image recognition (Litjens et al., 2017), has led to the rise of its use in remote sensing applications (Zhu et al., 2017; Liu et al., 2018; Ma et al., 2019; Yin et al., 2020; Pouliot et al., 2019; Li et al., 2021; Pashaei et al., 2020). With the addition of DL technologies to many GIS software suites, such as ArcGIS Pro and ERDAS Imagine, image classification using /DL has become more accessible than ever. These recent technological

advancements have enhanced our ability to monitor coastal wetlands within the spatial, temporal and social dimensions of coastal management (Clark, 2000; SCDHEC, 2019).

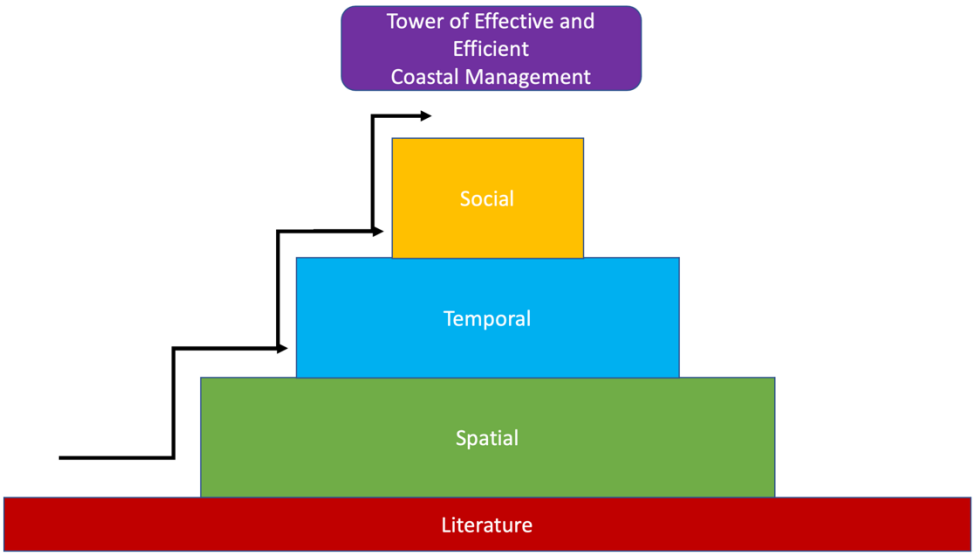

Figure 1.1. Effective and Efficient Coastal Management is made up of many dimensions. The three investigated in this dissertation are spatial, temporal, and social.

This dissertation is centered on applying the aforementioned advancing geospatial technologies to monitor and assess coastal wetlands within the spatial, temporal and social dimensions of coastal management (Figure 1.1). In chapter two, I reviewed the sUAS remote sensing and coastal vegetation related literature to determine best practices and important considerations for planning wetland monitoring missions. Chapter 2 serves as a foundation upon which we can build the tower of coastal management and monitoring. Chapter three addresses the spatial element of coastal management using sUAS to map the spatial distribution of *Spartina Alterniflora* (i.e., smooth cordgrass) biomass in a coastal tidal marsh system. In chapter four, I combined the temporal and spatial elements as I once again used sUAS to monitor a coastal tidal marsh system

monthly over a one-year period to assess the positive and negative impacts of wrack, as well as determine how a hurricane event impacts wrack spatial distribution over time. The spatial and temporal elements were combined with a social dimension (land use change) in chapter five as a DL classifier is compared with other ML classifiers to determine the best method for detecting changes in LULC for an entire coastal county in South Carolina and its impact to marsh environment over a period of 10 years. Finally, chapter fix summarizes the previous chapters and provides concluding remarks. Tied together by a string of developing high resolution image-oriented geospatial technologies and a staircase of cumulative coastal management elements, the six chapters of this dissertation are organized and structured to establish more efficient and effective ways to monitor coastal tidal marsh systems.

CHAPTER 2

UNMANNED AERIAL REMOTE SENSING OF COASTAL VEGETATION: A REVIEW[1]

[1] Morgan, G. R., Hodgson, M. E., Wang, C., & Schill, S. R. (2022). Unmanned aerial remote sensing of coastal vegetation: A Review. *Annals of GIS*, 1–15. https://doi.org/10.1080/19475683.2022.2026476. Reprinted with permission from the publisher

2.1. Introduction

Coastal wetlands are highly productive environments with a multitude of ecological and economic benefits (Mehvar et al., 2018; Peterson and Turner, 1994). For example, coastal wetlands serve as buffers to storms and floods, and the vegetation plays a large role in protecting people and infrastructure (Narayan et al., 2017). Furthermore, coastal wetlands also sequester carbon and filter runoff and upstream water from the pollutants they carry (Loomis and Craft, 2010; Ballard et al., 2016). Economically, commercial fishing industries rely heavily on coastal wetlands as they provide critical nursery and breeding grounds for many harvested species, and there is an increasing recreational and tourism sector by those seeking to enjoy the unique beauty wetlands provide (Purcell et al., 2020). Occupying the space between the land and sea, the constant pressure by a variety of forces, including aeolian, fluvial, flood hazards, and climate change, make coastal wetlands some of the most dynamic environments in the world. As a result, efforts to monitor and map these areas has taken precedence for many stakeholders. The critical ecological role that coastal wetlands provide, coupled with the dynamic environment in which they exist, necessitates frequent monitoring and study.

Traditional field methods of *in situ* monitoring in coastal wetlands are effective but often difficult due to accessibility and resources requirements. Remote sensing methods can be used to alleviate these concerns, though two challenges remain. The first challenge involves capturing imagery at an appropriate spatial resolution to resolve the phenomenon to be mapped and visibly interpreted from the imagery. The second challenge is acquiring imagery with adequate temporal resolution to properly describe the

phenomenon of interest while avoiding unwanted environmental conditions that can negatively affect the imagery. Current satellite and manned aircraft missions can provide moderate to high spatial resolution imagery at fairly high temporal resolutions. Satellite platforms with moderately-fine spatial resolutions (e.g., 1 m) are on set temporal orbital paths, typically with one overpass in the late morning and revisits every two to three days (Liu and Hodgson, 2016). Cloud cover, a challenge that specifically related to temporal resolution, can be problematic and obscure coastal environments when capturing imagery using optical satellites. Commercial high-resolution imagery is also too expensive for long-term monitoring of coastal wetlands.

Recent developments in small Unmanned Aerial Systems (sUAS) permit on-demand data acquisition and help fill the spatial and temporal resolution voids that often exist when using *in situ* data for calibrating satellite or manned-aircraft remote sensing imagery. These newer remote sensing systems can be cost efficient, deployed when circumstances require or allow, and capture very fine (<10 cm) spatial resolutions. However, they also come with many limitations, such as battery capacity impacting flight time and corresponding image area, as well as flight regulations from the Federal Aviation Administration (FAA), state and local authorities (Hodgson and Sella-Villa, 2021).

In this chapter, we review the opportunities for sUAS use as an emerging remote sensing approach to assessing and monitoring coastal wetland vegetation. Other recent review studies have highlighted the specific uses of sUAS in meeting operational requirements for coastal wetlands of the Great Lakes, wetland restoration, fluvial remote sensing and for monitoring the spread of water hyacinth (White et al., 2020; Ridge and

Johnston, 2020; Rhee et al., 2017; Datta et al., 2021). We are aware of one other review of the opportunities of using sUAS-based remote sensing of coasts and wetlands published in 2015 by Klemas (Klemas, 2015). This manuscript focuses on reviewing literature published more recently. The larger body of peer-reviewed literature related to sUAS and coastal wetland vegetation did not exist until after 2015.

Through an in-depth review of the most recent sUAS and coastal vegetation related literature, we present the current state of sUAS uses for coastal vegetation remote sensing, the challenges encountered in each study, and a way forward to improve research methods when using these promising new tools. The article proceeds with Section two describing the methods used to obtain the literature base and general trends in the research. Section three presents specific lessons and strategies for using sUAS for coastal wetland research. Section four discusses some future directions for research, while section five summarizes and concludes our thoughts with questions to consider moving forward.

2.2. Collection of Literature

To assess the uses of sUAS in coastal vegetation research, a Web of Science search was conducted using the terms “unmanned aerial,” “coastal,” and “wetland vegetation” (15 articles identified). A second search used the terms “unmanned aerial,” “coastal,” and “marsh vegetation” to enhance the literature base we investigated (12 additional articles identified). For the purposes of this study, “unmanned aerial” represented any use of an sUAS in an article, including if the sUAS only provided supporting data for the study. The word “coastal” was critically important here, and for

the purposes of this study, represented the coast of any body of water (i.e., fresh or salt water), including a lake, sea, or ocean. Since wetlands are found all over the world in a variety of environments, it was important to clarify our geographic extent of interest. The words “wetland vegetation” or “marsh vegetation” gave focus to mapping and monitoring vegetation rather than topography or another phenomenon. These five words, when placed together in a search, produced a total of 25 distinct articles. We examined each abstract to verify the article related to our goals. Conference proceedings and other review articles were not included in this review.

Of the original 25 studies identified using Web of Science, a few were review papers describing the application of sUAS in a coastal wetland environment that did not pertain to remote sensing of vegetation characteristics. Some articles included a short discussion or mention of sUAS in a coastal wetland, but then focused on other topics. For example, some studied sUAS to investigate hydrology in a coastal environment to monitor tidal channel surface velocities or determine water budgets (Pinton et al., 2020; García-López et al., 2018). Other studies described methods (e.g., structure from motion or SfM) for mapping terrain under dense vegetation from the point cloud (Meng et al., 2017). Although vegetation was addressed, it was not the focal point of the study. These articles were also removed from our literature base. Another study’s objective was identifying nesting waterbirds and was therefore removed (Barr et al., 2018). After our thorough examination of all 25 articles, only 20 articles remained. The 20 selected articles focused on coastal wetland vegetation per our qualifications above. We reviewed each article thoroughly to ascertain detailed information on where and how each study

was performed; platform and sensor requirements; challenges faced; results; accuracy; and general characteristics of the products derived from the sUAS imagery.

Vegetation-related goals of each study could be categorized into three general objectives: mapping spatial distribution of vegetation or species, monitoring vegetation health (e.g., estimating biomass or mapping photosynthetically active vegetation), and quantifying vegetation structural characteristics. The number of articles focused on the use of sUAS and coastal vegetation has increased steadily (Figure 2.1). These articles were published in a variety of journals, with *Remote Sensing* (n = 6) and the *International Journal of Remote Sensing* (n = 2) including the highest number of related articles. Twelve other journals have a single publication with relevance to coastal vegetation remote sensing with sUAS. The geographic study areas described in the publications were widely dispersed around the world, although a very high percentage (80%) of the research was conducted in the United States of America. Based on these results, an interdisciplinary and growing international interest in the use and development of sUAS resources for mapping and monitoring coastal vegetation. While only three studies that fit our criteria had been published in the year 2021 (as of the writing of this article), it is expected that there will be many more to come. Figure 2.1 does not include Klemas (2015), which is a review article concerning the beginning of sUAS use for coastal vegetation.

Many different sUAS configurations (i.e., platform types and sensor types), calibration techniques, products, and methods of analysis were used in the literature base. The most common platforms can be assigned one of two categories: fixed wing (airplane-like) or multicopter (helicopter-like). A variety if sensor types were also used, including

the nearly ubiquitous Red-Green-Blue (RGB) cameras, multispectral cameras, hyperspectral sensors, spectroradiometers, and LiDAR sensors. Two software packages, Pix4D Mapper (n = 5) and Agisoft Photoscan/Metashape (n = 11), were most often used for transforming the images collected by sUAS into standard products, including orthomosaics, digital elevation models (DEMs), and vegetation index maps.

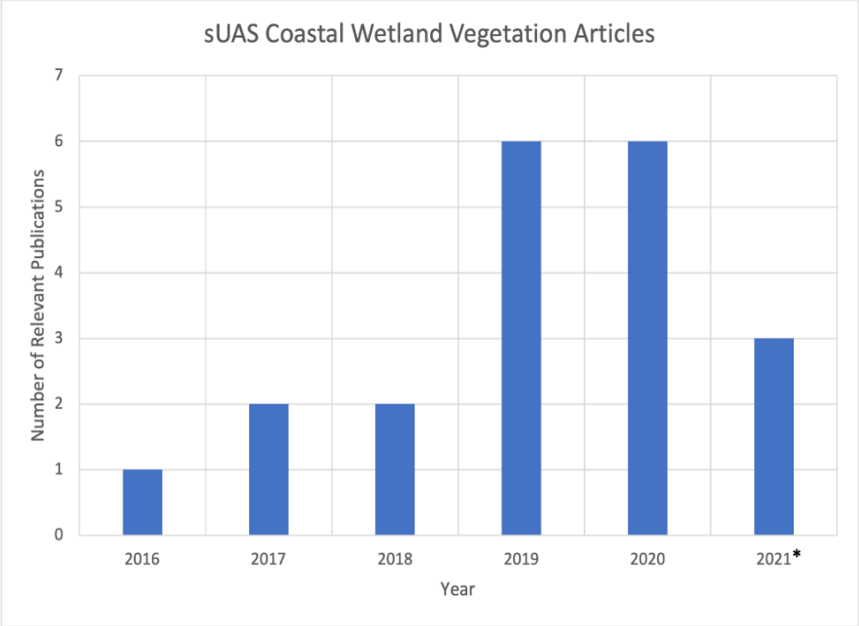

Figure 2.1. Number of sUAS Coastal wetland vegetation articles published by year. *2021 numbers were accurate as of July 13, 2021, and thus, do not include publications after July 13.

2.3. sUAS Remote Sensing for Coastal Wetlands

2.3.1. Benefits of sUAS Remote Sensing

Several benefits of employing sUAS for coastal vegetation mapping were evident in the literature base used for this review. The cost effectiveness of using a sUAS for coastal vegetation research and monitoring was well documented (Marcaccio et al., 2016;

Johnson et al., 2020; Durgan et al., 2020b; Haskins et al., 2020; Taddia et al., 2021). While initial set up costs can be expensive, the reusability of the Global Navigation Satellite Systems (GNSS) equipment, sUAS, and ground control point (GCP) targets suggest that future sUAS mission costs would be limited, or costs would decrease over time. The commonly used image processing software can be expensive as well, although freeware options are available to make sUAS remote sensing possible for coastal managers and researchers with budgetary constraints (Johnson et al., 2020). The use of sUAS can also significantly reduce time spent in the field. For the study area described in (Marcaccio et al., 2020), traditional *in situ* field work for a wetland would take two researchers 6 to 8 days. However, acquiring the aerial images using sUAS only took 6 to 24 hours, depending on the type of sUAS. Durgan et al. (2020b) shared a similar sentiment, offering that sUAS are more efficient than traditional field surveys for tracking wetland restoration progress. The sUAS surveys took less than one hour to complete while the field survey required five days with comparable accuracy. Time spent in the field gathering data using sUAS methods and in situ methods will all depend on the area, number of sites, and workload, and these examples may be extreme. Nevertheless, the literature base has shown that financial and time-related costs can be significantly reduced when monitoring coastal wetland vegetation with a sUAS.

Using sUAS as an on-demand remote sensing platform can help overcome many logistical problems related to the dynamics of a coastal wetland environment (Farris et al., 2020; Doughty et al., 2021). For example, tidal cycles make planning and operating missions difficult, especially when weather on coastlines can be so variable. Many manned aerial imagery programs, such as the National Agriculture Imagery Program

(NAIP), capture imagery for leaf on conditions, but do not consider the tidal cycle and other environmental conditions when determining flight times. Other impactful natural elements, like cloud cover, precipitation and previous rainfall events can be avoided with sUAS mission flexibility. The ability to collect repeat datasets over the same area makes sUAS an appropriate tool for monitoring dynamic ecosystems, invasive species, and short-term events (Abeyshinghe et al., 2019; Pinton et al., 2020; Dai et al., 2020). sUAS are an on-demand remote sensing option, capable of flying over small coastal areas when the elements align to collect the best possible imagery.

There were well mentioned benefits to using sUAS for each type of coastal wetland environment as well. For example, when mapping submerged aquatic vegetation (SAV), sUAS can provide a footprint larger than other monitoring methods (i.e., from *in situ* methods in a boat), and larger areas can be mapped more efficiently (Brooks et al., 2019). sUAS-borne LiDAR sensors are able to gather more ground returns and penetrate the vegetation more effectively than manned airborne LiDAR missions due to the lower flight altitudes (Pinton et al., 2020). High spatial resolution imagery provided by sUAS can be used for generating training samples in many environments where non-invasive and non-destructive methods are required (Haskins et al., 2021). Finally, sUAS derived datasets can serve as important supplementary information for making effective decisions and modelling (Zhou et al., 2018; Broussard et al., 2020). sUAS fill a scale niche that was previously difficult to fill. Multi-scale remote sensing is used to understand ecological processes at different scales – satellite (global, regional, national) and sUAS (local). They work complementary with each other. Remote sensing data can most effectively be used when you join multiple scales together.

2.3.2. sUAS Platforms for Coastal Wetland Vegetation Research

The chosen sUAS platform used in each study is important because factors such as payload capacity, flight time, stabilization, cost, and maintenance are a function of the platform itself. In all studies included in our review, the two largest categories of sUAS platforms were fixed wing and multicopter. Of the 20 articles included in the review, seven used fixed wing aircraft, eleven used multicopter aircraft, and two used both. Fixed wing aircraft, known for their ability to sustain flight for an extended period of time, have been used for a multitude of applications in coastal environments (Barr et al., 2018). In a study comparing fixed wing and multicopter aircraft for environmental mapping applications, Boon et al. (2017) found that fixed wing aircraft were more cost efficient, required less maintenance, and allowed increased flight time. Of the nine studies that used fixed wing aircraft, five used a version of a Sensefly eBee aircraft (Ebee). Fixed wing aircraft can be beneficial for monitoring larger areas of coastal wetland vegetation due to their increased flight times. Our review showed the flight area of the fixed wing aircrafts used for this particular environment ranged from smaller areas of about 0.292 km^2 (Dale et al., 2020) to larger areas up to 2.85 km^2 (Marcaccio et al., 2020). Figure 2.2 shows the relationship between flight altitude (above ground level) and the corresponding mapped area for fixed wing aircraft and multicopters for coastal wetland mapping.

Boon et al. (2017) suggested, based on their analysis, that multicopters could maintain a higher payload and offer better stabilization. In addition, multicopters can control speed much more effectively than fixed-wing sUAS. They offer the ability to fly sufficiently slow to capture imagery with more complex sensors, like hyperspectral sensors, especially when vegetation is submerged in a wetland. These two factors

contributed to what the authors referred to as a more accurate environmental mapping option. Thirteen studies (plus the two studies that used both sUAS aircraft types) used a multicopter aircraft, with a mix of octocopters, hexacopters, and quadcopters. The most common (8 articles) multicopter aircraft brand was Da-Jiang Innovations (DJI). Multicopter sUAS are excellent for capturing imagery of smaller areas. Most of the studies were conducted over similarly small study areas, below 100 ha or 1 km2 (Figure 2.2). Multicopters are also beneficial in areas like coastal salt marshes where it can be difficult to find adequate space to launch/recover a fixed wing aircraft (Broussard et al., 2020). The typical payload for each sUAS was only one sensor, however a Bergen hexacopter was used by Brooks et al. (2019) to carry a heavier payload of two sensors.

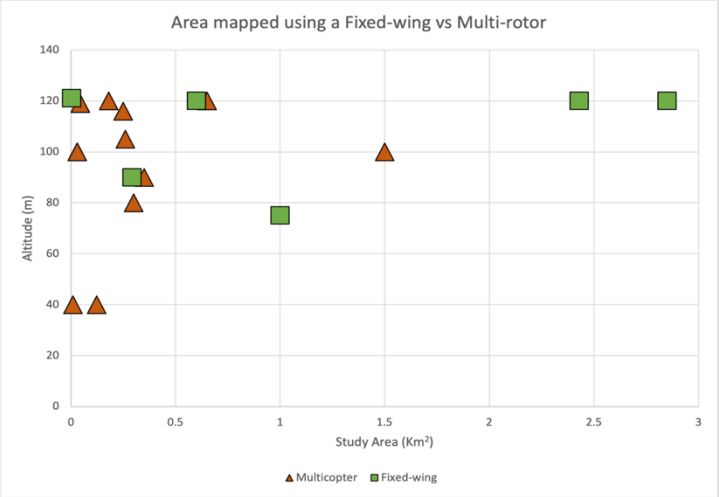

Figure 2.2. Platform graphed by altitude and study area. Graph only includes article information if both study area and altitude were disclosed somewhere in the article. If multiple flights were flown or a range of altitudes were used, the highest altitude was used for graphing.

In a study comparing the capabilities of an eBee fixed wing aircraft, a DJI quadcopter, and aerial imagery in a coastal marsh environment, Marcaccio et al. (2016) found that multicopter aircraft could capture about 16 hectares per flight, while the fixed

wing aircraft could capture 94 hectares per flight when flying at the same altitude and environmental conditions. Although the study area size is a function of altitude, battery capacity, and camera lens this study's results suggests fixed wing aircraft could cover six times the area of a multicopter. Upon further review, the battery capacity was certainly a factor, although the manual operation of the multicopter sUAS and autopilot operation of the fixed wing eBee aircraft may have been a factor. Nevertheless, figure 2.2 does support the notion that fixed wing aircraft should be considered for study areas with greater extents, as authors have been doing. In summary, both multicopter and fixed wing sUAS serve as useful remote sensing platforms in estuary/coastal wetland sUAS research depending on the application, study area size, and payload required. Multicopter aircraft are favored for image quality and stability, while fixed wing aircraft are ideal for larger flight areas.

2.3.3. sUAS Sensors for Coastal Wetland Vegetation Research

Studies in coastal wetland environments included a diverse group of payloads (Figure 2.3). However, 15 of the 20 studies included at least one RGB camera for vegetation observation and analysis (Durgan et al., 2020b; Lishawa et al., 2017; Rupashinghe et al., 2018). Many studies (n= 10) incorporated a near infrared (NIR) band, with the band ranging in wavelength (depending on the sensor) between 770-850 nm (Abeysinghe et al., 2019; Broussard et al., 2020). The red edge (RE) band was included on some of the sensor systems with wavelengths between 707 and 727 or 730 and 740 nm. The RE band was not commonly used in analysis, however (Farris et al., 2020; Doughty and Cavanaugh, 2019). The most common multispectral cameras used were the Micasense Red Edge-M or MX sensor, the Parrot Sequoia sensor, or the Mapir Survey 3

sensor (Figure 2.4). Each of these sensors and their NIR and RE bands contributed to improved model or classification accuracy when used to generate vegetation indices like NDVI (Abeyshinghe et al., 2019; Doughty and Cavanaugh, 2019; Samiappan et al., 2016). Broussard et al. (2020) used modified RGB cameras with filters to capture a false color image. Both RGB and Multispectral cameras offer relatively inexpensive opportunities to map and monitor coastal wetland vegetation. Even the least expensive option, RGB camera derived imagery was used to go beyond visual interpretation and provide RGB-based vegetation indices to improve classifications and mapping (Johnson et al., 2020). Haskins et al. (2021) recommended the collection of NIR in addition to RGB imagery because of the added benefits for classifying vegetation.

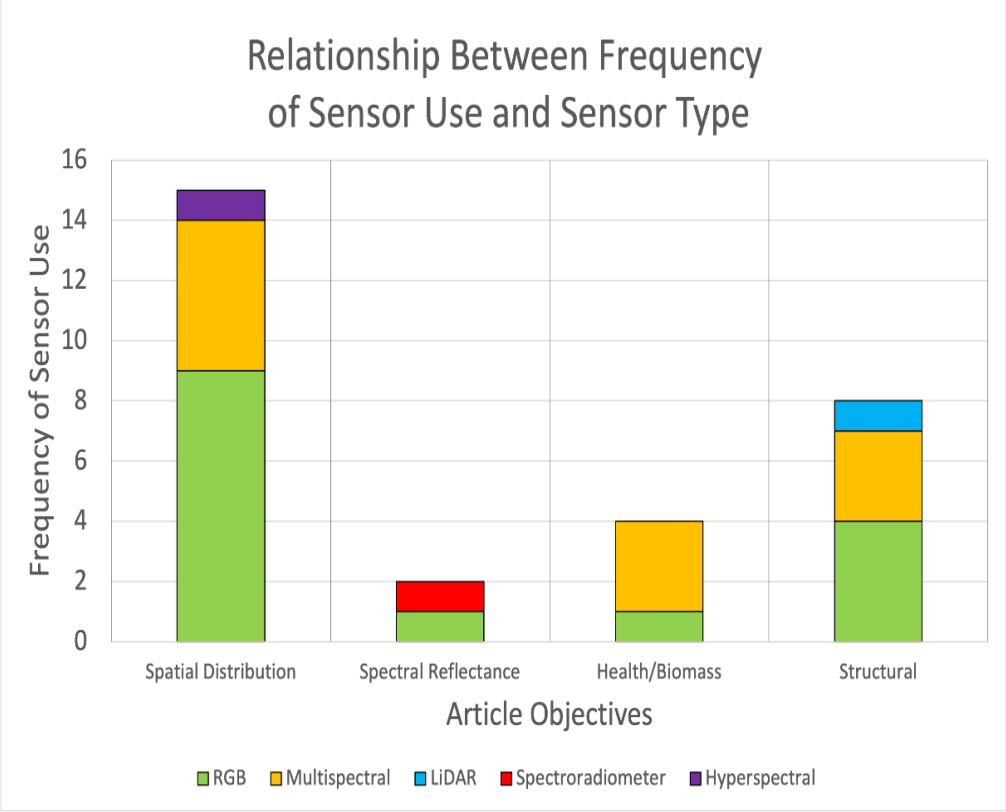

Figure 2.3. Relationship between article objects, sensor type, and the sensor type's frequency of use. Some studies included multiple sensors.

Cao et al. (2018) used a Cubert UHD 185 hyperspectral sensor was used to distinguish between different mangrove species. This sensor is able to capture wavelengths from 450 nm to 998 nm in up to 138 spectral bands. The authors discovered that using hyperspectral data with very high spatial resolution, along with DEMs, provided the best mangrove classifications with an overall accuracy (OA) of 89.55%. A variety of spectroradiometers were attached to an sUAS by Brooks et al. (2019). SAV was detected using spectroradiometers ranging from 190 nm to either 800, 1000 or 1100nnm, with a 1.5 nm spectral resolution. These sensors were successfully used to derive vegetation curves, even with the vegetation submerged, though the radiance values are not as strong as signals from a boat or the vegetation out of the water (Brooks et al., 2019). The authors also included a Tetracam multispectral camera as well with six bands of 490, 530, 550, 600, 680, and 720 nm.

Figure 2.4. A DJI Matrice 100 with a Micasense Red Edge-M multispectral camera attached.

Pinton et al. (2020) conducted a study in a salt marsh in Georgia, USA using a sUAS-borne LiDAR sensor, SfM-derived point cloud from RGB images and a combined dataset to map coastal marsh vegetation structural characteristics. Authors discovered that sUAS-borne LiDAR outperformed the RGB-derived data and the combined dataset of LiDAR returns and the sUAS SfM-derived point cloud. Furthermore, sUAS-borne LiDAR was shown to overcome some shortcomings found in traditional higher-altitude manned-aircraft borne LiDAR for coastal wetlands. Applying less-commonly used sensors and cameras with practical applications, such as LiDAR and hyperspectral sensors, remain an important area of future study for coastal wetlands.

2.3.4. Flight Parameters for Coastal Wetland Vegetation Research

Ideal flight parameters for sUAS remote sensing of coastal wetlands are dependent upon the type of vegetation being mapped. For example, remote sensing of salt marsh grasses may require different parameters than a mangrove forest depending on the research question. Examples in the literature base gathered for this review offer insights into best approaches. Durgan et al. (2020a) evaluated the impacts of flight altitude, image overlap, and lighting conditions on various sUAS-imagery derived products (e.g., point clouds, orthomosaics, Digital Terrain Models or DTMs). They found that flight altitude was the most impactful parameter, while image overlap also contributed to a small degree. Flight altitude, as shown in Figure 2.2, varied widely across studies in coastal wetlands but was generally between 70 m above ground level (AGL) and 120 m AGL. (Note: 120 m is the non-waivered FAA legal limit for sUAS operations in the USA.) Increased image overlap impacted the author-designated level 2 products (Canopy height models or CHM and DTMs) the most. For wetland cordgrass height modelling, lower

altitude flights (around 70 m in Durgan et al. 2020a) showed less error than higher altitude flights, while higher altitude flights (around 119 m) reduced vertical error for mangrove canopy modelling. However, it is of note that in one author's experience, lower altitude flights can make it more difficult for photogrammetric processing software to find key points in overlapping imagery. Higher altitude images stich together into orthomosaics better.

Another study investigated ideal parameters for using sUAS to monitor marsh restoration projects (Haskins et al., 2021). While a large portion of the study was focused on investigating topographic changes in restored marshes, one objective was to investigate the required flight altitude for identifying vegetation of different horizontal area sizes. Of the three flight altitudes (10 m, 30 m, and 60 m) flown over a 1 ha marsh area, the authors found 30 m to provide the most accurate classifications when the NIR band was included (Nash-Sutcliffe Efficiency (NSE) coefficient = 0.74). The 10 m (NSE = 0.71) and 60 m (NSE = 0.63) flights were not as accurate, though they only required the use of the RGB bands to reach this accuracy. Flights of 10 m were able to identify high percentages of mid-size and large plants (> 80%) and only 45% of vegetation classified as 'small.' It was more difficult to identify all sizes of vegetation with the imagery provided by flights of 30 m (0.76 cm spatial resolution) and 60 m (about 1.5 cm spatial resolution). The authors suggested the use of 30 m for vegetation recognition because of the amount of area that can be imaged while also providing high spatial resolutions for vegetation recognition.

Other studies offer important notes such as light conditions and tidal effects for consideration when planning missions. For example, Farris et al. (2019) suggested the

collection of imagery during solar noon to reduce shadows, particularly when planning to use the data for a structural study such as salt marsh shoreline recognition. However, sun glint on water in tidal areas is more prominent during this time and can impact imagery as well. Shadows impacted DTM accuracy by restricting the creation of ground points in the generated point cloud (Durgan et al. 2020a).

Flight altitude, overlap, and spatial resolution was determined to be the most influential flight and imagery parameters for generating successful imagery products and eventual interpretation (Rupasinghe et al., 2018). When using visual interpretation, it is also important to reduce shadows during data collection. Water was found to dampen reflectance and impact various products, including a biomass estimation model, so it is important to consider the tidal cycle in order to limit the amount of water in the imagery (Doughty and Cavanaugh, 2019). Collecting multi-temporal images over longer periods of time during similar tidal stages was also suggested.

The spatial resolution of collected imagery is a function of the flight altitude, focal length and sensor width of the camera. A discussion of the focal length and sensor width of different cameras is beyond the scope of this study but is important to note that many cameras used for sUAS remote sensing share similar characteristics. The required spatial resolution of a mission should be dependent upon the minimum mapping unit (MMU), which is driven by the research question. The MMU is determined by the smallest phenomenon to be resolved in the imagery and requires expert knowledge of that particular phenomenon. Surprisingly, the concept of a minimum mapping unit (MMU) was not mentioned in any of the articles in this category. However, Brooks et al. (2019) flew at multiple altitudes and found altitudes of 10 to 20 m could obtain the highest

concentration of reflectance over the study area. While the results from the sUAS produced a weaker spectral response than the data collected via boatside or out of the water methods data collection scales, they were still successful in separating Eurasian watermilfoil (EWM) from other vegetation types. Of the 20 studies focused on the coastal wetland environment, the spatial resolution ranged from 0.8 cm to 32 cm. Rupasinghe (2018) flew at an altitude of 121.92 m and used a canon RGB camera. The authors do not explain why a spatial resolution of 32 cm is used, though the sUAS imagery was used to compare with 1 m and 2 m data as a higher spatial resolution alternative. Higher spatial resolutions can be gathered with those parameters, and more detail from the authors is needed to understand how and why such a coarse resolution was collected. Beyond this outlier, the lowest spatial resolution collected for any study is 13.9 cm. The median spatial resolution, including the outlier, was 4.23 cm and suggests the preference of researchers to map coastal wetland vegetation at spatial resolutions in the 1 cm to 5 cm range.

2.3.5. sUAS Data Correction and Calibration for Coastal Wetland Vegetation Research

Image correction (e.g., radiometric or geometric corrections) is essential for ensuring accuracy of the reflectance value and geolocation of remotely sensed imagery. Any errors introduced in the collection of the images will be propagated through to the imagery products and eventual results. Several studies reviewed and applied various georeferencing and radiometric correction techniques to normalize the sUAS data.

Ground control points (GCPs) were deemed essential to ensuring proper georegistration of the collected sUAS data. Even though more expensive sUAS may

include a high accuracy GNSS, such as those augmented with RTK or PPK, collecting and using a proper number of GCPs is essential to ensuring the data produces the map product accuracy needed for the application. In our review, many articles did not discuss the number of GCPs being used, particularly in the earlier studies. In the 11 articles published from before 2020, only 3 (27%) mentioned that GCPs were used for georeferencing. In contrast, 8 of the other 9 articles published in 2020 and 2021 (89%) mentioned the use of GCPs. The number of GCPs and size of the study area did not show any correlation, indicating a lack of consensus on how many GCPs should be used for different study area sizes in this type of environment (Figure 2.5). The most GCPs collected for any study was 30, while the least amount was 6. In a single study used an eBee plus real time kinematic (RTK) sUAS, researchers collected 6 ground control points over their 29 ha area (Dale et al., 2020).

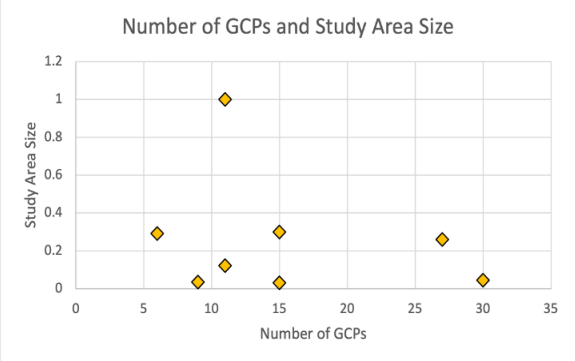

Figure 2.5. Relationship between number of GCPs and study area size for sUAS in coastal wetland research. Only studies indicating the number of GCPs and study area size were included.

Santos Santana et al. (2021) experimented on sUAS flight altitude and ground control points in georeferencing and discovered that accuracy doesn't improve much after

including more than 6 to 8 GCPs per hectare. However, the authors concluded that the number of GCPs and altitude of the aircraft are crucial components to incorporate into mission planning for a successful mission and useable product. Interestingly, Haskins et al. (2021) suggested that two GCPs per hectare is sufficient for high resolution mapping and accuracy did not improve much beyond that threshold. We suggest the number of GCPs per ha relationship should also be selected based on the flight altitude/study area and complexity of the topography. Including GCPs in a wetland environment can be difficult due to the inaccessibility of marshes or height and complexity of the canopy. Solutions to this issue were to select GCPs strategically around the vegetation canopy or use an elevated GCP on a platform to rise above the vegetation canopy (Broussard et al., 2020). While the elevated GCPs remove some of the studied phenomenon from the images, it is a non-destructive method that protects the underlying vegetation.

The primary radiometric correction that was conducted across numerous studies was to transform the raw digital numbers (DNs) collected by the multispectral or hyperspectral cameras into radiance and percent reflectance. Accurate radiometric correction ensures that image data can be compared across collection dates and times and minimizes seamline inconsistencies across image scenes. Changing atmospheric conditions can result in raw DNs for the same objects across scenes to change dramatically, even over just a few minutes. The most common calibration method was to use a radiometric calibration target provided by the camera manufacturer, such as a MAPIR Calibration Target V2 or Micasense red edge panel (Johnson et al., 2020; Durgan et al., 2020b; Doughty and Cavanaugh, 2019). This step involves placing the calibration target on the ground and using the sUAS camera to take an image of the target before and

after the programmed flight. These collected target images are then used in the software (i.e., Pix4D Mapper) to pre-process and calculate reflectance values from the raw digital numbers. Pinton et al. (2020) used upward facing sensors to simultaneously capture the downwelling irradiance of the sun along with the ground surface spectral reflectance captured by the camera. Another technique the authors used was to image panels of known reflectance to use along with the downwelling sensor to calibrate the DN values to percent reflectance. For example, using reference measurements from a white board and dark measurements from the lens cap to calibrate the values (Doughty and Cavanaugh, 2019). Using ground reflectance targets is the most widely adopted method and can be considered a best practice for radiometric correction in coastal wetlands using sUAS.

2.3.6. Useful Products of sUAS Imagery for Coastal Wetland Vegetation Research

The products derived from sUAS images in each study in our collection of literature were dependent upon the goals of each experiment. Digital elevation maps (e.g., DEM, DTM and Digital Surface Models or DSM) were constructed from the SfM-derived point clouds or LiDAR returns in 17 of the 20 studies. The elevation information was often used for determining structural characteristics of vegetation, though they were not always used in each study. When utilized, the elevation maps were subsequently used as inputs into models for delineating wetland boundaries/shorelines and describing the heights of various species (Farris et al., 2020; Pinton et al., 2020; Dai et al., 2020). The elevation data were also used as inputs into models for classifying species. It was demonstrated by Samiappan et al. (2016) that including a DSM can improve classification accuracy. The authors discovered that including the DSM produced one of the lowest omission errors (11.3%) when mapping invasive phragmites australis.

Incorporating the DSM, spectral information from vegetation indices, and morphological attribute profiles (MAPs) produced the best classification results (overall accuracy, or OA = 96.3%).

Another common product derived from the spectral bands of sUAS imagery were vegetation indices. Vegetation indices were subsequently used as input for species classifications, just like the elevation data. Table 2.1 describes the vegetation indices used in the 20 coastal wetland articles. Multiple indices were used as inputs into biomass models (Zhou et al., 2018; Doughty and Cavanaugh, 2019). The most commonly used index, often on its own, was the Normalized Difference Vegetation Index (NDVI). NDVI was a successful indicator of coastal wetland vegetation biomass (Doughty and Cavanaugh, 2019). In Brooks et al. (2019), the authors tested the capabilities of four indices for discriminating different SAV species. While some of the indices were originally developed for terrestrial vegetation (i.e., Modified NDVI), they were also used for submerged aquatic vegetation for detecting vegetation in the water column. The authors found that the modified NDVI was important for separating EWM from other vegetation types.

Vegetation indices based on RGB bands are widely used since many commercial sUAS come with RGB cameras. A few popular indices include the Triangular Greenness Index (TGI), Visible Atmospherically Resistant Index (VARI) and Excess Green Index (ExG), among others (Johnson et al., 2020; Dale et al., 2020). Johnson et al. (2020) found that TGI was more effective in separating the vegetation from water than VARI. Dale et al. (2020) demonstrated the utility of RGB vegetation indices for mapping differences in vegetation cover in a coastal wetland and suggest their use for cost-effective monitoring

using off-the-shelf sUAS cameras. For example, ExG slightly outperformed other indices in discriminating vegetation cover. Zhou et al. (2018) used the Difference Vegetation Index (DVI), based on NIR and red bands, to effectively model *Spartina Alterniflora* biomass.

Table 2.1. Vegetation Indices commonly used for sUAS coastal wetland modelling.

Vegetation Index	Equation	Source(s)
Normalized Difference Vegetation Index	$\frac{NIR - RED}{NIR + RED}$	Doughty et al., 2021; Zhou et al., 2018; Doughty and Cavanaugh, 2019
Visible Atmospherically Resistant Index	$\frac{GREEN - RED}{GREEN + RED - BLUE}$	Johnson et al., 2020; Dale et al., 2020; Rupasinghe et al., 2018.
Soil-Adjusted Vegetation Index[2]	$\frac{(NIR - RED)}{(NIR + RED + L)} * (1 + L)$	Zhou et al., 2018; Samiappan et al., (2016)
Simple Ratio	Ratio between any two bands. Example: $\frac{RED\ EDGE}{BLUE}$	Abeysinghe et al., 2019; Brooks et al., 2019
Blue-Green Pigment Index 2[1]	$\rho 1/\rho 25$	Cao et al., 2018
Chlorophyll Index Green	$\frac{NIR}{GREEN} - 1$	Doughty and Cavanaugh, 2019
Chlorophyll Index RedEdge	$\frac{NIR}{REDEDGE} - 1$	Doughty and Cavanaugh, 2019

Difference Vegetation Index	$NIR - (0.96916) * RED$	Zhou et al., 2018
Enhanced Vegetation Index 2	$2.5 * \frac{NIR - RED}{NIR + 2.4 * RED + 1}$	Doughty and Cavanaugh, 2019
Excess Green Index	*2 * GREEN – (RED + BLUE)*	Dale et al., 2020
Green Chromatic Coordinate or Relative Green Index	$\frac{GREEN}{RED + GREEN + BLUE}$	Dale et al., 2020
Green Normalized Difference Vegetation Index	$\frac{NIR - GREEN}{NIR + GREEN}$	Doughty and Cavanaugh, 2019
Green-Red Vegetation Index	$\frac{GREEN - RED}{GREEN + RED}$	Dale et al., 2020
Modified Chlorophyll Absorption Ratio Index 2[1]	$\frac{1.5[2.5(\rho 87 - \rho 55) - 1.3(\rho 87 - \rho 25)]}{\sqrt{(2\rho 87 + 1)^2 - \left(6\rho 87 - \sqrt[5]{\rho 55}\right) - 0.5}}$	Cao et al., 2018
Modified Normalized Difference Aquatic Vegetation Index	$\frac{REDEDGE - BLUE}{REDEDGE + BLUE}$	Brooks et al., 2019
Modified Normalized Difference Vegetation Index	$\frac{REDEDGE - RED}{REDEDGE + RED}$	Brooks et al., 2019
Modified Water-Adjusted Vegetation	$(1 + L)\frac{REDEDGE - BLUE}{REDEDGE + BLUE + L}$	Brooks et al., 2019

Index[2]		
Normalized Difference Green Index	$\frac{NIR - GREEN}{NIR + GREEN}$	Abeysinghe et al., 2019
Normalized Difference Red Edge Index	$\frac{NIR - REDEDGE}{NIR + REDEDGE}$	Abeysinghe et al., 2019
Optimized Soil Adjusted Vegetation index (OSAVI)[1]	$(1 + 0.16) * \frac{(\rho 87 - \rho 55)}{(\rho 87 + \rho 55 + 0.16)}$	Cao et al., 2018
Photo-chemical Reflectance Index[1]	$\frac{(\rho 16 - \rho 20)}{(\rho 16 + \rho 20)}$	Cao et al., 2018
Reformed Difference Vegetation Index[1]	$\frac{(\rho 87 - \rho 55)}{(\sqrt{(\rho 87 + \rho 55)})}$	Cao et al., 2018
Ratio Vegetation Index	$\frac{NIR}{RED}$	Zhou et al., 2018
Transformed Chlorophyll Absorption in Reflectance Index (TCARI)[1]	$3[(\rho 63 - \rho 55) - 0.2(\rho 63 - \rho 25) \times (\rho 63/\rho 55)]$	Cao et al., 2018
TCARI/OSAVI[1]	$\frac{TCARI}{OSAVI}$	Cao et al., 2018
Triangular Greenness Index	$GREEN - (0.39 * RED) - (0.61 * BLUE)$	Johnson et al., 2020

[1] These vegetation indices were used with hyperspectral imagery; Therefore, the

equations reference different wavelengths rather than simple green, blue, NIR channels.

[2] $L = 0.5$

Orthomosaics derived from sUAS RGB images were used in several studies for visual analysis and manual digitizing of vegetation boundaries (Taddia et al., 2021; Farris et al., 2019; Dai et al., 2020). The high spatial resolution RGB orthomosaics were also used to generate random sample points for validation and accuracy assessment (Rupasinghe and Chow-Fraser 2019). Not all studies required processing in photogrammetric software before the sUAS data was useable. In Brooks et al. (2019), the authors performed radiometric calibrations and generated vegetation indices with each individual image, and spectral signatures were also derived. The spectroradiometers provided significant spectral detail and were able to deliver detailed spectral signatures for the SAV. In a coastal wetland environment, spectral and structural characteristics are very effective in assisting image classifications for determining species spatial distributions.

2.3.7. Methods of Analysis of sUAS Imagery for Coastal Wetland Vegetation Research

A variety of methods were found to be effective for analyzing imagery in coastal wetlands. Many studies in the coastal wetland environment had the goal of mapping the spatial distribution of species and other surrounding phenomenon. In a comparison of pixel-based and object-based machine learning classifiers and the traditional maximum likelihood classifier (MLC), Abeysinghe et al. (2019) found that a Support Vector Machine (SVM) classifier outperformed all others with an overall accuracy (OA; see

section 3.8) of 90%. Johnson et al. (2020) used a SVM classifier to effectively separate mangroves from other primary vegetation classes. In another study, Durgan et al. (2020b) also used a SVM classifier to map 17 species in a coastal wetland with an overall accuracy (OA) of 68.7%. When comparing the original high resolution sUAS orthomosaic to resampled, lower spatial resolution orthomosaics, the high-resolution imagery had a higher classification accuracy as well.

Cao et al. (2018) performed a number of experiments with varying feature combinations for classifying different mangrove species with K-nearest neighbors (K-NN) and SVM classifiers. They determined that for the object-based classifiers, segmentation characteristics best represented the underlying vegetation with a spatial resolution of 0.15 m, a segmentation scale of 100, and a compactness of 0.7. However, the spatial resolution, segmentation scale and compactness will require adjustment based on research objectives. Both classifiers performed well, but the SVM classifier performed the best with an 89.55% OA. Broussard et al., (2020) used object-based image analysis to first classify the orthomosaics into vegetation and water, and then into more in-depth classes. In Rupasinghe et al. (2018), the authors tested unsupervised classifiers, an MLC and an SVM classifier on sUAS imagery and then compared the accuracies to manned-airborne hyperspectral imagery. The unsupervised classifications did not work well with sUAS data and only yielded an OA of 28.8%. The authors suggested this is because the additional spectral information from a NIR band is important for classifications, and the sUAS only collected RGB images. The SVM supervised classifier (OA = 82.4%) outperformed the MLC (OA = 79.3%), suggesting that SVM classifiers are able to perform the best. The manned aircraft hyperspectral imagery classifications (OA =

85.5%) outperformed even the most accurate sUAS classifications, suggesting that spectral information may be more important than high spatial resolution, however. Based on the reviewed literature, there is a consensus that SVM classifiers may be the most accurate for coastal wetland vegetation classification.

Models for estimating wetland vegetation biomass were developed using linear statistical models. Using sUAS data for accuracy assessment, Zhou et al. (2018) discovered that their biomass model resulted in an R^2 of 0.89 and RMSE of 0.415 kg m^{-2}. The model developed using an NDVI layer derived from a multispectral camera on an sUAS in Doughty and Cavanaugh (2019) resulted in an R^2 of 0.67 and RMSE of 0.344 kg m^{-2}.

A variety of statistical tests (i.e., ANOVA, Tukey HSD, and Tukey-Kruskal) were used in Brooks et al. (2019) to test for differences between direct field-measured (e.g., boatside, out-of-water) and data collected using a sUAS. No significant differences were found between the spectral index values when comparing direct field vs sUAS-collected data. Kolmogorov-Smirnov (K-S) tests were also performed on spectral signatures of different vegetation species. Differences were found between EWM, the vegetation of interest, and the several other species.

2.3.8. Validation and Accuracy Assessment of sUAS Imagery for Coastal Wetland Vegetation Research

Most accuracy assessments performed in the literature were conducted using validation data collected just before or after sUAS flights (Zhou et al., 2018; Doughty and Cavanaugh, 2019). Validation data were also created from manual image interpretation of

the high resolution sUAS imagery. In this case, high-spatial resolution sUAS data were used as if the researchers were there in person. As an example, Zhou et al. (2018) used the imagery to generate validation data for fractional vegetation cover in a satellite image-derived model. Similarly, Rupasinghe et al. (2018) used a stratified random sampling method to generate random points from sUAS imagery-based land cover maps for accuracy assessment. In vegetation structure-focused studies, *in situ* GNSS surveys and traditional vegetation surveys were used for accuracy assessment (Broussard et al., 2020).

Traditional validation and accuracy assessment methods were found effective for evaluating the performance of classifiers in the coastal wetland environment. For example, Abeysinghe et al. (2019) effectively used a three-fold cross validation approach to assess the many classifiers in their experiment for mapping phragmites. Other studies used *in situ* data and random sampling methods to determine a method's accuracy from a confusion matrix (Marcaccio et al., 2016; Samiappan et al., 2016; Durgan et al., 2020b). Overall accuracy (OA) was the most commonly computed accuracy assessment metric. OA was computed by using equation 2.1:

$$\boldsymbol{OA} = \frac{\sum_{i=1}^{K} x_{ii}}{N} \qquad (2.1)$$

where x_{ii} represents a pixel classified correctly, N is equal to the total number of pixels being assessed, and OA is the overall accuracy. The OA served as the baseline accuracy metric.

For a similar type of assessment, Haskins et al. (2021) used a weighted Nash-Sutcliffe Efficiency (NSE) coefficient, calculated using equation 2.2:

$$\boldsymbol{NSE} = 1 - \frac{\sum_{i=1}^{n} W_i(E_i - M_i)^2}{\sum_{i=1}^{n} W_i(M_i - \bar{M})^2} \quad (2.2)$$

where $\boldsymbol{n}$ is the number of sampled plots, $\boldsymbol{E}$ is estimated cover from classified imagery, $\boldsymbol{M}$ is measured cover from the field survey, and $\boldsymbol{W}$ is the number of intercept sampling points (weight). The NSE metric indicates agreement between the classified results and field results.

In studies estimating vegetation biomass, root mean squared error (RMSE; equation 2.3) was used to describe the differences between the modeled values and validation dataset values:

$$\boldsymbol{RMSE} = \sqrt{\frac{\sum_{i=1}^{N}(x_i - \hat{x}_i)}{N}} \quad (2.3)$$

where N = the number of data points, x_i is the ground-measured biomass, $\hat{x}_i$ is the estimated biomass (Doughty et al., 2021; Zhou et al., 2018; Doughty and Cavanaugh, 2019). Lower RMSE values indicated more accurate estimations of biomass.

2.3.9. Challenges for sUAS Imagery for Coastal Wetland Vegetation Research

A variety of challenges exist for using sUAS in coastal wetlands and are well documented in the reviewed literature. Some challenges are common across all sUAS remote sensing applications, while some are specific to the coastal wetland environment. For example, vegetated areas with standing water and changing tide levels can pose a problem when using vegetation indices to classify the vegetation (Lishawa et al., 2017).

NDVI values varied substantially between *in situ* measurements and the sUAS measurements for these areas within the study site due to the presence of water. Doughty and Cavanaugh (2019) suggested that environmental conditions, such as atmospheric conditions and tidal stage, can adversely affect biomass estimations when using sUAS data. To combat this, the authors suggest collecting imagery under consistent atmospheric conditions as close to solar noon as possible. This technique would not be effective with standing water, however. The presence of water can affect reflectance values and potentially cause an underestimation of NDVI, so imagery should be collected at a low tidal stage. Ideal research conditions should be chosen based on research objectives. More generally, sensor noise can also contribute to radiometric variability causing inconsistencies between data collections. Other shortcomings described by Rupasinghe et al. (2018) included misclassifications caused by shadows and shaded areas. While special processing techniques were used in an attempt to remove these artifacts, they still had an effect on the classification results. Finally, coastal wetland vegetation phenology can impact how vegetation indices and biomass correlate and can influence vegetation classification accuracy. Similar to methods used when classifying satellite and manned-aircraft imagery, collecting data during peak biomass for best sUAS-derived biomass estimations was recommended (Lishawa et al., 2017). When planning to compare imagery datasets across time, it is important to collect them in a similar temporal window (e.g., season) so that vegetation phenology is approximately the same.

A more general sUAS related challenge described in the literature includes the presence of artifacts in the imagery, created during orthomosaic generation, that can make classifications difficult (Samiappan et al., 2016). ‘Artifacts’ can be described as

blurred objects or discontinuities in the orthomosaicked images. For example, a boardwalk in a section of marsh may be blurred out or slightly misaligned during the mosaicking process. The misalignment or blurring of the object can cause misclassifications. In some temporal change detection analyses, the imagery available to compare the more recent sUAS imagery may have a coarser spatial resolution, which can make true comparisons can be difficult. It was also suggested that lighting conditions could result in errors in DTM accuracy (Durgan et al., 2020a).

Legal restrictions from the Federal Aviation Administration (FAA) require unmanned aerial pilots-in-command flying under Part 107 rules to be 'licensed' (i.e., the remote pilot certificate) and follow certain regulations that can potentially limit flight times and study area extent (Durgan et al., 2020b). One of these restrictions, maintaining constant visual line-of-sight, can restrict the study area to the distance of the sUAS visual recognition by the remote pilot (Broussard et al., 2020). The requirement of FAA certification to fly a sUAS for research purposes can limit the number of individuals who operate a sUAS for research purposes. Many states also put additional restrictions on the launching/landing/operating from locations of a sUAS (Hodgson and Sella-Villa, 2021). These restrictions can indirectly impact the coastal wetlands sUAS image collection plans. In a more dramatic impact, North Carolina also requires a separate state UAS permit in addition to the FAA remote pilot certificate. Remote pilots need to investigate and follow local rules and regulation wherever a sUAS is being operated.

Computing power is also a well-documented challenge. sUAS missions with a high percentage of overlap (i.e., 80%) can collect large numbers of images to be processed. Computer storage and computation power to process the images requires large

amounts of computer random access memory (RAM), large graphics processing units (GPUs) and extensive storage (Broussard et al., 2020). The millions of points generated in a point cloud can be difficult to process and handle as well. Another technological limitation comes in the form of current battery capacities and their link to flight times. Depending on the size of the drone and payload, battery power limits flight duration to less than one hour for most fixed wing and multicopter sUAS. Multiple batteries are required to fly over larger areas. Challenges discussed here are not all specific to coastal wetlands. As technology improves, our ability to collect and analyze datasets in these environments will also improve.

2.4. Directions for Future Research

2.4.1. Sensors

Both RGB and multispectral cameras have been used extensively to map and classify vegetation in three of the four general objectives observed in this review (Figure 2.3). Future coastal vegetation research should more extensively examine other sensors and instruments, such as thermal infrared sensors, sUAS-borne LiDAR, and hyperspectral sensors. LiDAR and hyperspectral sensors can be expensive investments and therefore were used in only two studies. However, data collected from these sensors and others can contribute significant knowledge on the biophysical characterization of coastal vegetation using a UAS platform. For example, thermal sensors have been used along with other multispectral sensors to detect chlorophyll content and water stress from an sUAS for crops (Berni et al., 2009). Applying similar techniques to a coastal environment may provide greater insight into variables affecting water stress in coastal vegetation. For example, Gao et al. (2014) utilized Landsat TM and ETM+ imagery,

including the thermal band, for coastal region drought monitoring. However, at such coarse spatial scales, it is difficult to discriminate coastal wetland vegetation from other types of upland vegetation. Higher spatial resolutions provided by sUAS can highlight stresses affecting coastal vegetation in specific regions, and even for specific species. There are many applications for these sensors in mapping coastal vegetation, particularly in submerged aquatic vegetation, algae blooms, and mapping structural characteristics of vegetation (Pinton et al., 2020; Brooks et al., 2019; Kislick et al., 2018). As the technology becomes less expensive and these sensors become more widely available, an increasing number of applications will provide a growing knowledge base.

2.4.2. Incorporating Multiple Scales

Many articles reviewed in this study utilized sUAS imagery as ancillary data or validation data in the study. For example, Zhou et al. (2018) performed their main biomass model with satellite imagery, and then used the sUAS data to validate the satellite-derived model. In another study, Doughty et al. (2021) compared the use of sUAS for coastal wetland biomass modelling to coarse resolution satellite-based biomass modelling and found the sUAS models to perform better. Conversely, studies like Marcaccio et al. (2016), Dale et al. (2020), and Doughty and Cavanaugh (2019), among many others, focus on the sUAS as the sole remote sensing platform.

There is merit in identifying other opportunities of data integration from all platforms and scales. sUAS can provide excellent model input and guidance for extracting information from satellite data. By including sUAS data in models of multiple scales, a high-resolution imagery gap can be filled between traditional satellite and aerial-

based imagery and corresponding *in situ* data. sUAS imagery can be used to detect the many fine scale spatial patterns and changes across a study area, and in some instances, has outperformed broader scaled products develop using Landsat imagery Doughty et al. (2021). sUAS do an excellent job improving detection of heterogeneous spatial patterns and pairing these data with coarser resolution data can enhance larger scale analysis. Although current legal restrictions and battery limitations may curb study area size and sUAS applicability, there are increasing opportunities for sUAS to be used regularly by environmental researchers and coastal managers. Battery performance is improving, and flight time capabilities have steadily increased with new iterations of fixed-wing and multicopter sUAS (Figure 2.6). Future research can take advantage of increased flight capabilities to investigate how sUAS can serve as a reliable independent remote sensing platform on its own, without the need for other manned-airborne or satellite datasets to make a meaningful contribution.

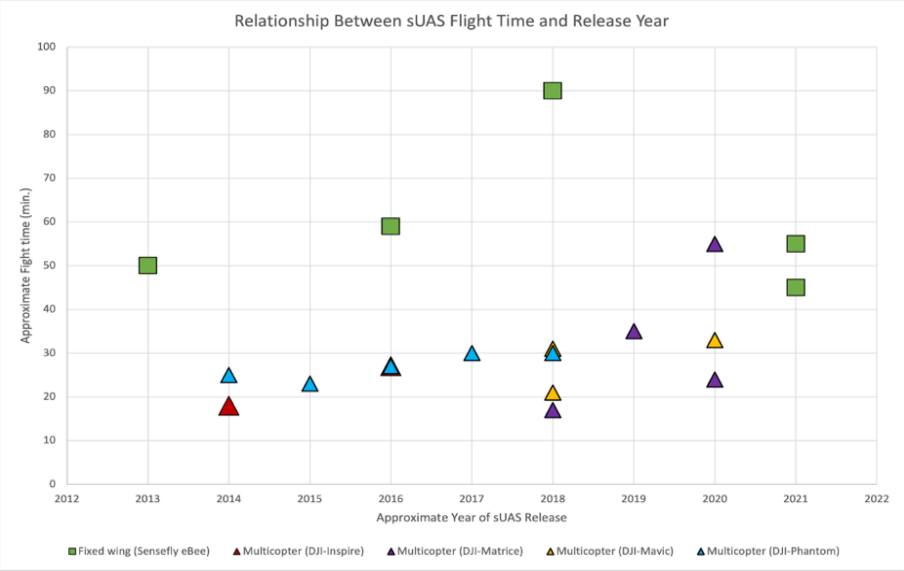

Figure 2.6. Relationship between sUAS flight time and year of model release for a sample of multicopters and fixed wing sUAS.

2.4.3. Standardization of Procedures

As previously mentioned, the coastal environment is very dynamic and can be a challenging environment for remote sensing data collection. The ever-changing weather, cloud cover, wind and tides necessitate the development of general guidelines regarding capturing imagery in these environments. Other variables that can change among sUAS missions include GCP and validation survey data accuracy and mission planning or flight parameters. While collectively coastal wetland vegetation research could benefit from a set of field-tested general guidelines, each unique study environment could benefit from a specific set of corresponding guidelines. Because sUAS data are new and developing rapidly, other scholarly research has called for a more general standardization of procedures and data sharing (Wyngaard et al., 2019; Poley and McDermid, 2020). In regard to sUAS in coastal wetland vegetation research, much progress was made by Durgan et al. (2020a) in the way of understanding the impact of flight parameters on imagery products. The effects of varying spatial resolutions were also assessed by Durgan et al. (2020b) and Haskins et al. (2021).

However, additional mission planning research needs to include exploring the appropriate number of GCPs for study area size in coastal wetland environments. Topography and vegetation characteristics differ between coastal wetland environments, and therefore may need different georeferencing requirements. While Haskins et al. (2021) determined a minimum of 2 GCPs per hectare for their study area, Santos Santana et al. (2020) found a different threshold for their study area. The GCP requirement will be dependent upon the project accuracy requirements. Further investigation is needed in a variety of coastal wetland environments to come to a consensus. Until recently, GCPs

were not frequently used or mentioned in sUAS coastal vegetation studies. A consensus for lower limits of flight parameters and mission planning (e.g., overlap or altitude and spatial resolution required to map a particular vegetation species) was not reached in our literature review. In order to correctly compare and build upon prior research, standards should be developed as soon as possible. We call on remote sensing experts and coastal wetland vegetation experts to work together on standardizing procedures for sUAS missions in vegetated coastal wetland environments.

2.5. Concluding Remarks

Coastal environments are significant for many reasons, including their economic, ecologic, recreational, and hazard reduction benefits. Coastal wetland vegetation provides a critical role in each of these benefits and warrants regular monitoring due to the extremely dynamic nature of the coastal environment. This chapter offers a review and synthesis of 20 articles pertaining to sUAS use for remote sensing of coastal wetland vegetation. Since 2016 there has been an increase in literature regarding the use of sUAS in coastal vegetation research. Limitations were related to using ground control points; balancing altitude, image overlap, and battery capacity; legal restrictions; environmental limitations; and computational requirements of the data. Overall, there is an increasing use of sUAS platforms for mapping and monitoring coastal vegetation and the challenges outweigh the limitations for a variety of applications. However, as sUAS platforms continue to be upgraded and new and improved sensors become more readily available and cost-effective, the applications and capabilities of sUAS for remote sensing of coastal vegetation will continue to grow.

The following chapter (Chapter 3) manuevers the several described limitations and builds upon the lessons learned from the extensive review to develop a new application for sUAS remote sensing in a coastal tidal marsh: using RGB sUAS imagery and derived vegetation indices to develop a model for estimating vegetation biomass. Its advancement focuses on using sUAS to enhance quantitative coastal management in a spatial aspect by studying how to reliably monitor the spatial distribution of vegetation biomass across a given marsh system.

CHAPTER 3

RGB INDICES AND CANOPY HEIGHT MODELLING FOR MAPPING TIDAL MARSH BIOMASS FROM A SMALL UNMANNED AERIAL SYSTEM[2]

[2] Morgan, G. R., Wang, C., & Morris, J. T. (2021). RGB indices and canopy height modelling for mapping tidal marsh biomass from a small unmanned aerial system. *Remote Sensing*, *13*(17), 3406. https://doi.org/10.3390/rs13173406. Reprinted with Permission from the publisher.

3.1. Introduction

Coastal tidal marshes are dynamic environments that serve a variety ecologic and economic functions in coastal regions. Beyond providing nurseries for many important aquatic species and beautiful backdrops for tourists, they also are known for carbon sequestration and water runoff filtration (Loomis and Craft, 2010; Ballard et al., 2016; Purcell et al., 2020). Despite their utility, tidal marshes face various challenges including sea-level rise and erosion. Climate change threatens the natural order of tidal marshes by strengthening various environmental stressors that are predicted to impact vegetation biomass and other biophysical characteristics, eventually leading to loss of vegetation (Thorne et al., 2018; Kirwan and Megonigal, 2013). The benefits of and future challenges for coastal tidal marshes have led many community stakeholders to recognize the importance of regular assessment and monitoring of these environments (*Sea Level Rise*, pg. 34). Successful marsh health monitoring requires the use of several metrics, including vegetation height, biomass, and density (Zhou et al., 2018; Doughty and Cavanaugh, 2019; DiGiacomo et al., 2020; Pinton et al., 2020). The complex nature of the tidal marsh environment presents challenges for frequently and efficiently gathering these metrics using *in situ* methods (Durgan et al., 2020b). Remote sensing techniques have long provided non-intrusive methods for obtaining useful biophysical measurements (Tiner, 2015).

The use of satellite imagery has been particularly successful in estimating one important biophysical measurement, marsh vegetation biomass. The use of remote sensing for estimating biomass of *Spartina alterniflora* (hereafter *S. alterniflora*), a common tidal marsh cordgrass, was introduced in 1983 (Hardisky et al., 1983a). The

study simulated bands 3, 4, and 5 of a Landsat TM imagery by collecting spectral radiance data and determining the relationships between vegetation indices and collected biomass measurements, and found that the infrared index provided the strongest relationship (R^2 = 0.92). Soon after, others investigated other spectral indices and found that many were highly correlated with coastal marsh vegetation biophysical characteristics and showed favorable predictions in comparison with traditional methods (Hardisky et al., 1983b). Further studies continued to provide substantial evidence of a strong relationship between spectral properties and salt marsh vegetation biophysical characteristics using medium resolution satellite imagery (Gross et al., 1988; Zhang et al., 1997). More recently, high spatial resolution satellite imagery (3 m) has also been successfully used to model biomass in a coastal tidal marsh (Miller et al., 2019).

Aerial imagery also performed well for estimating marsh vegetation health metrics, especially biomass. Early practitioners used 3 m Calibrated Airborne Multispectral Scanner (CAMS) data to model *S. alterniflora* above ground biomass (Jensen et al., 1998). They found the NIR band to correlate the best with biomass (R^2 = 0.879), and the four most useful vegetation indices were Infrared Summation Index (R^2 = 0.741), simple ratio (R^2 = 0.578), Normalized Difference Vegetation Index (NDVI) (R^2 = 0.576), and Soil Adjusted Vegetation Index (SAVI) (R^2 = 0.574). For further investigation, other authors used ADAR 5500 high spatial resolution imagery to measure biophysical parameters of *S. alterniflora* in South Carolina and found that SAVI was the best performing index (R^2 = 0.569) (Jensen et al., 2002). Many other studies have shown strong relationships between biomass and spectral reflectance information and are well documented by Klemas (2013).

Small unmanned aerial systems (sUAS) are a relatively new development in the remote sensing community (Jensen, 2017). With the advancement of miniaturized sensors and cameras, sUAS are able to provide very high resolution (VHR) imagery by flying at low altitudes. The relatively low-cost sUAS instruments can be flown on-demand. The coastal manager now has control over much of the data gathering processes, unlike with satellite and aerial remote sensing. Managers can use sUAS to capture imagery over small geographic areas, making them ideal for investigating subtle variations within smaller environments that are difficult to discover with coarser spatial resolution imagery captured with aerial and satellite remote sensing (Doughty et al., 2021).

sUAS have recently been used to collect on-demand VHR aerial imagery for mapping vegetation biomass. While only a small number of sUAS studies in the literature have examined the coastal marsh environment, they have increased in the past few years (Poley and McDermid, 2020). sUAS imagery has now been used successfully in conjunction with SPOT6 satellite data for estimating *S. alterniflora* biomass and fractional vegetation cover with high accuracy (Zhou et al., 2018). Others recently used an sUAS with a multispectral sensor to model coastal marsh vegetation biomass across the four seasons (Doughty and Cavanaugh, 2019). The authors found that certain seasonal models were more robust than annual models. Superior to satellite/aerial optical remote sensing, sUAS imagery can extract 3D point cloud along with orthoimages. Canopy height information may play a unique role in assisting biomass estimation of tidal marshes. A most recent study modeled salt marsh vegetation height in Beaufort, North Carolina using sUAS imagery-derived point clouds, LiDAR point clouds and *in situ*

height measurements (DiGiacomo et al., 2020). Results found that LiDAR measurements performed better than the sUAS-derived elevation values.

Most off-the-shelf sUAS can be purchased with built-in, inexpensive RGB cameras. To extend beyond visual spatial analysis, RGB-based vegetation indices, hereafter referred to as RGB indices, can be used to highlight the differences in vegetation reflectance between the red, green, and blue bands. RGB indices have recently been used to aid in mapping mangrove canopy and monitor the health of wetland vegetation (Johnson et al., 2020; Dale et al., 2020). Other studies have found success when using RGB indices to model biomass for aquatic plants, rice, winter wheat, and soybeans crops, among others (Cen et al., 2019; Yue et al., 2017; Maimaitijiang et al., 2019; Jing et al., 2017).

sUAS personal remote sensing devices offer a relatively inexpensive means to map and monitor small coastal environments, and many coastal managers are beginning to discover their utility (Tait et al., 2019; Fallati et al., 2020; Collin et al., 2019). For example, Tait et al. (2019) found that sUAS multispectral and RGB data are capable of classifying marine microalgae with considerable accuracy. In a shallow coral reef, Fallati et al. (2020) was able to identify three important substrate types from sUAS imagery for identifying changes over time. Finally, Collin et al. (2019) identified best band combinations for high classification accuracies of coastal reef environments. It is important to establish best practices for their use in a variety of practical situations (Morgan and Hodgson, 2021; Wyngaard et al., 2019). The goal of this chapter was to establish best practices for use of RGB indices and canopy height models for modeling *S. alterniflora* biomass using a low altitude sUAS. We hypothesized that RGB indices

would be highly correlated with peak *S. alterniflora* biomass measurements and canopy height information would provide useful information for creating a robust biomass model. A large set of RGB indices were explored in this study to support the use of RGB cameras installed on many off-the-shelf sUAS. The results of this chapter are meant to establish best practices of coastal managers with cost-effective means for regular monitoring of tidal marsh biomass.

3.2. Materials and Methods

3.2.1. Study Area

We conducted sUAS surveys at four marsh plots in the North Inlet Winyah Bay (NIWB) estuary at the Belle W. Baruch Institute for Marine and Coastal Sciences near Georgetown, South Carolina, USA. NIWB is a NOAA National Estuarine Research Reserve and home to *S. alterniflora*-dominated tidal salt marshes. Within NIWB, the North Inlet estuary is 7,655 Ha of relatively untouched tidal marsh wetlands. The tidal range for this area is approximately 1.4 m.

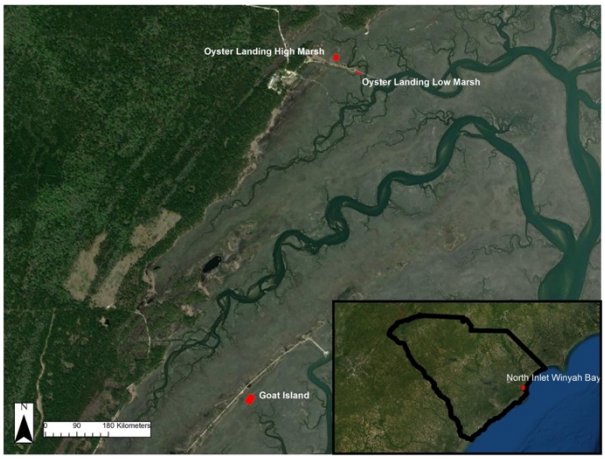

Figure 3.1. NIWB study site locations. South Carolina is located in the southeastern USA, bordering Georgia, North Carolina, and the Atlantic Ocean.

Three distinct high and low marsh study sites were selected within the North Inlet Estuary (Figure 3.1). The largest plot is located at Goat Island (GI). The other two plots are located near each other to the north at Oyster Landing. The first is in a high-marsh area (OL-HM), and the second is in a low-marsh area (OL-LM). Each of these plots have been monitored for 30+ years as part of an NSF-funded Long-Term Research in Environmental Biology project, with biomass data collected regularly (Morris and Haskin, 1990).

3.2.2. Data collection

3.2.2.1. sUAS data collection

This study utilized a DJI Matrice 100 built with modifications to include a multispectral Micasense Red Edge sensor with 5 bands: blue (475 nm), green (560 nm), red (668 nm), red edge (717 nm), and near infrared (842 nm). The calibrated multispectral sensor provided reliable spectral information to test the concepts of using RGB-indices for *S. alterniflora* biomass modeling. Regular built-in sUAS cameras have also been used in past studies in extracting RGB indices (more described in next section). The concepts tested in this study using the multispectral camera's RGB bands apply to an inexpensive, off-the-shelf sUAS RGB camera, although it is expected the radiometric accuracy is reduced in these inexpensive cameras. Flight time with one battery was approximately 15-17 minutes, and all missions combined required the use of four batteries. The sUAS came equipped with a Global Navigation Satellite System (GNSS) receiver (Figure 3.2). Each site required a variable flight path and time, though altitude was held constant at 40m with a 5 m/s flight speed. The sUAS captured 142 images at the OL-LM site, 198 images at the OL-HM site, and 287 images at the GI site. Overlap (both

side lap and front lap) was extended to 85% to ensure that orthomosaics and point clouds could be computed using the structure from motion (SfM) algorithm. Flights were conducted from 11:00 AM to 2:00 PM EST, centered around low tide (11:49AM) on August 30, 2020. The best time for remote sensing-based biomass estimation is when the species is at peak biomass (Doughty and Cavanaugh, 2019). For *S. alterniflora,* peak biomass is from late July through the beginning of October (Ai et al., 2017). Wind was variable during data collection with 4-6 m/s gusts from the northeast, and cloud cover was minimal.

Figure 3.2. The DJI Matrice 100 with the Micasense Red Edge-M multispectral camera.

Ground control points (GCPs) were collected using an Emlid Reach RS2 RTK GNSS base station and rover at all three sites (Figure 3.3). Local GNSS survey markers were used as a base station location to ensure accurate GNSS data collection. To avoid sinking into the difficult marsh, ground control points were placed along walkways

previously built for vegetation height measurement and monitoring. A few GCPs were placed in areas of high marsh, very close to shore, to expand GCP coverage around the study areas. Nine GCPs were collected throughout the GI site, six GCPs for the OL-HM site, and seven for the OL-LM site.

Figure 3.3. Emlid Reach GNSS base station (left) and rover (right) for collection of GCPs. Top middle image shows GCPs placed on the narrow boardwalk in various locations marked with red circles. Bottom middle image shows a black and white checkerboard GCP.

3.2.2.2. Biomass Data Collection

Aboveground biomass and annual production of *S. alterniflora* has been estimated at the NIWB LTREB site using monthly surveys of plant height and density since 1984 (Morris and Haskin, 1990). This on-going LTREB project is investigating salt marsh response to both natural and anthropogenic changes in the environment (Morris and Sundberg, 2021). Vegetation stem heights are measured for each plant within a sampling plot using bird ID bands to distinguish individual plants. Biomass data were calculated from stem height measurements using allometric equations based on equation 3.1 and

described in Morris and Haskin (1990), where M is the dry plant mass in grams, H is the plant height in cm, and c_n is a coefficient that depends on previously determined relationships and the month of data collection. Six of the vegetation plots are fertilized with phosphorous (15 mol P/m^2/y) and nitrogen (30 mol N/m^2/y) each year while the other 24 are control plots.

$$M = c_0 + c_1H + c_2H^2 + c_3H^3 + c_4H^4 \quad (3.1)$$

One-meter by one-meter plots each included two subplots (10 cm * 15 cm) where biomass data were gathered. A total of 29 of the 30 biomass measurements from high and low marsh subplot locations were used for model training and validation. One plot was estimated to have zero biomass during the final six months of the year and was not used for analysis. The biomass data used for this study were collected on August 13, 2020, 16 days before capturing the sUAS imagery. Though it would be ideal to collect these biomass data at the same time as the remote sensing data, there were no known disturbances to the area within the 16 days that could potentially affect the *S. alterniflora* biomass (Zhou et al., 2018). Furthermore the logistics of obtaining sUAS data at the exact time of the biomass collection were less of an issue for this study because the data values were non-destructively gathered or estimated.

Precise locational data of subplot centroid locations were captured using the Emlid Reach RS2 RTK GNSS base and rover with centimeter level accuracy (Figure 3.4). The positional data were instrumental in accurately extracting vegetation index values around the subplots. Among the 29 biomass samples eventually used, 20 were randomly selected as training data for model development and 9 for validation of the proposed model.

Figure 3.4. Example plot (bottom right) for ground biomass collection. The Emlid Reach RS2 base (not pictured) and rover were used to collect subplot centroid locations in March 2021. Centroid locations have not changed since 1984.

3.2.2.3. LiDAR Data

LiDAR data were downloaded for NIWB from NOAA digital coast website (Digital Coast Data). LiDAR data collection flights were flown over 2,300 km^2 in Georgetown County, South Carolina from December 2016 to March 2017. Five 1524 m by 1524 m tiles were downloaded to cover the study areas in NIWB. The LiDAR data were reprojected from the original geographic coordinate system into the North American Datum (NAD) 2011 UTM 17N coordinate system (m). The vertical coordinate system for the data was the North America Vertical Datum (NAVD) of 1988 in meters. Combined, the five tiles contained nearly 62.5 million LiDAR returns and required 1.8 Gb of storage space. These data were classified by the original vendor, Precision Aerial Reconnaissance (PAR), into ground returns, low noise, model key point returns, water returns, ignored ground due to breakline proximity, culverts, bridge decks, high noise, and unassigned

returns. The maximum number of returns from any one pulse from all five tiles was five, and the point spacing ranged from 38 cm to 50 cm.

3.2.3. Approaches

3.2.3.1. sUAS Imagery Processing

sUAS imagery was processed in Pix4D Mapper 4.6.4 to generate reflectance maps, point clouds, Digital Surface Models (DSM) and Digital Terrain Models (DTM) from each mission. Images of a radiometric calibration target were captured before and after each flight by the RedEdge-M multispectral camera. Calibration target images were imported in Pix4D Mapper to calibrate the raw digital numbers into reflectance values for each pixel. All data products were processed in the NAD83 (2011) UTM 17N coordinate system and the EGM 1996 geoid vertical datum at a 5 cm spatial resolution. Georeferencing error was calculated to be between 4-9 cm at each site, approximately the same error in the GNSS equipment used.

3.2.3.2. RGB Indices and Canopy Height Model

RGB indices for this study were computed from the calibrated bands of reflectance using ESRI ArcMAP 10.8.1. A number of vegetation indices previously used for biomass modeling in past studies were tested, as indicated in Table 3.1. Calculations for each index were performed using the *raster calculator* tool. We used the *zonal statistics as table* tool in ArcMap 10.8.1 and 30 cm by 30 cm square buffers to extract the mean vegetation index value around each subplot location. The square buffers were specifically calculated around the points of interest collected using the Emlid reach RS2 GNSS. All values within the buffer were averaged together to generate our vegetation index value for that particular location.

Table 3.1. Vegetation Indices computed for sUAS biomass modeling.

Index	Formula	Reference[1]
ExG	$2 \times G - R - B$	Jing et al., 2017
GCC or Green Ratio	$G / B + G + R$	Yue et al., 2017
GRVI	$(G - R) / (G + R)$	Jing et al., 2017
IKAW	$(R - B) / (R + B)$	Maimaitijiang et al., 2019
MGRVI	$(G^2 - R^2)/ (G^2 + R^2)$	Cen et al., 2019
MVARI	$(G - B)/(G + R - B)$	Cen et al., 2019
RGBVI	$(G^2 - B*R)/(G^2+B*R)$	Possoch et al., 2016
TGI	$G - (0.39 * R) - (0.61 * B)$	Michez et al., 2018
VARI	$(G - R) / (G + R - B)$	Cen et al., 2019
VDVI or GLA	$(2 * G - R - B) / (2 * G + R + B)$	Cen et al., 2019

[1] These indices have been used in in many other contexts and articles in the literature of biomass mapping. The authors recommend examining Poley and McDermid (2020) for a more extensive review.

In addition to vegetation indices, DTMs and DSMs were produced using a structure from motion (SfM) algorithm in Pix4D that generates a point cloud (Westoby et al., 2012). Pix4D Mapper software uses the points classified as the top of whatever

surface (i.e., vegetation or ground) to generate the DSM. The DTM was constructed from the points classified into the ground category. Since the ground is difficult to see through the dense *S. alterniflora* canopy, ground points were sparse. This resulted in the use of extensive interpolation, and a less perfect bare Earth surface. A recent study found that a LiDAR derived DTM provided a more accurate representation of the bare earth for modeling *S. alterniflora* height (DiGiacomo et al., 2020). LiDAR data collected in 2017 for Georgetown County, South Carolina were used to create a more reliable DTM. These LiDAR data were filtered to only include ground returns. Ground returns were then used to generate a DTM. Before the creation of the DTM and DSM, both the sUAS point cloud and LiDAR data were reprojected into the same NAD (1983) HARN South Carolina State Plane coordinate system.

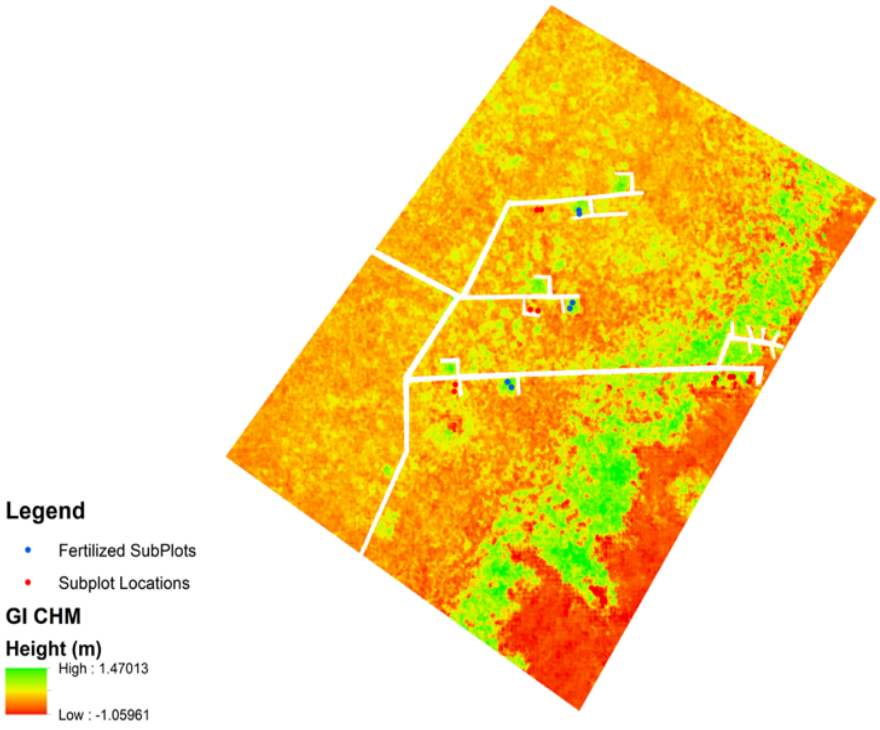

Figure 3.5. Example CHM for the GI site. Fertilized plots are represented by blue dots and other, non-fertilized plots are represented by red plots.

The DSM and LiDAR-derived DTM were used to create a canopy height model (CHM) of each of the study areas (Figure 3.5). In using a DTM derived from 2017, the authors assumed little to no change in the surface topography. The 2020 sUAS data were assumed to represent the current height of vegetation. As shown in figure 5, there is apparent variability throughout the CHM that can be visible associated with where fertilized plots are found.

A CHM was derived by Equation 3.1, where CHM is the canopy height model, DSM is the digital surface model produced by the Pix4D software, and the DTM is the ground surface generated from LiDAR returns (unit in meter):

$$CHM = DSM - DTM \quad (3.2)$$

The CHM was generated to assess its utility for adding merit to biomass modeling with RGB indices.

3.2.3.3. Biomass Modeling and Mapping

RGB indices and biomass models were explored in R studio 4.0.2. First, a correlation matrix was created to determine which indices could potentially contribute unique information to a biomass model. Investigation of single index scatter plots with the biomass data revealed a nonlinear relationship between biomass and the RGB vegetation indices. Therefore, each RGB vegetation index was explored as a variable in a polynomial regression with the reference biomass values. The best performing model, initially determined by coefficient of determination (R^2) and statistical significance, was applied to each study area (GI, OL-LM, and OL-HM).

Biomass maps were extracted after applying the best-fit model equation to each study site. At the 9 validation subplots, we used the *zonal statistics as table* tool in

ArcMap 10.8.1 and 30 cm by 30 cm square to extract the average modeled biomass values. The extracted values were then compared to the ground biomass values at these validation samples with the root mean squared error (RMSE) metric:

$$\boldsymbol{RMSE} = \sqrt{\frac{\sum_{i=1}^{N}(x_i - \hat{x}_i)}{N}} \qquad (3.3)$$

where $\boldsymbol{N}$ = the number of data points (N=9), $\boldsymbol{x_i}$ = the ground-measured biomass, $\boldsymbol{\hat{x}_i}$ = the estimated biomass. A smaller RMSE value represents better agreement between the modeled and ground surveyed biomass. RMSE was calculated from the validation dataset only.

3.3. Results

3.3.1. Biomass characteristics of tidal marsh

Using such a temporally extensive LTREB biomass dataset presented the opportunity to investigate the *S. alterniflora* biomass characteristics and its temporal and spatial patterns. Figure 3.6 shows the measured biomass at 29 subplots in NIWB throughout the year 2020. These data were used for model calibration and validation. The peak biomass dates can be considered for most plots between June-October. This agrees with one author's a-priori knowledge from 20+ years of living near and with the common smooth cordgrass and assessments (Morris and Haskin, 1990).

All sites were categorized as high marsh or low marsh. High marsh environments showed greater average biomass measures (0.966 kg/m^2) than the low marsh areas (0.653 kg/m^2) for August 2020. These averages included fertilized plots in the high marsh, however. Removing the fertilized plots from the calculations results in two more similar

averages (High marsh: 0.620 g/m^2; Low marsh: 0.653 kg/m^2) that are more consistent with the literature (Morris and Haskin, 1990).

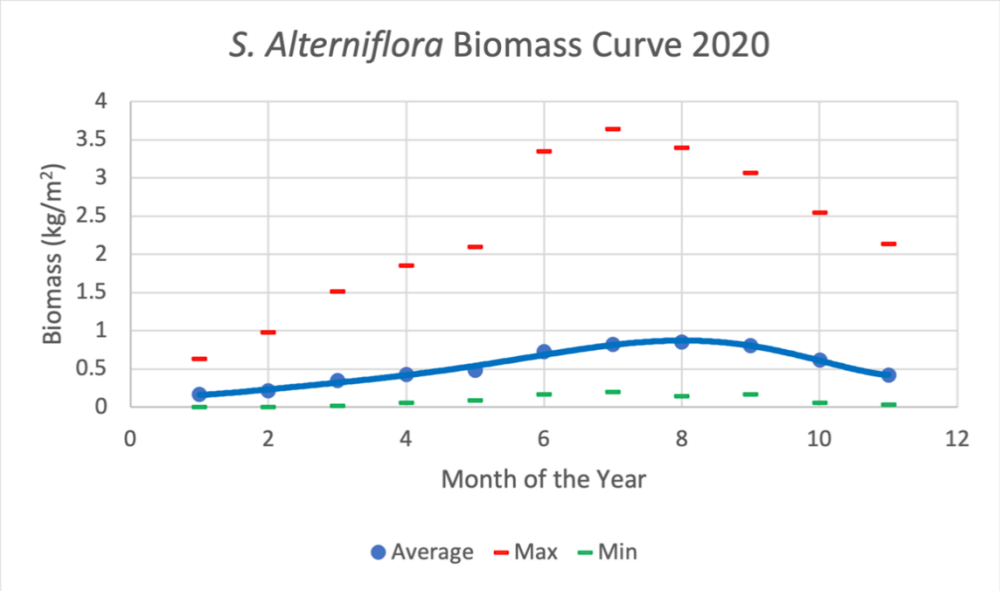

Figure 3.6. *S. alterniflora* average biomass curves derived from 29 subplots in NIWB over the year 2020. The peak biomass for each plot varies but ranges from late July to the beginning of October.

3.3.2. Vegetation indices and Biomass Models

After a thorough review, we discovered nine of the ten RGB-vegetation indices were highly correlated (Figure 3.7). The IKAW index was the only index without as high a correlation with other indices and height, but also was not very strongly correlated with biomass. The height variable was also not as correlated with other variables. Following those two, ExG and TGI were both highly correlated with each other, but not as correlated with other indices. The other seven indices we investigated were all highly correlated. This made it clear that we would not be able to conduct a multivariate regression as highly correlated variables would overlap a good bit in their effect on the regression quality, and in particular the regression results.

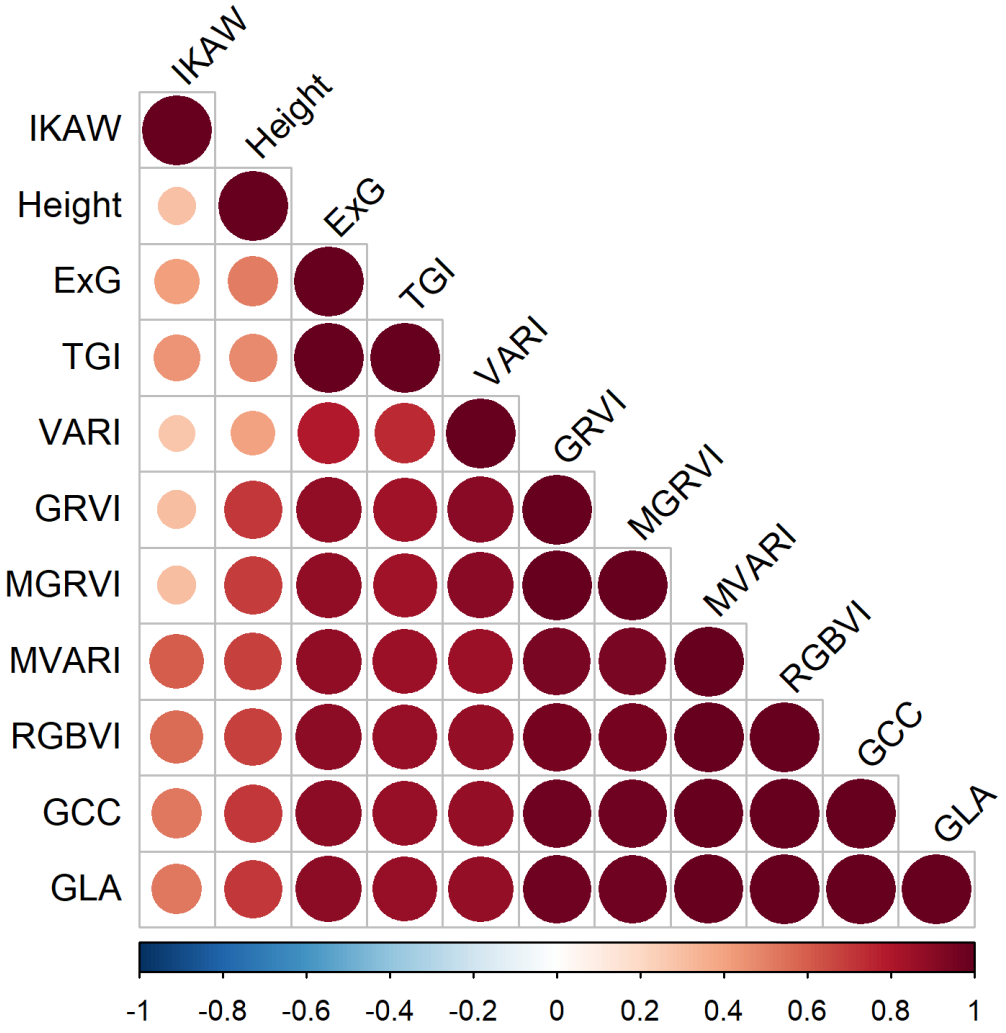

Figure 3.7. Visualization of the correlation matrix for all 10 RGB vegetation indices and canopy height.

In order to create the most parsimonious model, linear and nonlinear quadratic biomass estimation models were created using each individual RGB index rather than combining correlated variables into a flawed multivariate model. The quadratic models performed better than the linear models in all cases other than the model based on the GCC index. The scatterplots of the models, along with R^2, are shown in figure 3.8.

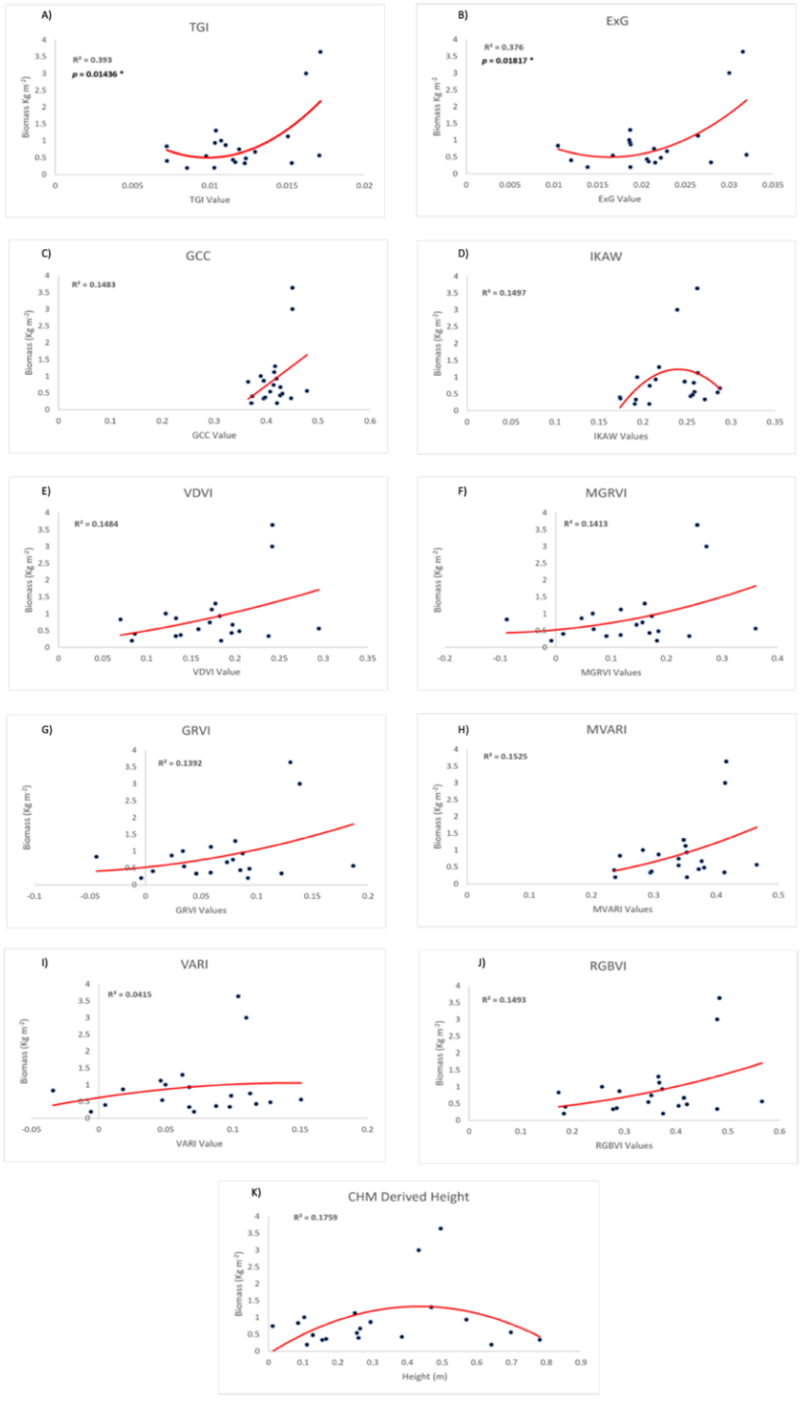

Figure 3.8. Scatterplots and Trendlines for each RGB index and Height metric with the training biomass data. R^2 represents the coefficient of determination, and p values are indicated if the model was significant.

The best performing model, based on RMSE in conjunction with R^2, was the ExG index quadratic model (R^2 = 0.376; significant at $p < 0.05$; RMSE = 0.57 kg m^{-2}; See equation 3). The TGI quadratic model (R^2 = 0.39; significant at $p < 0.05$; RMSE = 0.67 kg m^{-2} performed similarly well with slightly more explanatory power. As shown from the formulas in Table 3.2, TGI and ExG are both distance-based indices or based on simply subtracting or adding visible light bands together. In plots A and B within Figure 8, both indices spread out the data points enough to allow the creation of a more reliable model. ExG represents a linear band combination (ExG = 2 × G − R – B) while the TGI is basically the same but is further tested to empirically fit in crop studies (TGI = G − (0.39 * R) − (0.61 * B)) (Michez et al., 2018). Here we decide to maintain the simplicity by choosing ExG for estimating biomass in coastal marshes. The biomass model is extracted as:

$$Biomass = 6943.5 * ExG^2 - 226.82 * ExG + 2.3477 \qquad (3.4)$$

All other RGB indices performed poorly, none of which was significant at p = 0.05 and the highest R^2 was 0.1525. Upon the formulas in Table 2, these other RGB-indices were based on ratio between the visible light bands. Using a ratio of the bands created a cluster of data points that resulted in a less-than-significant model and low R^2 (Figure 3.8).

With a relatively small sample set, outliers in the biomass model need to be carefully examined. Figure 3.8 shows that all plots include two points with extreme values that contribute to the nonlinear relationships. These two points with high index and biomass values come from two of the fertilized sample plots. In regard to biomass measurements and their relationship with RGB index values, the fertilized plots add value

to our model. They represent high biomass areas that can be seen across the wider NIWB area, and are important to include in RGB-index data analysis. In our future study, more high-biomass points will be collected to strengthen our model development.

Against our hypothesis, vegetation height was not an effective biomass indicator (Figure 3.8, bottom graph). The relationship was nonlinear ($R^2 = 0.175$) and not significant at p = 0.05. The fusing of LiDAR data with sUAS SfM point clouds to create a CHM presented the authors with various challenges. Similarly, the two outliers in the middle of the graph in Figure 8 come from fertilized plots, which have extremely high biomass but the canopy heights are only around 0.4-0.5 m. We attribute the flat trend to the relatively homogenous growth height in the reserved marsh. Although the absolute elevations of the plots vary across geographic space, the canopy heights are relatively homogenous regardless of location.

3.3.3. Biomass Maps

Biomass maps were created using the ExG-based biomass model (Eq. 3.3) at each study site in NIWB (Figure 3.9). A standard deviation histogram stretch was applied to the maps to accentuate the visual variability of biomass distributions in the maps. The real values of biomass were not changed. Only marsh pixels were mapped. Open water and manmade structures such as boardwalks were masked out. A minimum threshold of either 2 standard deviations below the mean or 0 was used as the lower threshold of index values for input into the model. Although the areas should be low in biomass, negative index values would actually contribute to high biomass values on the map if not controlled. The histogram of index values varied depending upon the study site, but there were consistently exceptionally high ranges yet small means and standard deviations.

Upper limits of index values derived from 2 standard deviations were used to control for extreme outliers presumably caused by atmospheric conditions and small pixel sizes that captured high variability.

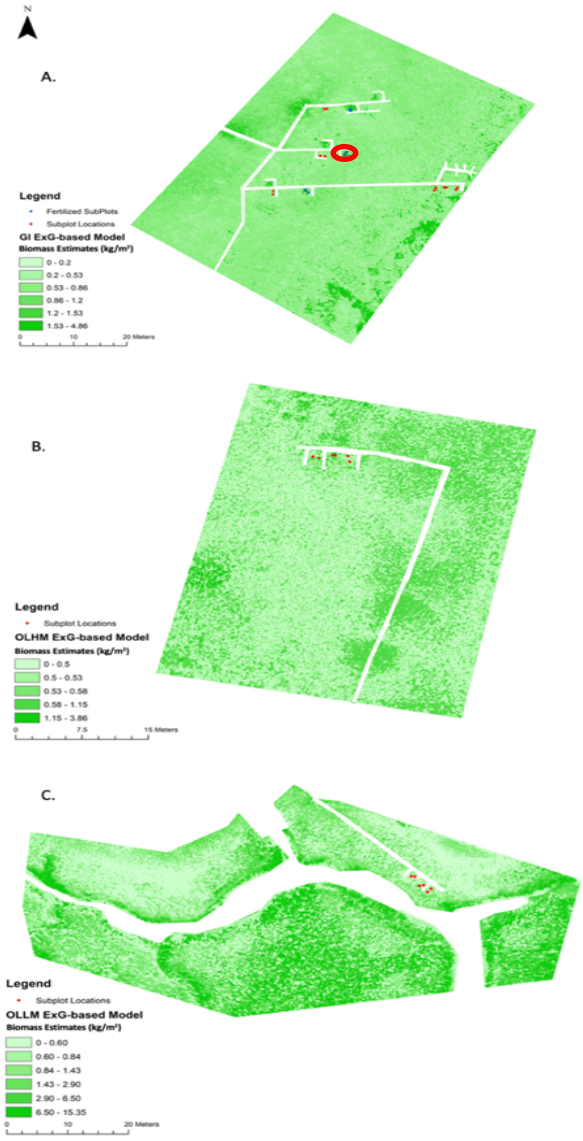

Figure 3.9. Biomass maps and sample point locations for GI (a), OLHM (b), and OLLM (c) using the ExG-based model. The two samples with the highest biomass (as shown in Figure 3. 8) are circled in red in (a).

At the GI site (Figure 3.9A), the estimated biomass ranged from 0-4.86 kg/m^2. As a high marsh close to shore in the west (where the boardwalk is connected to), biomass is relatively low across the site. The fertilized long-term LTREB plots show distinctively higher biomass than other areas in the high marsh. The biomass maps represent the fertilized plots very well; all three fertilized plots used in biomass data gathering are dark green on the GI map. The two subplots with extreme values in model development (as shown in Figure 3.8) are marked in Figure 3.9. Being fertilized and growing well, these two subplots reached the biomass values of 3.63 kg/m^2 and 2.99 kg/m^2, respectively.

The six fertilized subplots (two per fertilized plot, the blue point marks in Figure 3.9A show interesting trends. All six fertilized plots are in high marsh at the GI site. Compared to all 20 of the biomass values used for model training across the three sites, two subplots show significantly higher biomass measurements, two show slightly higher estimates, and two show relatively low measurements throughout the year. For example, in August 2020, the highest two subplots were over 2.0 kg/m^2 greater than the site average. The two slightly higher-than-normal measurements still were about 0.30-0.40 kg/m^2 more than the site average. The last two fertilized subplots were 0.30 to 0.40 kg/m^2 less than the average biomass measurements. Nevertheless, each of these subplots are on the high end of biomass for the GI environment, thus showing a dark green footprint compared to the other plots. Other plots that are not fertilized do not show up as well along the boardwalk section. Three other fertilized plots that are not used for this data gathering research project are also visibly apparent.

The OLHM site (Figure 3.9B) is a typical high marsh close to shore in the south. Marshes are naturally grown without fertilizing experiments. Its biomass is generally low

in a range of 0-3.86 kg/m^2. The marsh in the west of the boardwalk has homogeneously low biomass. Reasonably, areas further away from shore has increasing biomass.

The OLLM site (Figure 3.9C) is named as a low marsh because its topography is lower than other two sites and it is further into the NIWB Estuary. The geomorphology of the site, the creek bank, a nearby causeway and pier make the OLLM site unique. It is an area prone to wrack disturbances as well, compounded by the pier's support pilings. Due to the accessibility, all biomass samples were collected in the north along the boardwalk, which may attribute to model misfitting in the typical low marsh. As shown in the figure, the maximal biomass reaches 15.35 kg/m^2, which is unrealistically high and needs further investigation in the inner estuary.

Spatial patterns described in literature (Miller et al., 2020; Morris et al., 2005), such as higher biomass along the tidal channels and in the low marsh of inner estuary, are apparent in our maps. However, despite the recognizable patterns, the models significantly overestimate biomass as true biomass gets higher. When conducting model validation using the 9 biomass samples, estimates of lower biomass from 0.3 to 0.9 kg/m^2 had less absolute error (i.e., + 0.006 to -0.42 kg/m^2 absolute error) than the higher estimates (i.e., 1.95 kg/m^2 error). For example, a fertilized subplot resulted in 1.94 kg/m^2 error between the observed value of 1.28 kg/m^2 and the estimated value of 3.23 kg/m^2. In contrast, an unfertilized plot resulted in a mere .0055 kg/m^2 error between the observed value of 0.575 kg/m^2 and the estimated value of 0.5695 kg/m^2. In our future work, larger training and validation datasets will be collected for rectifying overestimation and recalibrating the model. This may entail more measurements and then estimated biomass, but we would also like to explore destructive measurements of biomass as well.

3.4. Discussion

RGB cameras are inexpensive and can be found on most off-the-shelf sUAS. The near ubiquity of the visible-light cameras provides coastal managers with effective tools to map coastal wetlands. One of the benefits of sUAS-based remote sensing is that several types of environmental metrics can estimated or obtained from a single sUAS flight, providing the means for a comprehensive environmental evaluation that can include metrics related to vegetation, sediment type, morphology, and much more for hard-to-reach areas (Dale et al., 2021; Fairley et al., 2018; Adade et al., 2021). This study achieved similar results as those employing vegetation indices beyond visible spectra, for example, the normalized difference vegetation index (NDVI; $R^2 = 0.34$) in a California coastal wetland (Doughty and Cavanagh, 2019). This study enhances our understanding of RGB indices and their relationships with *S. alterniflora* biomass. While this study used a calibrated sensor with higher spectral sensitivity than the typical consumer grade sUAS visible light camera, by focusing on the red, green, and blue bands we were able to test the concept of using RGB imagery for biomass modeling. Future work will compare these results with an inexpensive, more readily available sUAS and built-in cameras. Multispectral imagery, particularly the NIR band, is considered optimal for vegetation related studies, and future work will look at comparisons here as well. Given the flexibility of consumer-oriented sUAS flights, the RGB index could serve as a quick tool for coastal managers to investigate marsh healthiness in small areas at high spatial and temporal resolutions.

This study unveils that the distance-based RGB indices perform better than the common ratio-based indices for biomass estimation of coastal marshes from sUAS

imagery. Comparison analyses revealed that the excess green index (ExG) was the most suitable RGB index in this study, with a moderate nonlinear relationship ($R^2 \approx 0.4$) and the biomass measured in the late summer during peak biomass. The ExG was originally created to map fractional vegetation cover, but it has also shown good results for other applications in numerous other studies (Woebbecke et al., 1996). It has also been shown to be sensitive to chlorophyll and nitrogen content, just like TGI (Dale et al., 2020). The TGI was developed by Hunt et al. (2013) and has shown many strengths in various applications thus far. In a wetland environment, Johnson et al. (2020) mapped mangroves and successfully used TGI for separating vegetation classes from water and for estimating canopy cover. Though it partially overestimated canopy cover, it showed a better sensitivity to vegetation than the visible atmospherically resistant index (VARI). Another found that TGI performed remarkably well for estimating hops canopy cover, just like the ExG (Stary et al., 2020). Both indices perform well in many applications and are highly correlated because they are sensitive to the same vegetation elements. Of the two distance-based equations, we suggest ExG is the most useful for coastal managers for mapping biomass in tidal salt marshes because of the universal applicability of the equation. The equation used to create the ExG index simply relies on doubling the impact of the green band and then subtracting the red and blue bands. This can be applied to all environments without modification. TGI was originally found to be a strong indicator of chlorophyll content but also particularly sensitive to nitrogen fertilizing, which was performed on the fertilized plots. However, the TGI requires the use of empirically derived variables in the equation that may need adjustment for some environments. Furthermore, TGI was originally developed with hyperspectral imagery monitoring

crops. ExG was originally developed for weed identification. It is of note that while TGI and ExG performed best during peak biomass, different indices may perform better at different times throughout the year. Future research will explore the use of RGB-indices for biomass modelling during other seasons and *S. alterniflora* phenological states.

Stem height of salt marshes is highly correlated with vegetation dry weight (Davis et al., 2015). The LTREB project at NIWB uses its own equation to estimate biomass from its monthly surveys of stem height (Morris and Haskin, 1990; Morris and Sundberg, 2021). However, the experiment in this study found that drone-extracted canopy height data (CHM) were not effective in modeling biomass. It is important to note that the CHM we used for our study was not related to the height data used to calculate the biomass using equation 3.1. We expected the relationship to be very strong because height is the variable used for calculating biomass. While the R^2 of the height quadratic regression model was within the range presented by DiGiacomo et al. (2020), the statistical relationship between CHM and the measured biomass was not significant. The CHM extraction in this study utilized the LiDAR data ground returns as bare earth surface, which was found working well on terrestrial woodlands (Wang et al., 2021). In Coastal wetlands, however, studies have reported on the poor performance of LiDAR elevation, which may introduce high uncertainties to CHM (Enwright et al., 2017; Rogers et al., 2016; Hopkinson et al., 2004). Future work will be conducted with intensive field GNSS collection for better assessment of digital terrain model and digital surface models at our study site. Low marshes and high marshes can also be investigated separately to determine if elevation influences biomass modeling capabilities with sUAS.

It is important to address the modelling uncertainties. First, the ground biomass collection for training remote sensing-based biomass models has long been a destructive process. However, the biomass model training and validation data used for this study were non-destructively modeled from stem height measurements. Though the modelling equation used for biomass measurements has been shown to be very accurate, it is still modeled and therefore introduces another layer of uncertainty into the remote sensing model. These methods were proposed to attempt non-destructive means of sUAS remote sensing for biomass modeling. A comparison between destructive and non-destructive methods should be investigated to identify where and how much variability is added into the remote sensing modeling technique. Future work should also focus on incorporating larger training and validation samples to create a more robust model.

Wetlands can be difficult to map using remote sensing because of their complex nature. Environmental conditions can cause variability in reflectance. High tide was avoided to limit the amount of moisture in each image, but even at low tide residual moisture can be visible in patches within the vegetation canopy. Furthermore, there are many tidal creeks present within NIWB that can be seen on some of the imagery. These tidal creeks are unavoidable and add to the complexity of mapping in wetlands. Cloud cover and wind were variable between missions. Although reflectance targets were imaged before and after flights, conditions during flights also changed slightly. A sensor placed on the sUAS facing the sun can be used to capture solar irradiance during the flight. One study gathered with such a sensor but did not use the data as they felt it caused an overestimation of NDVI values (Kirwan and Megonigal, 2013). We suggest

investigating the impact of including a more comprehensive radiometric correction to improve sUAS-based biomass modeling of *S. alterniflora.*

A previous study has presented several flight configurations (i.e., flight altitude and overlap) and lighting conditions from sUAS flights and their effects on various products in a coastal wetland (Durgan et al., 2020a). This chapter investigated the optimal RGB indices for practical use in estimating biomass measurements in a tidal marsh system. sUAS are being presented to coastal managers and professionals as a time-saving instrument for coastal wetland vegetation research (Durgan et al., 2020b; Marcaccio et al., 2020). These experiments so far have added support to these sentiments and others presented in chapter 2, though future research is required to continue the development of practical applications of sUAS for use in coastal environments.

3.5. Concluding remarks

As we continue into decades of sea level rise and climate change that are predicted to significantly affect coastal tidal marshes, the development of efficient and effective monitoring practices is sorely needed. sUAS present coastal managers and researchers with cost-effective and on-demand tools for gathering data pertaining to several coastal tidal marsh vegetation health metrics. In this chapter we demonstrated the utility of sUAS-extracted RGB visible light vegetation indices for modeling *S. alterniflora* biomass in order to monitor its spatial distribution. The optimal index is the ExG index (RMSE = 0.598 kg/m^2; R^2 = 0 .376). The extracted biomass maps fairly reflect the spatial variations of biomass at three marsh sites. Height metrics from the sUAS point cloud, relying on LiDAR-derived bare earth model, did not significantly enhance our biomass models.

For the previous two chapters, chapter 2 established commonly used practices and suggestions for the practical application of sUAS remote sensing for monitoring tidal marsh, and chapter 3 applied these practices to focus on the use of sUAS remote sensing for biomass modeling in coastal tidal marsh. However, monitoring tidal marsh systems also benefit from a temporal component; rather than a single snapshot of the system, managers require regularly updated information to identify what is changing and why it might be changing. The next chapter, chapter 4, buildings upon chapter 3 by incorporating the temporal component of coastal management and explores the continued use of sUAS to monitor a marsh system long-term. Wrack, a common nuisance to beaches and marshes, is monitored over a one-year period to identify the wrack's spatial distribution and impact before and after the influences of a storm event.

CHAPTER 4

MAPPING WRACK MOVEMENT AND IMPACT ON COASTAL MARSHES WITH MONTHLY SUAS IMAGE SERIES[3]

[3] Morgan, G. R., Morgan, D. R., Wang, C., Hodgson, M. E., Schill, S. R. (2022). Mapping Wrack Movement and Impact on Coastal Marshes with Monthly sUAS Image Series**.** To be submitted to *Estuaries and Coasts.*

4.1. Introduction

Tidal wrack, or dead plant material that form mats, can be found in a variety of coastal settings. Throughout the year large amounts of deposited wrack can be found piled up in tidal marshes. It has long been held that tidal wrack can settle on living vegetation and have negative effects, even to the point of killing the underlying vegetation. Reidenbaugh and Banta (1980) sought to prove this by examining aerial photographs from seven missions over two years to observe the movements and impact of tidal wrack in Virginia. They found that the wrack can incrementally move its way up to the high marsh, and that wrack can kill underlying vegetation under certain conditions. They also discovered that devegetated areas could remain as such for up to two years. Valiela and Rietsma (1995) studied the disturbance of vegetation by 195 wrack mats that were stranded over a marsh. They determined that the larger mats that remained static for as long as 3-4 months and stranded at higher elevations did the most damage to the underlying vegetation. Brewer et al. (1998) investigated experimental wrack burial and found evidence to support the prior assertions that wrack disturbances interact strongly with marsh elevation. More recently, an experiment examining the impacts of wrack thickness was conducted whereby 2-3 cm thick and 15-20 cm thick wrack mats were placed on top of vegetation in experiment plots in a coastal salt marsh (Stalter et al., 2006). The study found that over a seven-month periods the larger wrack mats affected the underlying vegetation more negatively than the smaller mats.

In a study investigating sea level rise inundation and wrack deposition on vegetation both independently and together, Tolley and Christian (1999) established that one result of wrack deposition was the redistribution of species in a high marsh. Fischer

et al., (2000) investigated the spatial pattern of disturbed patches of vegetation (caused by wrack deposition) along a tidal creek in coastal Georgia and modeled the relationship between the disturbed patches and morphology of the creek. They found that areas where water slows down or where flow is multidirectional are the most vulnerable. Areas disturbed by wrack not only allow other high marsh species into the *Spartina Alterniflora* dominated low marsh, but these disturbed areas can also allow invasive species, like *Phragmites Australis,* to find a foothold in an ecosystem (Minchinton, 2002). Wrack deposition can also bring with it other forms of marsh intrusion by way of other small debris and pollution (Viehman et al., 2011).

Some studies documented that wrack can also have a positive association with marsh vegetation health and biomass (Pennings and Richards, 1998). The positive effect of wrack on marsh can depend on the thickness of the wrack mat and the length of time it takes for the detritus to decompose. The decomposition of wrack actually leads to a strengthening of the marsh system over time, though these positive effects take a long time to become evident (Montemayor et al., 2011). The strengthening of the marsh comes from the releasing and absorption of nutrients that promote and strengthen the food web in the marsh ecosystem (Negrin et al., 2012). Most recently, Van Stan et al. (2020) investigated the long-term effects of the potential of wrack to store freshwater from rain that can benefit specific plant communities. The ability for dense wrack to store water could also potentially influence its weight and therefore increase or speed up the impact it has on the underlying vegetation. While the positive effects of wrack on marsh systems have been documented, the negative effects wrack mats can have on marsh ecosystems occur more rapidly and are more easily discernible, as shown in the literature above.

Whether wrack deposition provides more benefits than detriments is still debated by coastal scientists and managers. Biases may come from the limitation of small-size plots in field experiments. Furthermore, wrack deposition, persistence, and subsequent effect on vegetation following the influence of a hurricane has yet to be comprehensively examined (Doyle, 2016). Little is known about the temporal-geographic distribution of wrack as it is often in hidden areas within the marsh. Wrack is known to be brought in and deposited by hurricane storm surge, but its long-term influence of the storm has not been studied, creating a gap in literature (Platt et al., 2015).

Small unmanned aircraft systems may bring new insights to wrack studies from high spatial resolutions and frequent temporal intervals. While small, unmanned aircraft have a rather robust military pedigree, their use by civilians began more recently (Hardin and Jensen 2011; Hugenholtz et al., 2012). In 1979, Przybilla and Wester-Ebbinghaus performed the first documented experiments with unmanned aerial vehicles (UAVs) in photogrammetric applications (Colomina and Molina, 2014). UAVs and small unmanned aerial systems (sUAS) were soon considered for disaster response, vegetation monitoring, glaciology, animal monitoring, conservation, and rangeland monitoring, amongst others (Terwilliger et al., 2015; Bhardwaj et al., 2016; Hugenholtz et al., 2013; Klemas 2015; Koh and Wich 2012). In the midst of the sUAS remote sensing revolution, coastal wetland scientists and managers have turned to the new technology to fill a data gap. Klemas (2015) delivers an extensive overview of the types, capabilities, and benefits of sUAS in a wetland environment. Highly accurate GNSS positioning technology allows sUAS to systematically fly over wetlands that were previously difficult to access due to the roughness of the environment. The advancement of sUAS technologies provides

excellent grounds by which the new high spatial and adjustable temporal resolution imagery can benefit coastal wetland monitoring. Not only can they capture extremely high-resolution imagery, but they can be deployed on-demand and at the most opportune times. The adjustable temporal resolution plays a key role in understanding both the effects of the movement and deposition of wrack that frequently, and sometimes perpetually, covers coastal wetlands.

With the new opportunities inherent in the development of sUAS technology, there is now the possibility of mapping the location and movement of wrack, as well as the health of the surrounding (and possibly uncovered) vegetation at higher spatial and temporal scales. These new data can offer new insight into the following questions:

- How long does wrack need to stay in the same location to have an effect on the underlying vegetation?
- How long can wrack deposited on vegetation from a hurricane remain there, and what kind of consequences follow?
- Are other pollutants now heavily involved with wrack as well, particularly after an extreme event, and what impact does their movement have?"

This chapter begins to address these questions by testing the feasibility of mapping wrack using monthly sUAS flights within two hours of low tide over a tidal marsh system throughout a calendar year. We propose the use of a small unmanned aerial system for mapping and monitoring wrack for effectively enhancing our understanding of wrack spatial distributions, patterns, movements, and effects following a hurricane event. Never before has wrack been mapped at such a fine temporal scale from an aerial perspective. Additionally, flights for this study were conducted before, immediately after,

and approximately monthly following the influence of hurricane Isais over the study area to identify how long wrack movement caused by a storm event can impact a marsh. Visual observation techniques from Jensen (2018) were used to identify wrack movement patterns and potential impacts from the wrack in the multidate orthomosaics. Using this chapter as a guide, coastal managers and scientists should be able to design and execute a plan for monitoring wrack phenomenon and impact on a coastal wetland in their stewardship.

4.2. Materials and Methods

4.2.1 Study Area

The study area of interest is a small coastal tidal marsh adjacent to Harbor Island in Beaufort County, SC within the Ashepoo, Combahee, and Edisto (ACE) Basin. The ACE Basin is home to numerous plant and animal species, as well as an almost 5,000 hectare National Wildlife refuge (*About the Refuge*, 2019). Parts of eastern Beaufort County are included in this basin, including Harbor Island. Our specific area of interest (Figure 4.1) is a 40 ha subset of a coastal tidal marsh situated between the Harbor River to the west and the island rental homes on the narrow strip of island to the east and north. The tidal marsh vegetation is predominately *Spartina Alterniflora*, though small patches of *Salicornia virginica* are also present near the river and tidal creeks. Wrack is frequently found along the beaches on Harbor Island, as well as in the estuaries and tidal marshes.

In August 2020, Hurricane Isaias affected portions of Harbor Island with tropical storm force winds, flooding and high tides. Isais was a category 1 hurricane at the time it

passed within approximately 100 km of our Harbor Island study site, later to make landfall near the South Carolina-North Carolina state borders. The close proximity of the storm resulted in extensive wrack deposition and movement across the study area. While damage caused by hurricane Isaias was prevalent in many other locations across North Carolina and Virginia, Harbor Island was thankfully spared from the devastation other areas experienced.

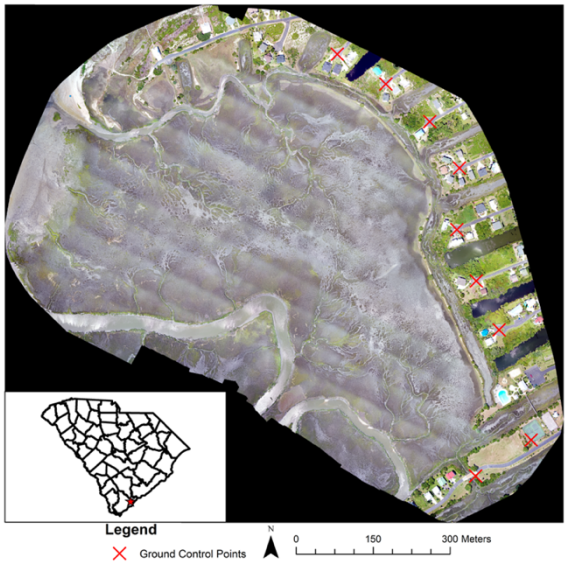

Figure 4.1. Study area for each recurring flight with GCPs. The example orthomosaic was collected from the flight on August 1, 2020.

4.2.2 sUAS Data Collection

The collection of sUAS image data began on August 1, 2020 and continued monthly until June 21, 2021. Flight dates, including flight times, weather, and the time of low tide for each fight are included in table 4.1. Each flight was flown by an off-the-shelf DJI Mavic 2 Pro using its built-in RGB camera. The 20-megapixel true-color camera has a 1” CMOS sensor with a 77° field of view. Each flight was conducted from the exact

same flight plan, resulting in 501 images per flight with near-coincident image centers. The flight altitude of 100m and overlap of 80% resulted in a ground sampling distance of approximately 2.5cm. Each flight required two batteries, so total flight time depended upon the research team's speed in replacing the battery before continuing flight.

Table 4.1. sUAS Data collection flights

Date	Flight Time	Weather	Low Tide	Note
Aug. 1 2020	1:58 PM – 2:45 PM	Partly cloudy	1:12 PM	Pre-Hurricane Isais Impact
Aug. 4 2020	3:51 PM – 4:41 PM	Partly cloudy	3:38 PM	Post- Hurricane Isais Impact
Aug. 15 2020	11:22 PM – 12:10 PM	Partly cloudy	11:48 PM	2 weeks later mission
Sept. 15 2020	12:30 PM – 1:23 PM	Mostly cloudy	1:13 PM	Beginning of normal operations
Oct. 29 2020	1:50 PM – 2:37 PM	Mostly Cloudy	1:46 PM	Data captured in between storms
Dec. 11 2020	12:04 PM – 1:03 PM	Clear	11:16 AM	Perfect sky/wind
Jan 11, 2020	12:10 PM – 12:58 PM	Overcast	12:55 PM	Captured between rain showers
Feb 9 2020	1:21 PM – 2:07 PM	Overcast	12:40 PM	Captured day after rain showers
Mar 25 2020	12:05 PM – 12:57 PM	Mostly Cloudy	12:35 PM	No shadows due to clouds
Apr 22 2020	11:30 PM – 12:20 PM	Clear	11:03 AM	Perfect sky/wind
May 22 2020	10:46 PM – 11:34 PM	Mostly Cloudy	11:23 AM	No shadows due to clouds
June 21 2020	11:55 PM – 12:46 PM	Partly Cloudy	11:49 AM	Perfect sky/wind

Flights were conducted within two hours of low tide. The spectral quality of images is affected due to the bidirectional reflectance distribution function (BRDF) as

seen by the spatial patterns of illumination in Figure 4.1. However, low tide conditions were deemed more important to the study than the BRDF effects in order to obtain the objective of getting a snapshot of the wrack placement. Importantly, the mapping of wrack was largely based on the visual interpretation on the orthomosaic that obviates the issues of automated image detection. We could visually determine the wrack locations better at low tidal periods. Other flight parameter changes, if logistically possible for all flights, would have benefited the spectral integrity of the images and are discussed in section 4.4. The logistical requirements were beyond the resources available for this study.

It has been noted that the DJI Mavic 2 Pro camera includes a rolling shutter that rapidly scans across a scene while taking the image. This is in contrast to a global shutter that takes a single image at one moment in time. The rolling shutter can introduce distortions into the images collected with this type of sensor. The processing software Pix4Mapper uses a model to compensate for the rolling shutter distortion by taking into account the movement of camera positions. According to Pix4D, the different camera positions are approximated by applying a linear interpolation between the two camera shots at the start and finish of the image readout (Pix4D, 2016). The model has shown good results with rolling shutter cameras on drone gimbal mounts to ensure the sensor is pointed constantly in the nadir (90°) position (Topodrone, 2020).

Nine ground control points (GCPs) were collected along the perimeter of the study area at permanent, unchanging locations, with similar GCP targets to the ones shown in Figure 4.2A. GCPs are not available within the marsh area due to the inaccessibility for placement of GCP targets (Figure 4.1). According to Santos Santana et

al. (2021), using GCPs for georeferencing that were placed around the perimeter of a study area performed well, especially as long as more than six GCPs are used. GCP collection was conducted using an Emlid RS2 base and rover GNSS RTK just prior to the first flight on August 1, 2020 using a NOAA survey marker as the base station (Figure 4.2B). Each GCP was collected over non-changing landmarks, and therefore could be used for recurring flights.

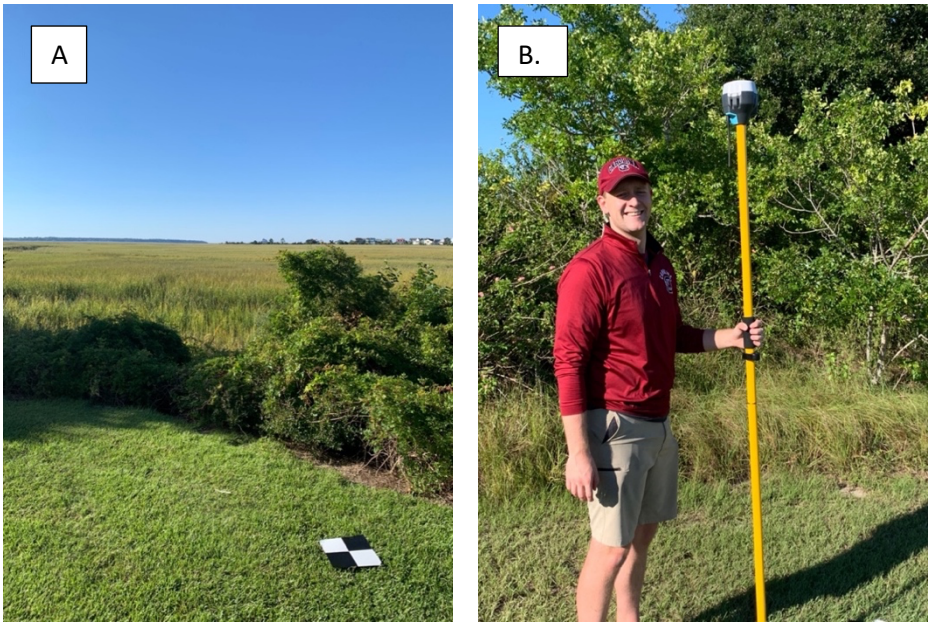

Figure 4.2. A) GCP with marsh study area in the background. B) GCP data collection with a Emlid RS2 (Rover unit pictured) GNSS unit.

4.2.3 Approaches

4.2.3.1 sUAS Data Processing

Following each flight, all 501 photos were imported into Pix4DMapper 4.6.4 where they were processed using a structure from motion (SfM) algorithm into a single orthomosaic over the whole study area. Processing required approximately two hours; usually about 20-30 minutes for initial processing and 1.5 hours for orthomosaic

generation. The ground sampling distance of sUAS images for each flight was within 0.05 m. During Pix4DMapper processing, the pixel size was resampled to 2.5 cm for all orthoimages (5x5 averaging).

4.2.3.2 Wrack Identification and Digitizing

As described by Jensen (2018), the American Society for Photogrammetry and Remote Sensing (ASPRS) defines airphoto interpretation as "the "examination of aerial photography [and aerial videography] to identify objects and judge their significance." Given the super high-resolution orthoimagery (2.5 cm), wrack identification and digitizing can be conducted following the elements of image interpretation, as described and defined by Jensen (2018). Expert visual interpreters identified each individual wrack patch, and large wrack patch clusters, using the primary elements of tone, color, and contrast in particular. The golden brown or white colored wrack is easily distinguishable from healthy green vegetation but was more difficult to distinguish from the brown dying or senesced vegetation beneath it. Different tones, however, provide enough distinction between the two for confident analysis. The tertiary visual interpretation elements of texture and pattern were equally important. Plant detritus clump together in distinct tightly clustered wrack mats when deposited by the tide or waves. The bumpy texture of wrack mats, evident in figure 4.3, make it easily discernible from the surrounding vegetation. Wrack patterns are typically quite similar over time and wrack mats are often found along tidal creeks (Reidenbaugh and Banta, 1980). This information was used when identifying wrack locations. All wrack locations were digitized into a new feature class using ArcGIS Pro version 2.8.1.

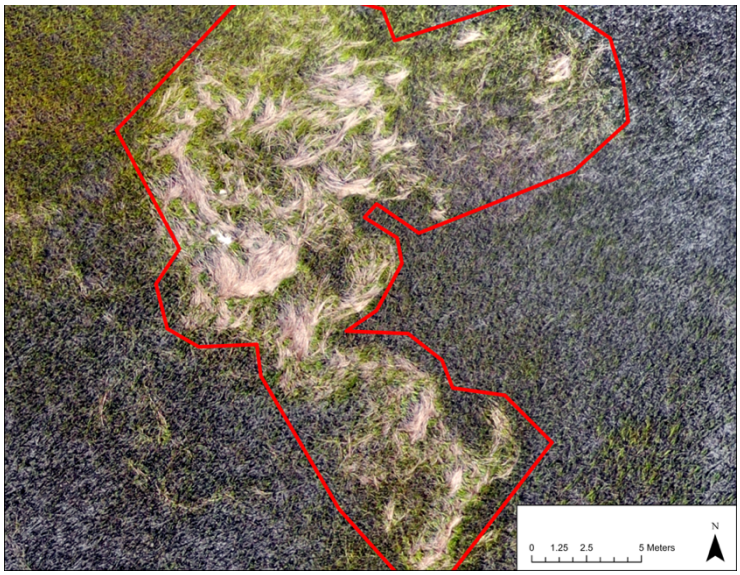

Figure 4.3. An example of a wrack cluster digitized from the orthoimage. Here, larger wrack mats, combining into a cluster, are easily discernible from the vegetation beneath.

A minimum mapping unit of a 225 cm^2 was selected for this study due to the assertion that larger wrack mats have a greater impact on the underlying vegetation. Smaller mats do not have much effect and were not considered (Valiela and Rietsma, 1995). As a result of the diversity of ways in which wrack can be found in nature, the authors have differentiated between wrack mats and wrack clusters. For the purpose of this study, wrack mats are groups of individual plant detritus to make a mat-like structure, and wrack clusters are large groups of wrack mats that can move together with the tides, as shown in figure 3.

4.2.3.3 Data Visualization and Spatial Pattern Identification

The digitized wrack polygons were processed using ArcGIS Pro 2.8.1 by first converting the vector representation of the wrack polygons into a raster data format. The

raster was generated with a 2.5 cm cell size to mimic the sUAS orthomosaicked image. Wrack locations were coded using a '1' for wrack present and '0' for wrack absence. We then used the ArcGIS Pro 2.8.1 raster calculator to add each raster together, showing changes over time. The final raster was used to make a heat map (i.e., greater frequencies of consistent wrack mats) of where wrack has occurred the most throughout the marsh system of interest (Figure 4.4). Spatial patterns in wrack presence (i.e., where wrack was consistently found and in relation to what physical characteristics of the marsh) were visually identified using the maps produced in the steps above. Example spatial patterns indicate wrack was consistently found near water bodies or in a certain region of the marsh. Descriptive statistics were performed for the digitized wrack feature classes.

Persistent wrack presence identified temporal analysis of wrack polygons was then used to further investigate the orthoimages to determine possible impacts upon surrounding vegetation. The areas experiencing vegetation disturbance were investigated systematically based on the heat map of wrack occurrence. First, the areas most prone to wrack throughout the year-long study were extracted and visually examined. The next areas investigated were typically affected by wrack for five to nine of the missions. Finally, we investigated the time series orthomosaicked images carefully one at a time to identify other areas of concern that may not have experienced persistent wrack presence.

The visual cues for unhealthy vegetation on the orthoimage include a change in color over time (that is different from natural plant senescence in the winter) and general plant structure. For example, if the vegetation was significantly impacted by wrack deposition, it would fail to rebound and stand erect again. Certainly, lack of vegetation, or exposed mudflat, is a visual cue that wrack has affected a particular vegetated area in the

marsh. For this study, areas where vegetation is missing was compared with previous aerial images of the area flown for the Beaufort County Mapping and Applications department. These images are captured during leaf-off conditions, in February or early March each year for various purposes. The spatial resolution of these images has improved in recent years to about 15-20 cm, which is enough to identify larger clusters of wrack if the image was captured during low tide. If similar vegetation gaps or mudflats existed in years prior, we assume the wrack mats had no impact. Other assumptions made here include a homogenous distribution of nutrients across the marsh system, as well as no disturbances to the marsh system. There were no known anthropogenic disturbances during the course of this study. From these assumptions, we also believe that any changes to vegetation health visually detected after the deposition of wrack was the cause of the wrack.

4.3. Results

4.3.1 Wrack presence and patterns

The spatial distribution of wrack around the marsh was consistent throughout the study. Wrack often followed tidal creeks; approximately 55% of wrack, in fact, was found within 10 m of a tidal creek (Figure 4.4). The wrack mats close to tidal creeks were typically smaller than the other wrack mats found further away. On average, the size of wrack mats and clusters closer to tidal creeks were smaller by about one square meter, per the descriptive statistics derived from the digitized wrack polygons. From figure 4.4 we can identify areas where wrack remained the longest. Generally speaking, a large portion of wrack material was displaced from regular tidal movements and small storms after a period of about three to six months. In a few instances wrack persisted beyond six

months, including some small regions in the northern sector of the marsh wrack persisted for the entire study length. While the wrack mats thinned in the winter time, they remained in place regardless of tide or other influences. Our observations conclude that the areas with persistent wrack extending beyond 6 months are mudflats along a river channel with surrounding vegetation where it is easy for wrack to enter, but difficult for it to leave. The trapped wrack mats remained for extended periods of time. Our study does not lend itself to a definitive conclusion as to why the mudflat areas exist, though it can be inferred that the geomorphological characteristics of the mudflat area give tendency to wrack deposition, and therefore wrack has persisted there long before our study was conducted. Indeed, when confirming with the aerial imagery provided by Beaufort County, there was indication of the marsh flat developing from early 2018.

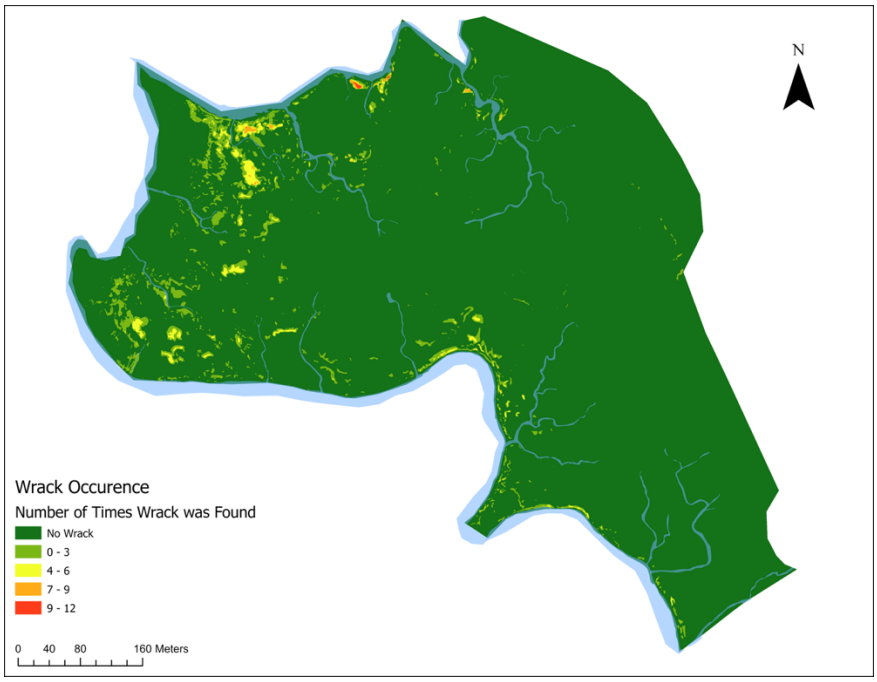

Figure 4.4. The distribution of wrack occurrences in the year-long period. Wrack deposition and movement typically occurs near the moving water bodies.

Wrack mats were most commonly found in August 2020 (324, 367, and 290 wrack mats and clusters identified) and the following June (207), indicating wrack is most prevalent in the summer for this marsh system (Figure 4.5). Winter months, particularly December (93), showed the least amount of wrack throughout the marsh. This is due to the lack of dead plant material following the several months of healthy vegetation during the season of *Spartina Alterniflora* peak biomass. There is a steep decline in wrack from August into the fall and winter until a steady increase into the summer months again. Figure 4.5 shows an obvious increase following the visit of Hurricane Isais.

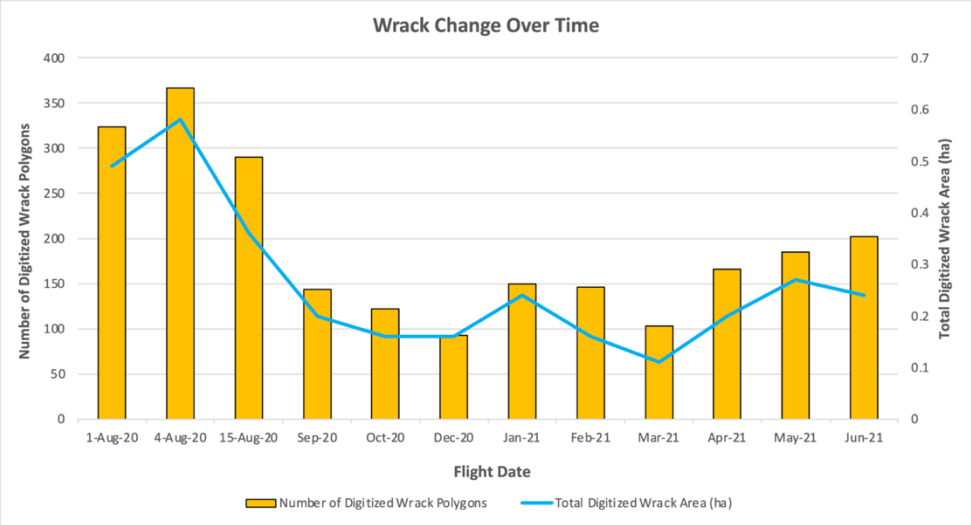

Figure 4.5. The number of wrack mats and wrack clusters on the left axis and Total Digitized wrack area in hectares on the right axis by flight date. The effects of Hurricane Isais were felt between August 1 and August 4.

Hurricane Isais on 2 August 2020 had an interesting impact on wrack movement in the marsh. The orthoimage on day 1 (August 1, 2020) was used to extract the pre-Isais wracks and the one on day 2 (August 4, 2020) was to extract the post-Isais wracks. After the storm, there were 43 more identified wrack mats or wrack mat clusters. Also, the

storm resulted in more wrack movement towards the interior of the salt marsh than any other data collection period (Figure 4.6). Wrack was deposited on the eastern (near urban) side of the marsh (red circle), which did not happen again after this incident over the yearlong study. Large new mats of wrack were also deposited on the northwestern part of the study area.

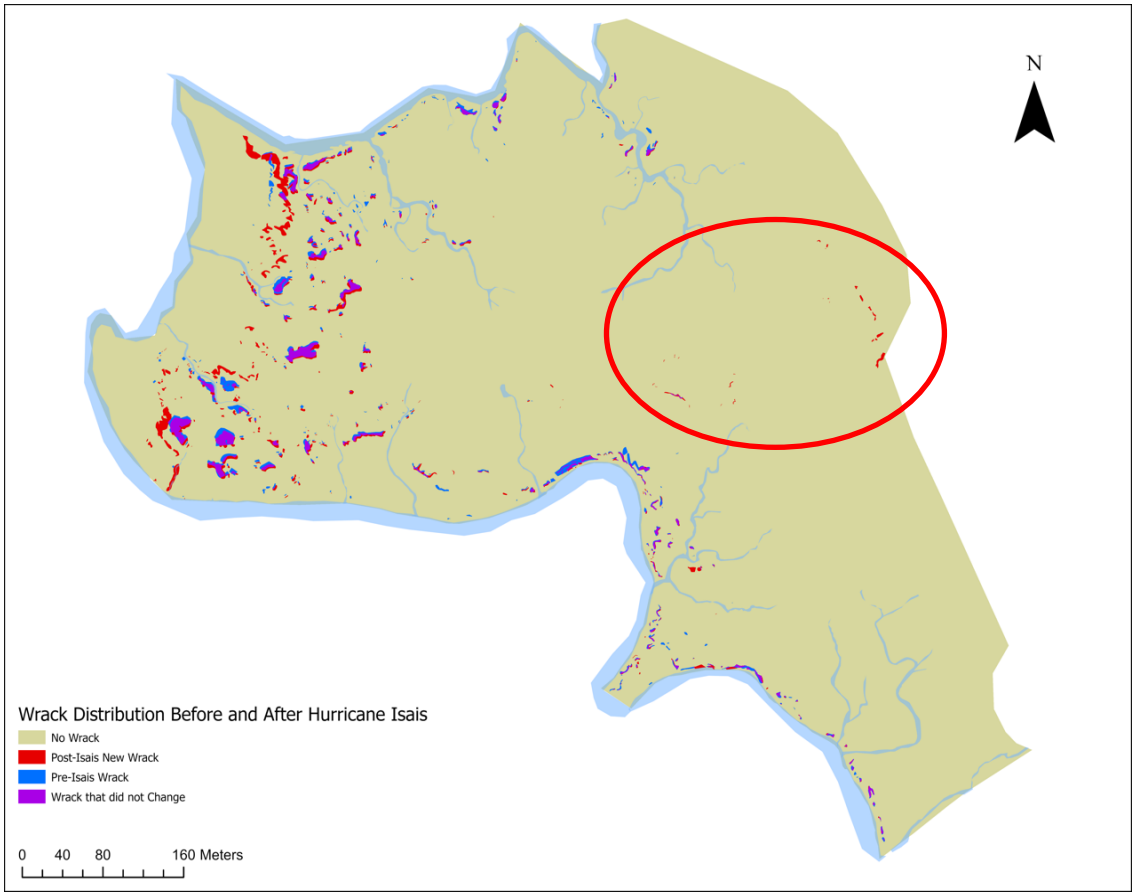

Figure 4.6. Wrack changes from before and after Hurricane Isais impacted the study area.

4.3.2 Wrack Impact on Marsh Health

Wrack presence over time was identified as an influence on vegetation. Figures 4.7, 4.8, and 4.9 identify patterns of wrack distribution and the final impact of an area

after an extended period of time. Figure 4.7 indicates an area of interest that experienced an increase in wrack presence after the impact of hurricane Isais, and slowly lost the detritus over the course of the study. However, wrack was present for at least three months (August through October). By the final flight, an area devoid of vegetation was present where wrack had been the densest. These small patches without vegetation (i.e., mudflats) in the image on the June 21 image were not found present in any of the previous three years of aerial imagery from Beaufort County.

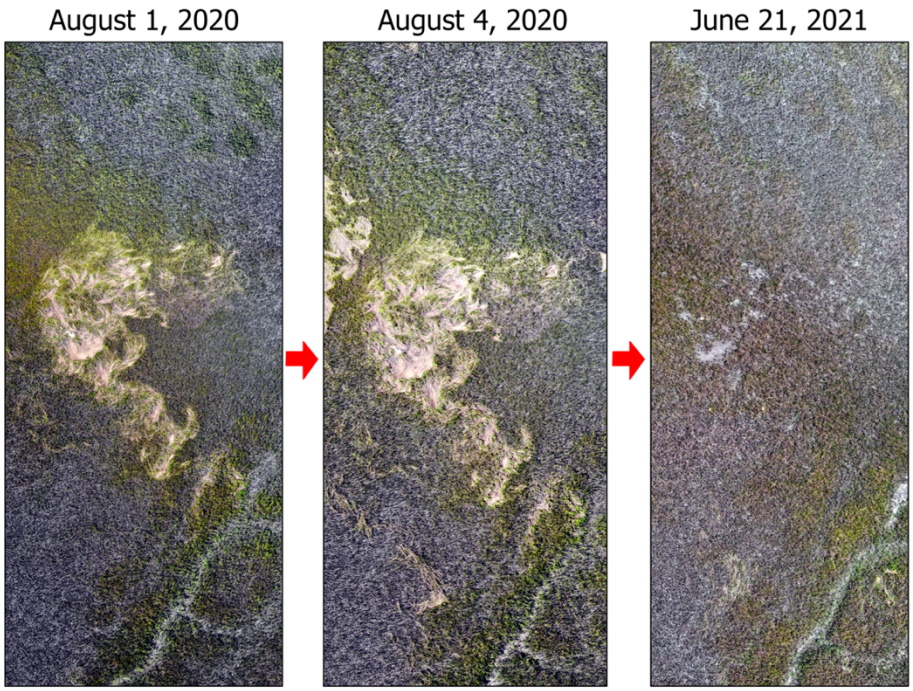

Figure 4.7. The change of a wrack before and after hurricane Isais and the eventual impact of persistent wrack presence.

Figure 4.8 represents an area where there was extensive wrack movement over the study period, resulting in some areas experiencing thinning vegetation from the previous wrack deposition and subsequent re-strengthening. More specifically, following the

movement of the wrack from the original location on August 1st 2020 to the new area on January 11th 2021 (red circles), the original area shows thin and discolored vegetation compared to the vegetation around it. This is likely a result of wrack persistence. However, after another six months, the same area in the red circle shows a thickness and greenness comparable to the vegetation around it. Other areas, like that of the densely covered area north of the channel in the January image (orange circle), had yet to experience an event strong enough to remove the wrack from the vegetation by the end of the study. The wrack, rather than move away, has fallen between the vegetation and lends itself to restrengthening.

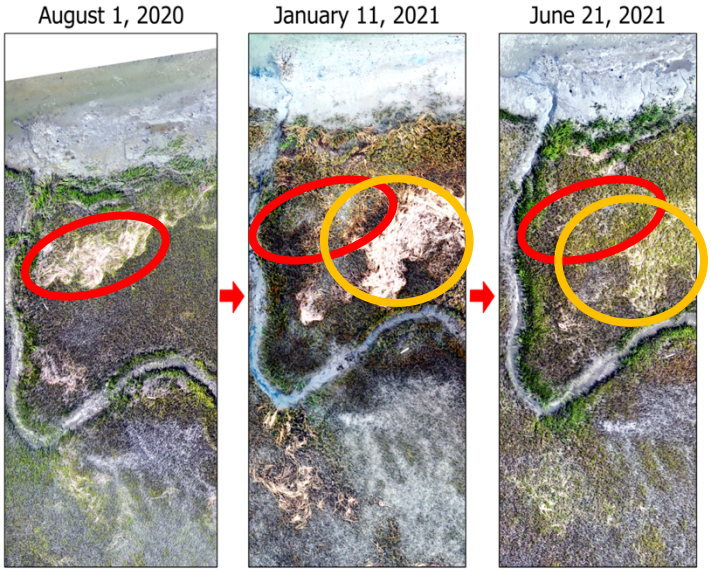

Figure 4.8. Wrack change and the eventual impact of persistent wrack presence. Red circles are the original wrack mat location while the orange circles are the locations after movement.

Figure 4.9 represents an interesting dynamic of wrack movement. The images captured depict a transition from wrack residue to a larger accumulation of wrack that

eventually intrudes deeper into the marsh system. The first image, from August 1, 2020 reveals wrack residue left behind just on the other side of a cluster of healthily green, tall form of *Spartina Alterniflora* along the tidal channel. As the season progresses to fall (shown on October 29) and then eventually to early winter, there is a growth of wrack deposition in the same location. Finally, by the end of the study, the accumulation had continued enough through the end of winter and spring to now overflow further into the marsh system.

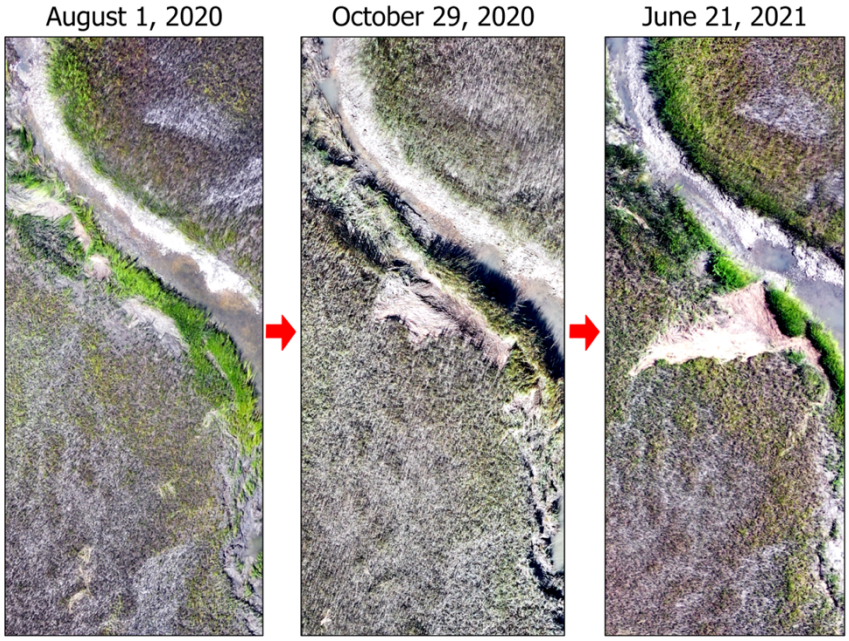

Figure 4.9. Progression from wrack residue to a small accumulation of wrack to finally a larger wrack mat overflowing into deeper parts of the marsh.

4.4. Discussion

sUAS are incredible new remote sensing tools with extensive capabilities. New advanced quadcopters have longer battery life and are able to cover a much larger study

area while also providing a stable platform for aerial photography (Boon et al., 2017). In this study, a DJI Mavic 2 Pro was used to capture aerial imagery over the 40 ha area of interest. Each flight was conducted within two hours of low tide. While logistically a challenging experiment, a long-term wrack study before and after hurricanes was shown to be a feasible pursuit. Long distance travel (2.5 hours) to the study site made the logistics and planning of sUAS missions complicated, but when planned in advance they were successful. If such a study were conducted by a coastal manager with easy access to the study area and an sUAS, a longer-term study is completely possible. The adjustable temporal and spatial resolutions of imagery, as well as the on-demand, low-cost nature of data capture, provide a unique contribution to studies of wrack and its impacts before and after coastal disturbances such as hurricanes.

Wrack was most consistently found in the northwestern portion of the study area, which happens to be closest to the large harbor river, a source of moving water for wrack transport/deposition. Few wrack mats made it to the far interior of the marsh, though a tidal channel running down the west of the study area deposited wrack along the shore frequently. Over half of all digitized wrack mats were found within 10 m of any tidal creek, which corresponds with the observations of Fischer et al. (2000). Not surprisingly, these findings provide evidence that wrack is mostly commonly found along the moving water bodies rather than farther inland from larger storm events.

While there was a substantial amount of wrack found throughout the marsh system prior to hurricane Isais impacting Harbor Island, there was both a visual and statistical increase in wrack presence after the storm passed three days later (Figures 5 and 6). The storm moved in wrack mats to areas where wrack was not found again in the

yearlong study, even two weeks after the storm had passed. While the other wrack movement throughout the year is certainly a function of regular tidal movement, these penetrating wrack mats could have been the result of compounding factors, including the usual high tide along with wind, the small amount of flooding, and small storm surge the island experienced. Many large wrack mats and clusters were found nearest the Harbor River, where much of the new wrack would be coming from upstream. From the aerial surveys conducted using the sUAS, we could determine how long wrack was in certain places. It appears that wrack deposited and moved from the storm remained in its locations for a fairly short period of time. By the time of the aerial collection on October 29, 2020, almost three months after the storm's impact, most of the wrack deposited or moved by the storm had been removed or had fallen beneath the vegetation canopy. According to Stalter et al. (2006), this would be enough time to have a mild impact on the underlying vegetation. However, more extensive negative impacts on vegetation health would require a longer persistence of wrack mats.

Wrack was also identified as a contributor to the underlying vegetation in both negative and positive ways. We found that the extended presence of wrack, as demonstrated in the area in Figure 7, contributed to the loss of vegetation. While we do not have sUAS imagery from before August 2020, we are confident that wrack was present in that area for at least three months before it was removed. Since wrack was extensively found in the area prior to Hurricane Isais, and if the wrack in that area follows the patterns found in this study, it can be inferred that wrack was present over the area for several months prior, including the summer and late spring. Therefore, we conclude that wrack presence of nearly six months could have contributed to marsh loss.

On the other hand, Figure 8 shows wrack that had at one point been on top of the vegetation but had since dropped below. With wrack below the canopy, it has a greater opportunity to decompose and benefit the vegetation rather than negatively affect it. Stalter et al. (2006) even suggests that the warm weather in South Carolina, USA could enhance and speed up the decomposition of wrack to the betterment of vegetation health.

Automatic wrack mapping with sUAS beyond visual observation is complicated. Several challenges were encountered when conducting the 12 flights and there were several lessons learned. For identifying wrack, low tide and high sun angle conditions are ideal for visually distinguishing wrack from other vegetation, particularly in the winter months. These conditions are ideal for ensuring true color images are clear and shadows are at a minimum. The low tide environment is ideal for a study on wrack because it not only limits the amount of water that affects reflectance, but also provides a snapshot of the wrack in the marsh system. The images reflect a time when most wrack movement would have halted or slowed for a short time after the waters receded. However, the flight conditions often produce BRDF effects because of the position of the nadir-viewing sensor, sun and smooth water surface in coastal marshes. Marsh environments, by their very nature, are wet and thus, result in strong direction reflective surfaces viewed from above. In extreme conditions, sun glint and hot spot effects may also occur. As was noted, BRDF effects were apparent in several of the orthomosaics due to the time of data collection, solar angle, and lack of radiometric correction. While these effects did not limit our ability to identify wrack locations for this study, it did remove the possibility of effectively using the images to calculate reliable RGB (true color) based vegetation indices for vegetation health evaluation. Two possible solutions are suggested for

overcoming these logistical problems. First, radiometric calibration targets can be used before and after flights with multispectral sensors to calibrate pixel values to true reflectance (Wang, 2021; Johnson et al., 2020; Doughty and Cavanaugh, 2019). In a previous study, BRDF effects in individual images have been successfully removed when radiometric calibration was applied in a marsh environment (Morgan et al., 2021).

Another solution to the BRDF effects is capturing images at more ideal sun angles. It has been suggested in conversation that flying in better conditions would have a bigger impact on the removal of the BRDF lines than any post-processing we can currently accomplish for sUAS imagery (G. Raber and S. Schill, personal communication, Feb. 25, 2020). It is recommended that a coastal manager would have the most control with operating during earlier hours of the day to limit the sun angle, although low tide and greater shadows in marshes should also be considered. In our particular environment, low tide occurs at the same time of day twice in a month, providing data collection windows of a few days twice a month. Careful study of tide charts and solar angles is required to carefully plan a successful flight over a marsh for investigating wrack movement.

Other limitations of future studies using an sUAS include current battery limitations. Our 40 ha area required the use of two batteries to complete the flights needed to capture the necessary images. Time wise, this typically added 10 minutes or so as the sUAS flew back to its home point, traveled to the ground, the battery was replaced, and the platform flew back to the point at which it stopped. Many flight parameters, especially cloud cover and weather, can change quickly during these short flight stoppages. As batteries improve and technology develops further, even quadcopters like

the DJI Mavic 2 Pro may have the capability to fly for longer periods of time. Such large areas can also become a problem with the Federal Aviation Administration's (FAA) requirement to maintain unaided visual line of sight with the aircraft at all times. While this was possible in our study area thanks to clear views across the marsh, some study areas and weather days may make it difficult. These logistical challenges, along with the several other tide and sun angle related difficulties, can present challenges for coastal managers in the future when attempting such studies.

The flight parameter considerations are extremely important for future work, as continued research should include long term studies on wrack distribution using a multispectral sUAS in order to capture more vegetation health metrics. Capturing data at appropriate times with proper radiometric correction can lend itself to accurate vegetation health maps from both RGB-based indices (Johnson et al., 2020; Zhou et al., 2019; Dale et al., 2020) and multispectral indices (Taddia et al., 2021; Dai et al., 2020; Doughty and Cavanaugh, 2019). Marsh elevation has also been investigated in the past with wrack deposition and storms and could be included in the study using a point cloud derived from the aerial imagery during SfM processing. Digital elevation models (DEMs) could provide insight into where wrack tends to remain after a storm, why that pattern exists, and how it can be fixed if needed.

4.5. Concluding Remarks

Long-term monitoring of wrack deposition, persistence, and its effects on marsh vegetation can be effectively conducted using an sUAS, especially before and after a hurricane. This chapter investigated the feasibility of such a study by conducting sUAS

flights over a 40 ha area of coastal tidal salt marsh from August 2020—before hurricane Isais affecting the area—until June 2021. Wrack mats and wrack mat clusters were digitized and visualized in order to identify its spatial patterns. We found that wrack, though already extensively present through the study site before the storm, increased following the storms passing. However, much of that wrack was gone after almost three months, revealing that storm deposited wrack may not be as impactful on vegetation for shorter periods of occupation. We also discovered some interesting patterns of wrack movement and impacts. For example, vegetation loss was found beneath some of the largest wrack mats following its removal over time. Wrack accumulation was also found as some wrack mats started small but over a few months' time grew to reach further into the interior of the marsh environment. Wrack was also found to have a positive influence as it decayed and provided nutrients for the vegetation to restrengthen following several months on top of the vegetation. Increased vegetation greenness and thickness several months after wrack persistence supported previous assertions of *Spartina Alterniflora* resilience to wrack coverage.

This chapter focused on the perspective of the coastal manager and demonstrates the utility of sUAS remote sensing for monitoring and mapping coastal wetlands, particularly wrack movement. The critically important temporal component of coastal management was introduced to compliment the spatial component described in chapter 3, and the fundamental principles for sUAS remote sensing investigated in chapter 2. Echoed throughout these chapters is that despite several limitations, sUAS remote sensing provides a powerful on-demand tool for monitoring coastal tidal marsh systems.

while sUAS technologies are under rapidly development, its utilization is limited to a local area restricted by the spatial extent of a flight mission. In order to examine the social component of coastal management that builds upon the spatio-temporal elements already described in previous chapters, this study turns to deep learning image classification models and large-scale LULC mapping to identify areas of concern in a county level. A coastal South Carolina county rich with coastal tidal marshes is studied. Chapter 5 introduces DL as a geospatial tool for identifying areas of social pressure from anthropogenic development near coastal tidal marshes.

CHAPTER 5

DEEP LEARNING OF HIGH-RESOLUTION AERIAL IMAGERY FOR COASTAL MARSH CHANGE DETECTION: A COMPARATIVE STUDY[4]

[4] Morgan, G. R., Wang, C., Li, Z., Schill, S. R., & Morgan, D. R. (2022). Deep learning of high-resolution aerial imagery for coastal Marsh Change Detection: A comparative study. *ISPRS International Journal of Geo-Information*, 11(2), 100. https://doi.org/10.3390/ijgi11020100. Reprinted with permission from the publisher.

5.1. Introduction

Machine learning (ML) algorithms have become commonplace in remote sensing data analysis (Camps-Valls, 2009; Lary et al., 2016; Maxwell et al., 2018; Shang and Chisholm, 2014; Hänsch et al., 2018; Peña et al., 2014; Brovelli et al., 2020; Pal and Mather, 2005). The successful use of ML for a variety of GIS and remote sensing applications has led to the implementation of these methods, often based on support vector machine (SVM) and random forests (RF) statistical methods, into GIScience software packages that can be used by non-technical investigators. The tools are readily available for supervised classifications in particular (*Train Support Vector*; *Train Random Trees*). Numerous studies have supported the use of machine learning over traditional, statistically-based classifiers such as Maximum likelihood methods, with SVM often performing the best (Ha et al., 2020; Otukei and Blaschke, 2010; Jamali, 2019; Rimal et al., 2019). ML classifiers have now been established across the professional community as reliable tools for mapping without requirement of extensive machine learning and programming experiences.

Advancements within the past ten years have led to a new division within machine learning. Deep Learning (DL) is a learning algorithm designed to mimic the function of human brain in the form of neural networks (Chassagnon et al., 2020). An advanced subsection of ML, DL is able to perform artificial intelligence functions with extensive training resources. The recent popularity and success of DL in other disciplines and applications such as speech recognition and medical image recognition has led to the rise of its use in remote sensing applications (Hinton et al., 2012; Litjens et al.,2017). While citing other reviews of DL applications in remote sensing by Liu et al. (2018) and

Zhu et al. (2017), Ma et al. (2019) gave a comprehensive review by describing different model types of DL in remote sensing. The authors also found in their meta-analysis of the subject that, as of the publication of their article, there were 221 peer reviewed articles and 181 conference papers or proceedings pertaining to remote sensing and DL. It is clear that use-cases of DL in remote sensing applications are increasing rapidly.

As applications of DL classifiers in remote sensing become more established, the algorithms and tools using DL for image classification are being made available as user-friendly graphical user interface (GUI) tools in commonly used GIS software, just like the ML tools. Though geospatial software companies tout both user-friendly and robust DL tools, it is often difficult to manipulate the tools to the user's desired specifications. Nevertheless, just as the ubiquity of ML GUI tools opened the use of ML to users without a background in programming and ML, DL tools are also now available to all. Application-driven researchers, managers, and GIScience professionals may have a difficult time choosing or knowing the appropriateness of a particular tool for a particular use-case.

A growing literature base has begun extensively testing DL classifiers against traditional ML classifiers in a variety of environments and with several data types and sizes (Liu et al., 2016; Li et al., 2016; Ghorbanzadeh et al., 2019; Hartling et al., 2019). The goal of these studies is to identify the best performing classifier by comparing the results of the classifiers on the same datasets, usually using the same or similar training and validation data. The results of these studies have thus far been inconclusive as to which classifier (DL or ML) performs best for many environments, though the current available literature can provide guidance for professionals looking to use such tools for

particular applications (e.g., land use/land cover classification, vegetation cover, coral reef habitat classification) (Jozdani et al., 2019; Nijhawan et al., 2017; Wan and Ma, 2020). Certainly, each tool should be selected based on how it best answers the research question. However, few studies have used the GUI tools developed for less-technically inclined researchers by the large GIS software companies.

The present study seeks to identify the best performing classifier (among three effective and commonly used DL and ML classifiers) for mapping land-use/land cover (LULC) using a large, complex county-wide dataset for a coastal county. Large, high resolution imagery datasets of coastal areas that include complex land cover can be more difficult to process and classify, depending on the research question, methods, quality of image, and field data. High resolution imagery can introduce a salt-and-pepper effect due to intra-class variations. Knowing which classifier performs best in this type of environment and with imagery of these specifications will especially benefit coastal managers and practitioners. This study will specifically use the ML and DL tools embedded in Esri ArcGIS Pro 2.8.1.

Three effective and commonly used ML and DL classifiers are compared in this chapter. The U-Net Convolutional Neural Network (CNN) is a DL algorithm that was originally created for biomedical image segmentation but has been now used for remote sensing image classification applications (Ronneberger et al., 2015; McGlinchy et al., 2019). The architecture of the network can be divided into two halves—the first being an encoding or ‘contracting” side and a decoding or “expansive” side— that give the architecture its “u” shape. The U-net algorithm has shown success in classifying coastal wetlands using remotely sensed imagery in previous studies (Li et al., 2021; Dang et al.,

2020). SVM and RF classifiers are commonly used ML classifiers for remote sensing analysis. The SVM classifier is a supervised classification method based on the statistical learning theory and was developed in the computer science community in the 1990s (James et al., 2013, pg. 337). It is now commonly used in remote sensing research (Liu et al., 2016; Mountrakis et al., 2011; Bahari et al., 2014). SVM classifiers are beneficial because they can handle small training samples and the training samples do not need to be normally distributed. SVM classifiers can handle non-linear class boundaries and multiple classes. The RF classifier is a supervised classification method based on the random forest statistical method (James et al., 2013, pg. 311). A series of decisions are made based on the statistical makeup of the classes and the image overall. The decisions branch out together and form what look like tree branches. When the entire image is classified, many instances of classification are performed on subsets of the data, therefore creating many decision trees (Pal, 2005). The most frequent tree output is used as the overall classification. Using multiple trees is meant to mitigate overfitting to the training samples provided by the user. The 'best' classifier will be determined by comparing time costs for classifying the imagery and overall accuracy (OA) results.

Upon determining the most effective classifier, a case study for demonstrating the effective use of the best classifier is conducted using the large county-wide data set to detect change in LULC over a ten-year period that can affect the extensive marsh environment across a large county in South Carolina, USA. While direct modification of the marsh environment for the sake of development is important to map, indirect impacts such as pollution, excessive nutrient and sewage inputs, other upstream development and freshwater diversions coming from coastal communities may have lasting negative

effects on the health of our important coastal wetlands (Kennish, 2002; Sanger et al., 2013; Hong et al., 2008; Alber et al., 2008).

Section 2 of this chapter outlines the materials and methods of the experiment and case study. This includes a description of the study area, the data used, how classifiers were trained and applied, and change detection analysis was conducted. Section 3 presents the results from the comparison and case study. Results of this case study provide insights for coastal managers to better monitor and adaptively manage for marsh health. Finally, results are discussed in the context of the current literature base, followed by a brief conclusion.

5.2. Materials and Methods

5.2.1 Approaches for Classifier Comparison Experiment

A general workflow of this study is represented in Figure 1. The experiment was performed by classifying the same large, county-wide, high-resolution aerial image, using the three different classifiers: RF, SVM, and DL U-Net. The mathematical and coding application of these classifiers were left to how the ESRI development team designed them, in ArcGIS Pro 2.8.1, in order to best represent what is available to the coastal managers and scientists with access to these common tools.

Object oriented classifiers (OOC) were used for the experiment because of their ability to mitigate some of the high-resolution, intra-class detail and salt-and-pepper phenomenon that often occurs with pixel-based classifications (Blaschke et al., 2014). While noise can still be found in the objects, object parameters can smooth out much of the salt-and-pepper effect. OOC have been shown to have better accuracy than pixel-based classifiers in a variety of environments, including salt marsh and other LU/LC

classes found in our study area (Ouyang et al., 2011; Whiteside et al., 2011; Li and Shao, 2014). The U-Net classifier performed the semantic segmentation, without the user input of a segmented image. For the SVM and RF classifications, the base image was segmented using different properties. Spectral detail was placed at the highest importance, with spatial detail coming in second. In the range of 1.0 to 20.0, spectral detail was placed at 18.5, while spatial detail was placed at an 8, in an effort to smooth out the image. Minimum segment size was placed at 5 pixels (5 × 5 m), as to accommodate smaller buildings and patches of marsh vegetation.

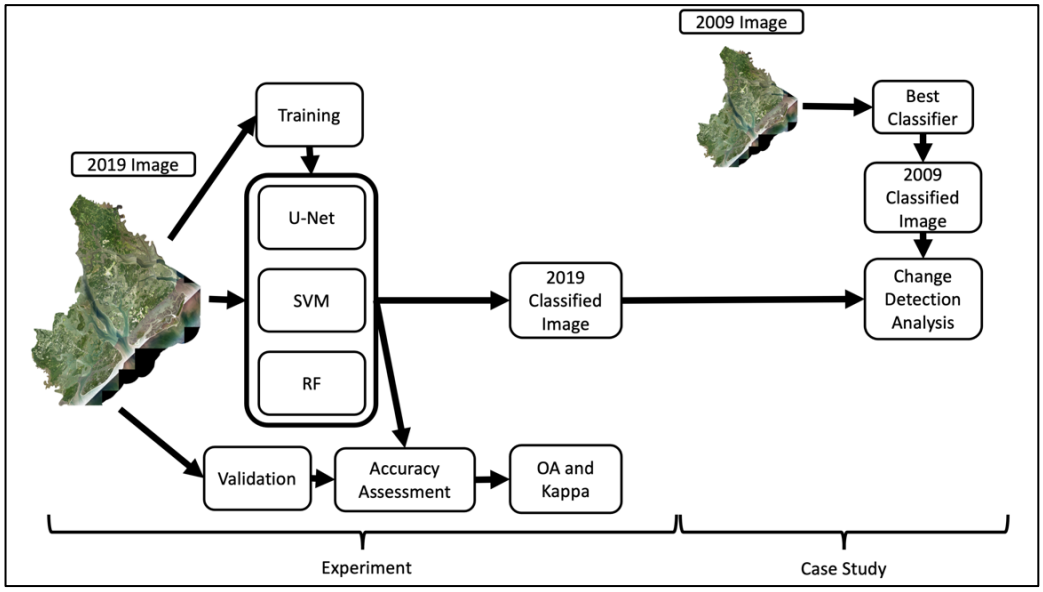

Figure 5.1. A general workflow for the experiment and case study. First, training data was used to classify the 2019 image using the three different classifiers (U-Net, SVM, and RF). Accuracy assessment was used to determine the most effective classifier. The 2009 image was classified using the best performing classifier and then compared with the 2019 image for change detection analysis.

Each classifier required certain input parameters beyond the images and training data (described in 5.2.2.2). To train the U-Net DL classifier, the training AOIs1 were used as inputs in the ArcGIS Pro's *Train Deep Learning Model* tool. To perform the

training, the entire raster image was segmented into 7169 tiles with the dimensions of 256 × 256 pixels. The training data were embedded, as well. The tool performed all of this in the software, with nothing more than a few clicks. Once the classifier was trained using the training data, and all of the small tiles were input into the U-Net classifier and ultimately classified one at a time, before being mosaicked together again to create the whole classified image. The final output was a classified image raster. The U-Net architecture includes a series of down- and up-sampling, resulting in a network with the appearance of the letter 'U'. In the first half of the architecture, sometimes referred to as the encoder, the features of the input image are extracted by 3 × 3 convolution layers, followed by a ReLU activation function and 2 × 2 maximum pooling operation. In the second half of the network, often referred to as the decoder, deconvolution occurs to restore the image back to the original resolution. Finally, a 1×1 convolution kernel is used in the final output layer (Ronneberger et al., 2015).

The simple idea behind the SVM classifier can be viewed in Figure 5.2, which is based on the maximum margin classifier (James et al., 2013). Here, a maximal margin hyperplane is computed, where the hyperplane separates out two classes and is the furthest from any of the training data. The observations that fall on the boundary, or on the outside of the extent of the hyperplane, are transformed into a 'slab.' These edge points are support vectors. However, most natural datasets cannot be separated as nicely as the example. Support vector machine classifiers allow a nonlinear decision boundary to separate the classes.

For the experiment, the SVM classifier required the input of the segmented image, training samples, and classification scheme. Only a single parameter of 500 maximum

samples per class was required, which limits the number of training samples you can use for each class. The parameter was set to the default given by ArcGIS Pro 2.8.1. Once each of the inputs were collectively used to train the SVM classifier, they were applied to the entire county-wide image. The final output was a classified image raster.

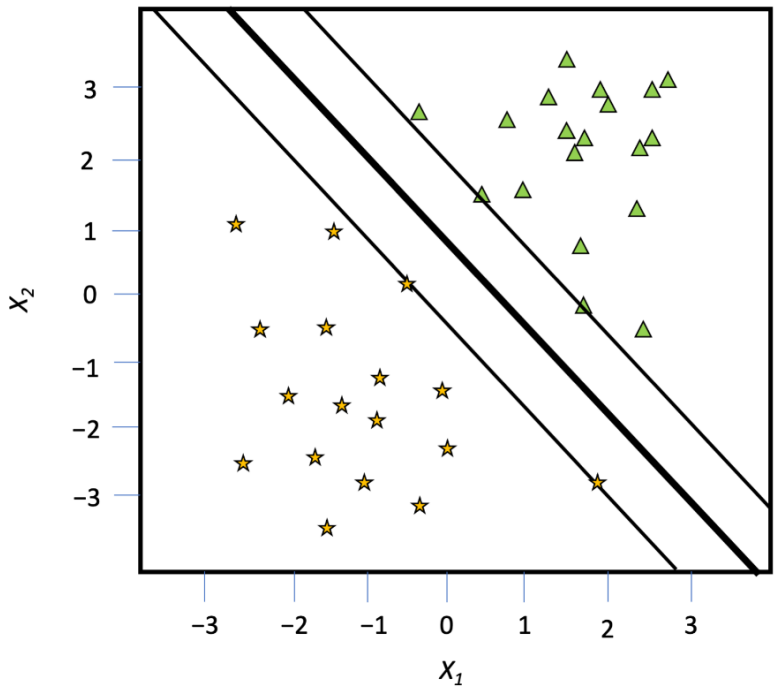

Figure 5.2. Basic SVM, in the form of a maximal margin classifier. X_1 and X_2 are hypothetical measurements and, in our case, would be pixel values.

In ArcGIS Pro, the random trees classifier is a supervised classification method, based on the random forest statistical method (James et al., 2013, p. 311). A series of decisions are made based on the statistical makeup of the classes, as well as the image overall. The decisions branch out together and form what looks like tree branches (Figure 5.3). When the entire image is classified, many instances of classification are performed on subsets of the data, therefore creating many decision trees (Pal, 2005). It is called a

random forest method is because each classification is made from a random subset of training pixels, selected from the overall image, and the final classification is based on the most frequent tree output from several trees. Using multiple trees is meant to mitigate overfitting to the training samples provided by the user.

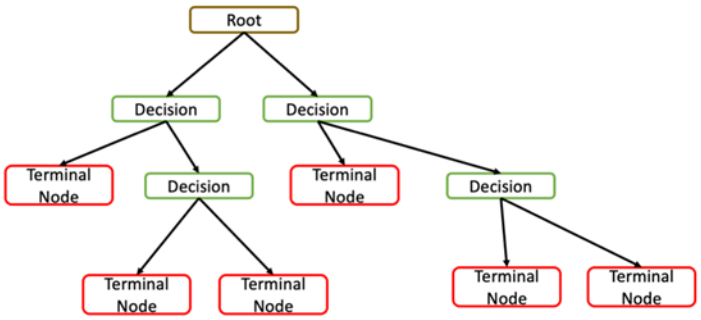

Figure 5.3. Single decision tree structure.

The RF classification followed a similar method. The same inputs were required to train the RF, though the required parameters were different. The RF classifier was trained using the following parameters: 120 maximum trees, maximum tree depth of 30, and 1000 as the maximum number of samples per class. Each of these parameters limited the size of the forest during the classifier training, while seeking to maintain a high level of accuracy.

All three classification methods were trained using the same training sample data and applied to the same aerial image composite from 2019. The final results were three classified image rasters for comparison.

Accuracy assessment metrics were used to compare the accuracy of the three classifiers. A confusion matrix was calculated using ArcGIS Pro's Compute Confusion Matrix tool, where the Producer's accuracy, User's accuracy, Overall Accuracy, and

Kappa were computed. Producer's accuracy is the total number of pixels classified correctly for a class divided by the total number of pixels in that class as determined from the ground truthing data. User's accuracy is the total number of pixels correctly classified into a class divided by the total number of pixels classified into that class. An overall accuracy (OA) percentage was also calculated:

$$\mathrm{OA} = \frac{\sum_{i=1}^{K} x_{ii}}{N} \tag{5.1}$$

where x_{ii} represents a pixel classified correctly, and N is the total number of pixels being assessed.

Kappa analysis is a multivariate technique for accuracy assessment first published in a remote sensing journal in 1983 (Congalton et al., 1983). Kappa is similar to overall accuracy as a measure of the accuracy of the entire classification, but each considers slightly different information. A kappa estimate ($\widehat{K}$) was determined as described in Jensen (2016):

$$\widehat{K} = \frac{N \sum_{i=1}^{K} x_{ii} - \sum_{i=1}^{k} (x_{i+} \times x_{+j})}{N^2 - \sum_{i=1}^{k} (x_{i+} \times x_{+j})} \tag{5.2}$$

where N is the total number of samples, k is the number of rows in the confusion matrix, x_{ii} is the number of observations in row i and column i, and x_{i+} and x_{+j} are the marginal totals for row i and column j.

5.2.2. Case Study

5.2.2.1. Study Area

Beaufort County is one of South Carolina's populous counties nestled in the southern coast of the state (Figure 5.4). From 2010 to 2019, the population in Beaufort County grew from 162,233 to 192,122, an increase of 18.4 % (US Census). It ranks as the

wealthiest county in the state with respect to the median household income at $68,377. Beaufort County is home to half of the state's salt marsh (*Port Royal Sound*). According to Purcell et al. (2020), South Carolina salt marshes and coastal wetlands provide services in the four ecosystem service categories: provisioning, regulating, cultural, and supporting. Each of these categories, though not all marketed services, provide valuable resources to coastal communities. For example, the salt marshes serve as nursery habitat to many species, especially shrimp. South Carolina's commercial fishing industry that relies upon these environments generates $42 million dollars annually to the state economy (Willis and Straka, 2016). Other services, like flood protection, carbon sequestration, filtration, and tourism all contribute to the enormous value these marshes are to the South Carolina coast. The predominate species of marsh vegetation is *Spartina Alterniflora*. *Juncus Romerianus* is also commonly found. The county is home to a diversity of several land cover types including wetlands, forests, large water bodies, extensive housing and commercial developments, and agriculture. As the county's population continues to grow in a dynamic and complex coastal environment, the importance of monitoring change using accurate classification methods is critical for future planning and measuring trends in socioeconomic and ecological health.

Despite extensive regulations to abate the environmental impacts of development on Beaufort County's salt marsh, community stakeholders continue to voice concerned for the health of the marsh (*Sea Level Rise*, pg. 33). While no substantial evidence of marsh loss was cited, additional insights from the document state that lack of monitoring in Beaufort County is a detriment to our understanding how the marsh is being affected (*Sea Level Rise*, pg. 34). Furthermore, the aforementioned Beaufort County

comprehensive plan does not address marsh migration in the face of sea level rise (*Beaufort County Comprehensive*). In addition to comparing DL algorithm competency in mapping a large, complex county wide image with other ML classifiers, this study seeks to fill a gap in the understanding of land use/land cover extent changes in the area that may be directly or indirectly impacting marsh health.

Figure 5.4 Map of the United States with Beaufort County (in red) highlighted within South Carolina (highlighted in blue) and its NAIP image acquired in 2019.

5.2.2.2. Data

The aerial imagery used in this study were collected by the National Agriculture Imagery Program, or NAIP. This program began in 2002 and is administered by the U.S. Department of Agriculture (USDA) Farm Service Agency to collect aerial imagery during growing seasons. The digital sensors used for NAIP imagery, though not apparent

in the metadata provided with the imagery, meet rigid calibration specifications (Davis, 2017). NAIP imagery is generally collected at a 1 m spatial resolution (50-60 cm in some areas) across the conterminous United States.

Table 5.1 Aerial Imagery Details.

Image Characteristics	2009 Image	2019 Image
Dates	April 16-25, 2009	August 29- Spetember 23 2019
Pixel Size	1 m	60 cm
Sensor	Leica Geosystems ADS40-SH52	Leica Geosystems ADS100
Tidal Range	Variable; High or low depending on the area	Variable; High or low depending on the area
Plant Phenology	Early stages	Peak Plant Biomass
Masked Image Size	21.7 gb	10.8 gb

For this study, NAIP images of Beaufort County acquired in 2009 and 2019 were used (Table 5.1). The imagery varies in the month collected. For the 2009 NAIP imagery, each tile in the orthomosaic was collected between April 16 and April 25, 2009. The 2009 imagery is a traditional true color orthomosaic, with a 1 m spatial resolution captured by a Leica Geosystems ADS40-SH52 sensor (sensor numbers 30028 and 30045). The 2019 imagery was collected between August 29 and September 23, 2019. The 2019 flights resulted in a 60 cm spatial resolution and true color imagery from a

Leica Geosystems ADS100 model sensor (sensor numbers 10530 and 10552). The pixel size was resampled to 1 m to match the 2009 image. The tide of each image varied, even within an image due to the flight times of each tile that makes up the images. In general, the 2009 image shows higher tides with much of the lower marsh slightly inundated. The National Wetland Inventory (NWI) shapefile for South Carolina was used to mask out deep water bodies while retaining marsh areas (Download Seamless). After masking, the imagery was reduced to a smaller size and became more manageable for classifications. Both images were transformed into the NAD83 (2011) UTM 17N coordinate system.

5.2.2.2. Case Study Classification and Analysis Methods

Both NAIP images were classified into several level 1, 2, and 3 LULC classes, loosely based on (Anderson et al., 1976). The level 3 classes included mudflat, marsh vegetation, forest, roads, buildings, agriculture, grassland, water, shadows, dry bare ground and wet bare ground (Table 5.2). Several classes were combined in our level 2 classes to leave 7 predominant classes that described the general LULC in the study area. For example, mudflat and marsh vegetation were combined into the marsh class, roads and buildings into the urban class, and dry and wet bare ground into a single bare ground class. It was determined that the agriculture class and grass classes were significantly confused, and therefore were combined due to their similarities. These combinations were made to identify general environments and limit unnecessary misclassifications.

A final set of level 1 classes were determined by combining bare ground, urban, and grass/agriculture into a developed class that was used as a proxy for general LULC changes that can impact marsh health. Bare ground was included in development because construction sites and pre-construction sites across the county are typically bare ground.

Grass is included as a development class because it represents a loss of natural forested coastal area. Many parks and yards are part of developments, and this is where grass is found. Further, while agricultural use may be impactful if the farmer is using certain chemicals, the same could be said for large grass areas where added nutrients can eventually reach the wetlands through runoff. In the end, the forest and development classes were deemed the most important for determining changes that would affect marshes. Aside from determining the actual marsh changes (i.e., development on marsh or marsh gain through marsh restoration), the changes in forested land and increase in development were used as an indicator of how marsh may be affected.

Table 5.2. Classes used in this study at each classification level.

Level 3 Class	**Level 2 Class**	**Level 1 Class**
Mudflat	Marsh	Marsh
Marsh Vegetation	Marsh	Marsh
Forest	Forest	Forest
Roads	Urban	Development
Buildings	Urban	Development
Agriculture	Ag/Grass	Development
Grassland	Ag/Grass	Development
Dry Bare Ground	Bare Ground	Development
Wet Bare Ground	Bare Ground	Development
Water	Water	Water
Shadows	Shadows	Shadows

Areas of interest (AOIs) for training and validation samples were manually digitized from the 1 m NAIP imagery based on expert knowledge in the study area and field visits within the last two years. Training samples were gathered visually from the imagery in collaboration with the Beaufort County Mapping and Applications Director, who has had residence in the position since 1995.

Table 5.3. Number of Training and Validation samples (area in ha).

Level 3 Class	**2009 Training AOIs**	**2009 Validation AOIs**	**2019 Training AOIs**	**2019 Validation AOIs**
Mudflat	103 (48.7)	68 (140.4)	100 (98.7)	57 (28.9)
Marsh Vegetation	174 (932.3)	71 (193.5)	112 (344.6)	61 (115.4)
Underwater Marsh	104 (578.1)	56 (120.3)	103 (278.8)	46 (134.8)
Forest	120 (887.4)	88 (534.0)	101 (882)	42 (218.6)
Roads	128 (71.5)	66 (30.3)	129 (61.1)	54 (11.4)
Buildings	510 (28.6)	301 (10.2)	656 (35.5)	400 (12.6)
Agriculture	144 (532.6)	74 (102.1)	104 (313.9)	35 (71.4)
Grassland	101 (87.1)	56 (50.2)	103 (119.6)	64 (29.8)
Dry Bare Ground	101 (187.6)	62 (61.3)	113 (206.6)	64 (48.2
Wet Bare Ground	102 (66.1)	40 (50.4)	101 (26.8)	46 (12.3)
Water	132 (138.5)	65 (46.2)	123 (90.0)	53 (18.6)
Shadows	174 (3)	109 (1.4)	119 (3.5)	65 (1.3)

A portion of the open-source building footprints layer provided by Microsoft was used as AOIs for the building class (Microsoft, n.d.; Huang et al., 2020). While the dataset was produced in 2018, the individual tiles or scenes throughout the imagery

collected in a wide variety of dates. Therefore, a Beaufort County building footprints subset was thoroughly examined before usage as ancillary training and validation data. Over 100 training AOIs were generated for each level 3 class, though all polygons were not equal in size. As a result, several classes had fewer AOIs but very large areas for training the classifiers. Since the study area was exceptionally large (nearly 2,400 km^2), there was ample space to define a large number of training and validation samples (Table 5.3).

An accuracy assessment was performed for each classified image using the validation AOIs generated in a similar manner to the training AOIs. Validation AOIs were a fraction of total AOIs for any given class. AOIs were combined for accuracy assessment to reflect level 2 classes, which were of more interest than the level 3 individual classes. Regardless of the number of validation AOIs, a stratified random sample of 1500 validation points were generated for the validation process within the given validation AOIs for each image (Figure 5.5). The validation points were then used to calculate the accuracy assessment metrics described in 5.2.1.

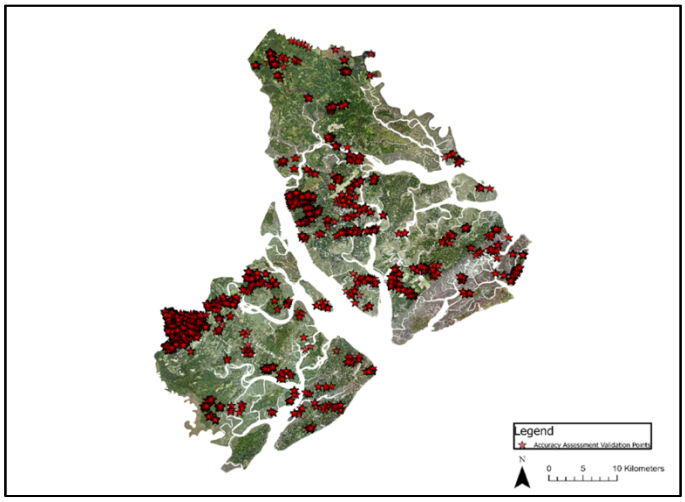

Figure 5.5. Distribution of sample points used for accuracy assessment across Beaufort County.

Following the classification of both the 2019 and 2009 images of Beaufort County, a change detection analysis was conducted using the Change Detection tool in ArcGIS pro v.2.8.1. The tool requires an input of a series of maps or images and computes a change detection map and change matrix in return. For the change detection analysis, a final classification map with combined classes was created. Water, shadows, marsh, and forest classes remained intact, but the agriculture/grass, bare ground, and urban classes were combined into a class called development. Areas of change were assessed based on the numbers of pixels that changed from a particular class to another. Pixel counts were multiplied by the 1 m * 1 m pixel size to determine approximate area in meters squared. Further conversion from m^2 to ha was accomplished by multiplying by 0.0001.

While mapping a marsh class alone gives us direct information on actual changes in the marsh, many indirect impacts from nearby land use/land cover changes have been documented (Sanger et al., 2013; Wedge et al., 2015). Because of these documented impacts, we decided to map all classes to suggest and discuss what changes may potentially occur if development trends continue.

Pixels that changed from any particular class to the shadow class, or from the shadow class to another class were disregarded for this change analysis. The pixels of interest for this study were the pixels that changed from the marsh class or the forest class to any other class, but particularly to the development class. The pixels that experienced these changes were mapped and visually analyzed to determine impacts and assess potential future impacts. This was done through visual observation based on the change detection analysis.

5.3. Results

5.3.1. Comparison of model performance and accuracies

Processing time is an important factor in processing large-size imagery. Computational costs depend on the data being processed as well as the computational abilities of the machine being used. Here, a Dell Inspiron 5680 6-core intel i7 CPU with 16gb Ram and Nvidia GTX 1060 3gb GPU was used to process each classification. As noted in Table 1, the U-Net classifier required the least training time but the most total classification time to apply the trained model to the image.

Table 5.4. Computational time and classification accuracies.

Classifier	Training Time	Classification Time	OA	Kappa
2019 DL U-Net	2 hours, 59 minutes	43 hours, 23 minutes	92.4%	89.8%
2019 SVM	4 hours, 52 minutes	30 minutes	81.6%	75.3%
2019 RF	4 hours, 29 minutes	23 minutes	75.7%	67.3%
2009 DL U-Net	2 hours, 46 minutes	42 hours, 34 minutes	85.3%	80.5%

Training the U-net classifier required 2 hours and 59 minutes, at least 30 minutes faster than the two other classifiers. However, the classification of the image itself took 43 hours and 23 minutes for a total of 46 hours and 22 minutes. The length of classification is not a common finding, however, as U-net classifiers have been found to be faster than many others in remote sensing applications (Li et al., 2021; Dang et al., 2020; Zhang et al., 2021). The authors suggest the extra length of time required to complete classification was due to the machine specifications, the size of the dataset, and

the methods by which the tiles were classified and subsequently mosaicked together. The SVM classifier required 4 hours 52 minutes for training and then 30 minutes to classify the image. The RF classifier was trained in 4 hours 29 minutes and was applied to the image in approximately 23 minutes. The computational times and classification accuracies are reported in Table 5.4.

The overall accuracies of the three classifiers for the 2019 image ranged from 75.74% to 92.38%, with the U-Net classifier performing the best (Table 5.4). This study found the object-based ML classifiers did not perform as well, though certain classes performed well (Tables 5.5, 5.6 and 5.7). The forest class was consistently classified with high users and producers' accuracy (99-89%). Other classes varied based on the classifier. For example, the SVM and RT classifiers correctly classified marsh at least 70% of the time, though the U-net Classifier had a user's accuracy of 84.41% and a producer's accuracy of 93.52%. However, both ML classifiers interestingly confused marsh with the urban class the most. It is proposed that the high-resolution imagery and complex environment lead to a high intra-class variability, making it difficult for the ML classifiers to separate the classes.

Table 5.5. Accuracy for the predominant Level 2 classes (U-net).

Classes	Marsh	Forest	Urban	Agriculture/Grass	Bare Ground	Total	Users Accuracy
Marsh	260	2	8	2	28	308	84.42%
Forest	2	592	1	0	0	596	99.33%
Urban	0	0	283	0	10	294	96.26%

Agriculture/Grass	6	12	11	123	3	156	78.85%
Bare Ground	10	0	0	3	84	97	86.60%
Total	278	608	307	129	125	1509	
Producer's Accuracy	93.53%	97.37%	92.18%	95.35%	67.20%		

Table 5.6. Accuracy for the predominant Level 2 classes (SVM).

Classes	Marsh	Forest	Urban	Agriculture/Grass	Bare Ground	Total	Users Accuracy
Marsh	217	6	10	1	19	263	82.51%
Forest	0	561	1	1	1	567	98.94%
Urban	37	7	273	11	63	400	68.25%
Agriculture/Grass	22	9	10	111	10	167	66.47%
Bare Ground	2	0	9	5	32	49	65.31%
Total	278	608	307	129	125	1509	
Producer's Accuracy	78.06%	92.27%	88.93%	86.05%	25.60%		

Table 5.7. Accuracy for the predominant Level 2 classes (RF).

Classes	Marsh	Forest	Urban	Agriculture/Grass	Bare Ground	Total	Users Accuracy
Marsh	201	19	15	4	11	260	77.31%

Forest	2	541	12	6	0	573	94.42%
Urban	55	23	265	0	73	448	59.15%
Agriculture/Grass	8	24	10	105	0	152	69.08%
Bare Ground	12	0	5	14	41	72	56.94%
Total	278	608	307	129	125	1509	
Producer's Accuracy	72.30%	88.98%	86.32%	81.40%	32.80%		

After finding the U-Net classifier performed the best, it was applied to the 2009 NAIP dataset as well. Overall accuracy of the 2009 image classification was 85.28%, with a Kappa statistic of 80.45%. While many of the same classes performed remarkably well between the two sets of imagery, the tidal ranges within the 2009 image seems to have proved difficult for the U-net classifier. The producer's accuracy for the marsh class was a low 65.18%, though the user's accuracy was 96.90%. The marsh areas were often confused for the water class or the agriculture/grass class. The agriculture/grass class was often confused as well. It is suggested that this was due to the image collection during peak biomass, when *S. Alterniflora* is its greenest and most like an agricultural product or grass. Outside of the marsh class and the bare ground class that was confused for urban areas, all other classes resulted in a producer's accuracy of at least 90.0%.

5.3.2. Comparison of classification results

The DL U-Net classifier was able to navigate the complexities of the environment better than the other ML classifiers and achieved a higher accuracy. Evidence of this assertion can be found in three subset areas with classification challenges. Figure 5.4 shows a forested and agricultural area in northern Beaufort County. It is classified reasonably well by U-Net (Fig. 5.4A), which shows very little salt-and pepper effect in

the classification. However, SVM and RF (Fig. 5.4B-C) misclassified the forest as water, marsh or shadow depending on the hue of the green space. Portions of the marsh on the western edge of the image were confused for bare ground by RF, though the U-net and SVM classifiers generally recognized it to be marsh. SVM also misclassified small portions of the marsh area as urban area. U-Net struggled with wet areas in and around inland water bodies, classifying surrounding vegetation as marsh.

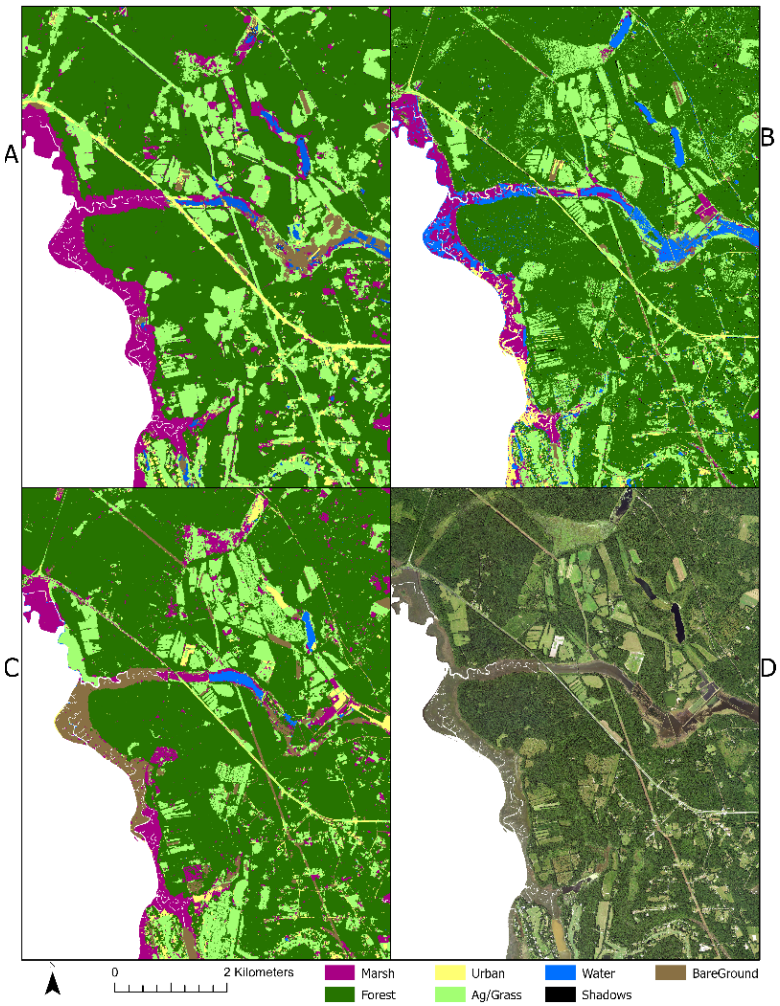

Figure 5.6. A mixed-use area classified by A) U-net, B) SVM and C) Random Forest. D) is the NAIP image of this subset.

In another subset area under development (Figure 5.5), U-Net (Figure 5.5A) once again classifies the bare ground areas correctly, along with the extensive suburban areas. SVM similarly classified most of the bare ground and urban areas correctly. However, RF misclassified the bare ground areas as urban areas. Another difficulty for each classifier was differentiating some wetland areas and ponds in neighborhoods and golf courses from the marsh. SVM and U-Net occasionally misclassified those areas, while RF struggled the most. Nearly every inland water body was misclassified as marsh by the RF classifier.

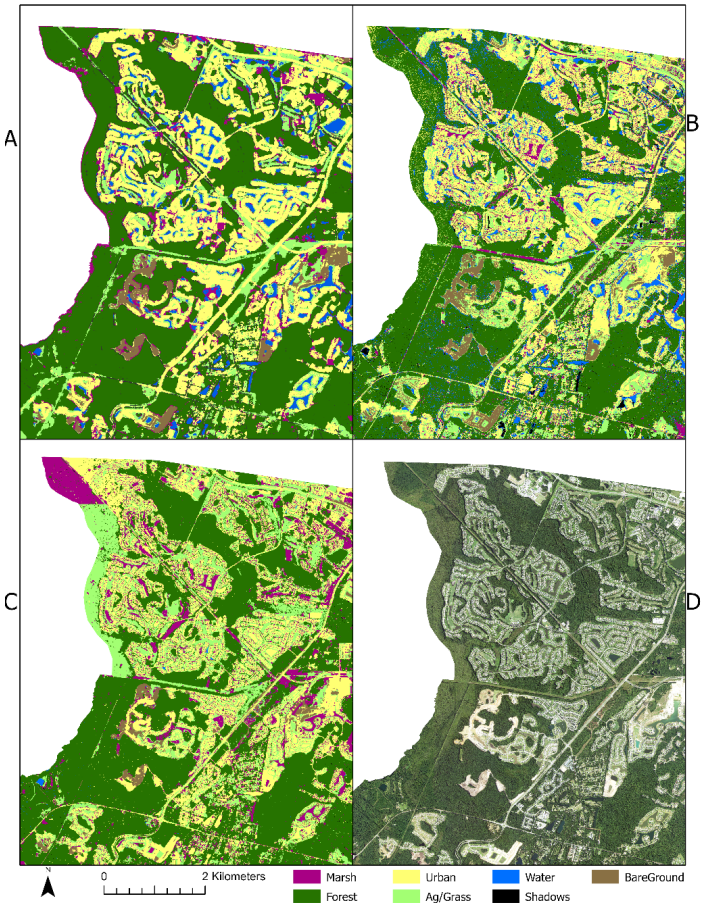

Figure 5.7. A developing area classified by A) U-net, B) SVM, and C) Random Forest. D) is the NAIP image of this subset.

It is well known that marsh extent is difficult to map, especially when the tidal range varies throughout the imagery. These tidal discrepancies made classifying the marsh difficult for each classifier in this study (Figure 5.6). Marsh was sometimes misclassified as water, urban, bare ground, and even grass. If images were collected during low tide conditions across the entire study area, classifications could have been more accurate. Water hues ranging from blue to algae-ridden green waters made classifications of water and grass difficult as well. Ancillary information, such as texture, RGB-based indices, or even a DEM might assist in the differentiation between some of the more troubled classes. Some inland areas in and around small ponds were also misclassified as marsh. This is similar to RF that struggled to differentiate the water class from the marsh class in nearly every inland pond (as shown in Figure 5.5C).

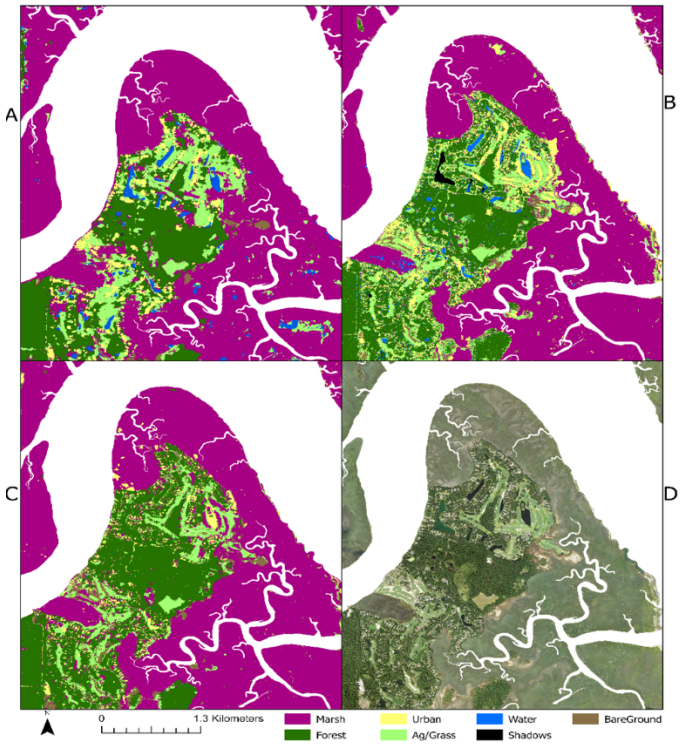

Figure 5.8. A marsh area classified by A) U-net, B) SVM, and C) Random Forest. D) is the NAIP image of this subset.

5.3.3 Coastal Development and Impact to Marshes

After the DL U-net classifier was applied to both the 2019 and 2009 images, changes between the two dates were assessed visually and, as best as possible, quantitatively. The 2009 image classification struggled to classify marsh correctly in some areas, assigning some pixels as development (i.e., the urban, grass/agriculture, or bare ground classes) rather than marsh. With this knowledge, it is apparent that several areas that were marked as marsh loss or gain were in fact errors made by the classifier. These areas were visually inspected. Figures 5.7C and 5.7D indicate two areas where actual changes did occur, and in fact some marsh vegetation was lost. An overall marsh system loss was estimated at 3,300 ha. However, because of the errors detected extensively throughout the 2009 marsh class in particular, a quantitative assessment of marsh losses may not be completely trusted. To reiterate the issues described above, the producer's accuracy of the marsh class in the 2009 image was only 65%, the lowest of all the classes. The marsh was misclassified as urban area because of sun glint, and sometimes as agriculture due to its greenness. We used expert visual observation to determine that there was very little true marsh loss over the ten-year period. There were a few areas where marsh vegetation extent expanded between dates (Figure 5.7A and 5.7B), but there were no detected areas where the marsh vegetation or mudflat were directly affected by development in the marsh system. Tidal levels throughout both images made classifications and comparisons difficult. Despite using a separate class for submerged or underwater marsh, these areas are where much of the misclassifications occurred among the marsh class. Further work using ancillary datasets, like a DEM of the entire county, to facilitate classification should provide better results in the future.

Figure 5.9. Examples of marsh vegetation gain (A and B) and loss (C and D) from 2009 to 2019.

Large areas of development expansion were detected across the county. This study indicates that approximately 7,102.74 ha of forest were lost to other land cover classes (e.g., urban, bare ground, and grass/agriculture). For the purposes of the case study, any forest lost to the level 1 development class was deemed development. The development in northern Beaufort County included small areas of urban development and large areas of agricultural development. Southern Beaufort County saw the greatest amount of urban growth. Figure 5.8 indicates the area of development across the county. On the other hand, some previously urban areas from 2009 were naturalized over the past 10 years. Some agricultural and urban areas from 2009 were overtaken by shrubs and

small trees over the ten-year period. These areas were often then classified as forest and were counted as lost developed land.

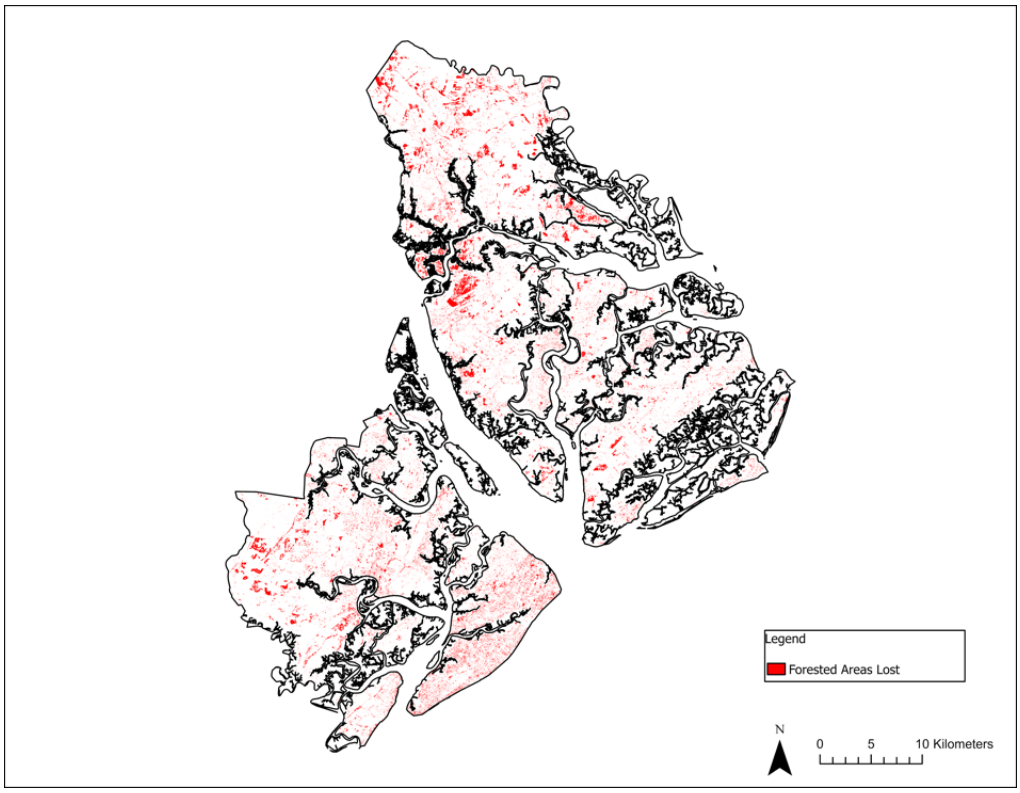

Figure 5.10. Forested areas lost to development across Beaufort County in 2009-2019.

5.4. Discussion

The DL, SVM, and RT classification results fared well when compared to other large-area DL mapping studies that included wetlands and other complex land cover classes. For large scale wetland mapping across Alberta Canada, DeLancey et al. (2019) achieved an 80.2% OA using a deep CNN. In a study comparing RF, SVM, and three other deep learning classifiers for classifying wetland using small unmanned aerial systems hyperspatial resolution imagery, Liu et al. (2018) found that the DL classifiers performed better than the SVM and RF classifiers, especially when the training sample

counts were high. RF and SVM classifiers resulted in OA as high as 65% and 67%, respectively. The DL classifiers resulted in OA upwards of 76% to 84%. Similarly, our results support assertions made by Mahdianpari (2018) that CNN can outperform RF classifiers. Specifically, U-Net has shown to outperform SVM and RF classifications for wetland mapping using Sentinel-2 10 m imagery. Dang et al. (2020) discovered that the SVM and RT classifiers only achieved an OA of 50.5% and 46.4%, respectively, while the U-Net classifier regularly reached at least 85%, depending on the optimizing function used. Our study suggests the higher resolution NAIP imagery includes enough spatial detail to improve the OA to the detected levels of accuracy (e.g., U-Net = 92.4%; SVM = 81.6; RT = 75.7%). When using a similar spatial resolution data from the Worldview 3 satellite to classify forested wetlands using a DL CNN, Du et al. (2020) found similar accuracy levels as our study (92%) when only the optical imagery was used.

In this study, all three classifiers showed a fair amount of competency in classifying large, complex aerial image mosaics. Other applications where these classifiers, especially the highest performing DL U-net classifier, might be of use include tree cover mapping, disaster assessment using imagery directly after a storm event or natural disaster, sUAS imagery classification, and species level mapping. The classifiers can be considered adequate for these purposes because of the results from this study, indicating that high resolution imagery can be processed quickly and with high accuracy. In some of these examples, time can be an important factor, and when that is the case the SVM and RF classifiers have been shown in this study to provide adequate results quickly (2-3 hours) for even a large, 2,400 km^2 study area.

Several challenges were faced when classifying the coastal tidal marsh in Beaufort County for this study. Maneuvering the tide, and water levels in general, is a significant challenge when using remotely sensed imagery to map coastal wetlands, including coastal tidal marshes (Gallant, 2015). This was particularly evident in this study, as event within the NAIP imagery for one county there was a significant difference across the tiles that made up the image in tide levels. This was one of the major difficulties in classifying the marsh. Other environmental conditions such as cloud cover and shadows cast by tall objects (like buildings, trees, and water towers) obscured the target wetlands, complicated spectral signatures, and made optical imagery difficult to interpret or use (Tiner, 2015, pg. 43-65). Plant phenology also played a factor in image classification. Peak biomass conditions are best for modeling plant health characteristics such as biomass and can be beneficial in mapping certain coastal wetland species (O'Donnell and Schalles, 2016; Doughty and Cavanaugh, 2019). The 2009 imagery was taken in April, which is at the beginning stages of growth and greening up for *S. Alterniflora*, the dominant marsh grass in Beaufort County. The 2019 imagery was taken in late august and early September, which is in the peak biomass for S. Alterniflora (Ai et al., 2017). All three classifiers were more successful at classifying the marsh class in the 2019 imagery than the U-net classifier was in the 2009 image. We propose that plant phenology, along with tide levels throughout each image, was a significant factor in these results.

NAIP datasets provide high resolution aerial imagery with great potential for vegetation mapping, in particular when acquired during leaf-on conditions. While we found a fair amount of success mapping various classes, including the marsh class, the

NAIP RGB imagery alone was not sufficient to overcome all of the complexities of the coastal wetland environment. To better classify the coastal tidal marsh, particularly the vegetation and mudflat, it would be expedient to incorporate ancillary remote sensing data. This process, called data fusion, can be used to better describe and classify wetlands (Lang et al., 2015). Data fusion can be performed at the pixel-level, feature-level, and decision-level. Dehouck et al. (2012), as described in Ramsey III and Rangoonwala (2015), found that they could improve land cover classification by fusing multispectral data with radar data. While the increase in overall accuracy (OA) was small, some sub classes improved while others decreased slightly in classification accuracy. Difebo et al. (2015) applied a fusion of multispectral imagery with LiDAR-derived elevation datasets to map peatlands in Canada with a 76.4% OA opposed to only achieving a 65.8% with the RGB and IR bands. Data fusion is able to provide better information for decision makers. For example, the addition of a NIR band or a vegetation index such as the Normalized Difference Vegetation Index (NDVI) provides greater discrimination between marsh vegetation and mudflat, as well as marsh vegetation from other vegetation classes. Elevation data derived from LiDAR or other sources improves feature extraction of trees, agriculture, and grasses from the marsh grasses and even mudflats.

Potential biases and errors introduced in the study may be introduced in the selection of training and validation AOIs by the researchers. Potential bias was mitigated by involving multiple long-term residents of the county who interpreted the aerial imagery and selected the training and validation polygons based on extensive local knowledge.

Future work should incorporate ancillary remotely sensed data into the classification process to further increase classification accuracy. As previously stated, other spectral bands and indices, elevation data, and imagery from other scales (i.e., small unmanned aerial systems) should be examined to produce a data fusion product of potentially higher accuracy. Results from LULC classifications can be used as input into models for other phenomenon, like water quality (Schill and Jensen, 2000). Water quality is another element that can impact marsh health. Further trials with other available deep learning pixel classifiers, such as DeepLabv3, are useful tools to be investigated as well. These methods could be further validated through application and testing in similar coastal environments.

5.5. Concluding Remarks

This chapter compared DL with traditional ML classifiers based on the classification of high-resolution imagery over an entire coastal county using GUI applications from ArcGIS Pro 2.8.1. Our case study then used the LULC maps from 2019 and 2009 to detect salt marsh change patterns over a 10-year period. Results indicated that a U-Net DL classifier significantly outperformed the other classifiers for the classification of a complex, high resolution county-wide dataset in terms of OA (92.4% as opposed to the 81.6% by SVM and 75.7% by RF). DL algorithms now available to any coastal manager or GIS analyst with access to Esri's ArcGIS pro showed their high applicability to large-area mapping. Using computational resources commonly available to coastal managers and professional GIS analysts, the U-net classification required a longer time to classify the large dataset (46 total hours vs 5.33 hours and 4.83 hours). Because this was not found among other literature regarding other U-Net classifiers, we

believe the time required for classification was a function of the large dataset, computational resources, and DL model structure.

Chapter 5 focused on DL and ML classifiers from the perspective of the environmental or coastal manager. Findings indicate a bright future for DL and ML LULC classification for large-area mapping, even for those without complicated programming and DL or ML backgrounds. Our case study demonstrated the power of using these tools for change detection, showing large areas of development over a 10-year period across the county that may have an impact on marsh health. Further research is needed to validate findings and test similar methods across similar complex coastal environments. Additional ancillary remote sensing data, including multispectral and hyperspectral imagery, LiDAR, and RADAR, can be integrated to improve classification accuracy.

CHAPTER 6

CONCLUSION

Coastal tidal marshes Coastal tidal marshes are essential ecosystems for the health of our coasts. Several factors, including anthropogenically driven factors like climate change, sea level rise, and pollution, have persistent impact on coastal tidal marshes and necessitate regular monitoring. Multiple dimensions of coastal monitoring, including spatial, temporal, and social, are important considerations for a comprehensive coastal management plan. Thankfully, developing geospatial technologies like sUAS and DL are perfect fits for many of the current gaps in monitoring tidal marsh.

This dissertation has collectively built a metaphorical tower of geospatial technology applications to reach more efficient and effective coastal monitoring (as shown in figure 1.1). Chapter 2 poured a foundation of understanding regarding the use of sUAS for monitoring of coastal wetland vegetation. Chapters 3 and 4 built upon that foundation by using sUAS to gather imagery over a coastal tidal marsh to model the spatial distribution of *S. Alterniflora* biomass and the spatio-temporal distribution of vegetation-affecting wrack. Chapter 5 looked to employ advanced Deep Learning technologies for exploring social pressures being applied to tidal marsh at a county level beyond the abilities of a sUAS.

Chapter 2 offered a review and synthesis of the current literature pertaining to sUAS use for remote sensing of coastal wetland vegetation. Since 2016 there was a perceptible increase in literature regarding the use of sUAS in coastal vegetation

research, and signs point to a continued increase as sUAS and sensors become even more cost efficient and widely available. Several benefits to using sUAS for monitoring coastal wetland vegetation were identified, including limited time-related and financial costs; the on-demand nature of deployment; added context for decision making; higher density of LiDAR points from LiDAR sensors; ability to add multiple sensors; and a few other site-specific benefits. A multitude of sensors, flight altitudes, GCP counts, applications and methods of analysis were successfully used in the selected literature base and described in chapter 2. Several limitations were also identified. These were related to using ground control points; balancing altitude, image overlap, and battery capacity; legal restrictions; environmental limitations; and computational requirements of the data. Overall, there was an increasing use of sUAS platforms for mapping and monitoring coastal vegetation and the challenges outweigh the limitations for a variety of applications. However, as sUAS platforms continue to be upgraded and new and improved sensors become more readily available and cost-effective, the applications and capabilities of sUAS for remote sensing of coastal vegetation will continue to grow.

Chapter 3 built upon the foundation established in chapter 2 to develop an RGB index-based biomass model from sUAS imagery in order to observe its spatial dynamics in a coastal tidal marsh system. Most off-the-shelf sUAS that coastal managers are likely to have access to are fitted with RGB cameras, and so RGB-indices were designed to be the focus of this experiment. Flights were conducted during the time of peak biomass for *S. Alterniflora*, the marsh vegetation of interest. Several flight parameters were based on parameters discovered from the literature review of chapter 2. RGB-indices, along with a CHM to estimate vegetation height, were calculated from the collected imagery. A

quadratic statistical model was established for estimating biomass from these with these extracted indices. The optimal RGB index for estimating biomass was the Excess Green index (ExG) with the RMSE = 0.598 kg/m^2 and R^2 = 0 .376. The extracted biomass maps fairly reflected the spatial variations of biomass at three marsh sites. Height metrics from the sUAS point cloud, relying on LiDAR-derived bare earth model, did not significantly enhance our biomass models. While future work is required to fine-tune parameters and work to produce a better model, chapter 3 established the use of sUAS in a coastal marsh for monitoring spatial phenomenon as a sure possibility for coastal managers.

Chapter 3 cracked the surface of observing coastal marshes, and chapter 4 capitalized on sUAS on-demand deployment capabilities to introduce the spatio-temporal component of coastal monitoring. Very seldom do coastal managers or researchers want a static picture of the marsh system at any one time. sUAS are easy to deploy and can provide high spatial and temporal resolution data on-demand. Time series data can provide important insights into any tidal marsh system. In chapter 4, an sUAS was flown over a 40 ha area of coastal tidal salt marsh in a monthly basis from August 2020—before hurricane Isais affecting the area—until June 2021. The imagery was used to monitor tidal wrack deposition, persistence, and spatial distribution from before a hurricane event, after a hurricane event, and up to 11 months following the hurricane event. Wrack mats and wrack mat clusters were digitized and visualized in order to identify its spatial patterns. We found that wrack, though already extensively present through the study site before the storm, increased following the storms passing. However, much of that wrack was gone after almost three months, revealing that storm deposited wrack may not be as impactful on vegetation for shorter periods of occupation. We also discovered some

interesting patterns of wrack movement and impacts. For example, vegetation loss was found beneath some of the largest wrack mats following its removal over time. Wrack accumulation was also found as some wrack mats started small but over a few months' time grew to reach further into the interior of the marsh environment. Wrack was also found to have a positive influence as it decayed and provided nutrients for the vegetation to restrengthen following several months on top of the vegetation. Increased vegetation greenness and thickness several months after wrack persistence supported previous assertions of *Spartina Alterniflora* resilience to wrack coverage.

sUAS are not the only rapidly developing geospatial technology in acquiring and analyzing high-resolution imagery on coast. In Chapter 5, a DL classifier was compared with traditional ML classifiers in an effort to establish which classifier is best for our given application: identifying social or anthropogenic pressures and marsh loss based on the classification of high-resolution imagery over an entire coastal county. The social component is an incredibly important management consideration during the Anthropocene. In addition to spatial and temporal analysis, identifying how humans are influencing the marshes is key. Our case study extracted the LULC maps from 2019 and 2009 to detect salt marsh change patterns over a 10-year period. Results indicated that a U-Net DL classifier significantly outperformed the other classifiers for the classification of a complex, high resolution county-wide dataset in terms of OA (92.4% as opposed to the 81.6% by SVM and 75.7% by RF). DL algorithms now available to any coastal manager or GIS analyst with access to Esri's ArcGIS pro showed their high applicability to large-area mapping. Using computational resources also commonly available to coastal managers and professional GIS analysts, the U-net classification required a longer time to

classify the large dataset (46 total hours vs 5.33 hours and 4.83 hours). This chapter focused on DL and ML classifiers from the perspective of the environmental or coastal manager. Findings indicate a bright future for DL LULC classification for large-area mapping, even for those without complicated programming and DL backgrounds. Our case study demonstrated the power of using these tools for change detection, showing large areas of development over a 10-year period across the county that may have an impact on marsh health.

This dissertation established the utility of the new sUAS and DL geospatial technologies in meeting the challenges and needs of a changing, and ever-threatened, coastal tidal marsh environment. The dissertation also advanced future coastal management and monitoring, as well as future sUAS and DL related studies in the coastal environment, by providing a thorough literature review, demonstrating the application if sUAS for modeling marsh biomass, establishing the feasibility of a long-term sUAS-based study for a marsh system, and determining the optimal classifier for large-scale county-level classification for a complex, developing coastal county. The methodologies, results, and other findings discussed within are meant to benefit application driven GIScientists and coastal managers in the coastal marsh realm to mitigate future negative impacts and expand our understanding of how we can protect such majestic environments.

REFERENCES

Abeysinghe, T., Simic Milas, A., Arend, K., Hohman, B., Reil, P., Gregory, A., & Vázquez-Ortega, A. (2019). Mapping invasive Phragmites australis in the old Woman CREEK Estuary Using uav remote sensing and machine learning classifiers. *Remote Sensing*, *11*(11), 1380. https://doi.org/10.3390/rs11111380

About the refuge - ernest F. hollings ace basin - U.S. fish and wildlife service. U.S. Fish & Wildlife Service. (n.d.). Retrieved January 3, 2022, from https://www.fws.gov/refuge/ACE_Basin/about.html

Adade, R., Aibinu, A. M., Ekumah, B., & Asaana, J. (2021). Unmanned aerial Vehicle (UAV) applications in coastal zone Management—a review. *Environmental Monitoring and Assessment*, *193*(3). https://doi.org/10.1007/s10661-021-08949-8

Ai, J., Gao, W., Gao, Z., Shi, R., & Zhang, C. (2017). Phenology-based Spartina alterniflora mapping in coastal wetland of the Yangtze Estuary using time series of GaoFen satellite no. 1 wide field of view imagery. *Journal of Applied Remote Sensing*, *11*(2), 026020. https://doi.org/10.1117/1.jrs.11.026020

Akaike, H. (1974). A new look at the statistical model identification. *IEEE Transactions on Automatic Control*, *19*(6), 716–723. https://doi.org/10.1109/tac.1974.1100705

Alber, M.; Swenson, E. M.; Adamowicz, S. C.; Mendelssohn, I. A. (2008) Salt marsh dieback: an overview of recent events in the US. *Estuarine, Coastal and Shelf Science*, *80*(1), 1-11.

Anderson, J. R., Hardy, E. E., Roach, J. T., & Witmer, R. E. (1976). A land use and land cover classification system for use with Remote Sensor Data. *Professional Paper*. https://doi.org/10.3133/pp964

Bahari, N. I., Ahmad, A., & Aboobaider, B. M. (2014). Application of support vector machine for classification of Multispectral Data. *IOP Conference Series: Earth and Environmental Science*, *20*, 012038. https://doi.org/10.1088/1755-1315/20/1/012038

Ballard, J.; Pezda, J.; Spencer, D. (2016). An economic valuation of Southern California coastal wetlands. Master's Thesis. University of California, Santa Barbara.

Barr, J. R., Green, M. C., DeMaso, S. J., & Hardy, T. B. (2018). Detectability and Visibility biases associated with using a Consumer-Grade unmanned aircraft to survey Nesting colonial waterbirds. *Journal of Field Ornithology*, *89*(3), 242–257. https://doi.org/10.1111/jofo.12258

Beaufort County Comprehensive Plan Chapter 5. Available online: https://www.beaufortcountysc.gov/council/comprehensive-plan/documents/2010-comprehensive-plan-documents/chapter-5-natural-resources.pdf (accessed on 20 Nov 2021).

Berni, J., Zarco-Tejada, P. J., Suarez, L., & Fereres, E. (2009). Thermal and narrowband multispectral remote sensing for Vegetation monitoring from an unmanned aerial vehicle. *IEEE Transactions on Geoscience and Remote Sensing*, *47*(3), 722–738. https://doi.org/10.1109/tgrs.2008.2010457

Bhardwaj, A., Sam, L., Akanksha, Martín-Torres, F. J., & Kumar, R. (2016). UAVs as remote sensing platform in glaciology: Present applications and future prospects. *Remote Sensing of Environment*, *175*, 196–204. https://doi.org/10.1016/j.rse.2015.12.029

Blaschke, T., Hay, G. J., Kelly, M., Lang, S., Hofmann, P., Addink, E., Queiroz Feitosa, R., van der Meer, F., van der Werff, H., van Coillie, F., & Tiede, D. (2014). Geographic object-based image analysis – towards a new paradigm. *ISPRS Journal of Photogrammetry and Remote Sensing*, *87*, 180–191. https://doi.org/10.1016/j.isprsjprs.2013.09.014

Boon, M. A., Drijfhout, A. P., & Tesfamichael, S. (2017). Comparison of a fixed-wing and multi-rotor UAV for environmental mapping applications: A case study. *The International*

Archives of the Photogrammetry, Remote Sensing and Spatial Information Sciences, *XLII-2/W6*, 47–54. https://doi.org/10.5194/isprs-archives-xlii-2-w6-47-2017

Breaux, A., Farber, S., & Day, J. (1995). Using natural coastal wetlands systems for wastewater treatment: an economic benefit analysis. *Journal of Environmental Management*, 44(3), 285-91.

Brewer, J. S., Levine, J. M., & Bertness, M. D. (1998). Interactive effects of elevation and burial with Wrack on plant community structure in some Rhode Island Salt Marshes. *Journal of Ecology*, *86*(1), 125–136. https://doi.org/10.1046/j.1365-2745.1998.00241.x

Brooks, C. N., Grimm, A. G., Marcarelli, A. M., & Dobson, R. J. (2019). Multiscale collection and analysis of submerged aquatic Vegetation Spectral profiles for Eurasian Watermilfoil Detection. *Journal of Applied Remote Sensing*, *13*(03), 1. https://doi.org/10.1117/1.jrs.13.037501

Broussard, W. P., Visser, J. M., & Brooks, R. P. (2020). Quantifying vegetation and Landscape metrics With Hyperspatial unmanned aircraft system imagery in a Coastal Oligohaline Marsh. *Estuaries and Coasts*. https://doi.org/10.1007/s12237-020-00828-8

Brovelli, M. A., Sun, Y., & Yordanov, V. (2020). Monitoring Forest change in the Amazon using multi-temporal remote sensing data and Machine Learning Classification on google earth engine. *ISPRS International Journal of Geo-Information*, *9*(10), 580. https://doi.org/10.3390/ijgi9100580

Camps-Valls, G. (2009). Machine learning in Remote Sensing Data Processing. *2009 IEEE International Workshop on Machine Learning for Signal Processing*. https://doi.org/10.1109/mlsp.2009.5306233

Cao, J., Leng, W., Liu, K., Liu, L., He, Z., & Zhu, Y. (2018). Object-based mangrove species classification using unmanned aerial vehicle hyperspectral images and digital surface models. *Remote Sensing*, *10*(2), 89. https://doi.org/10.3390/rs10010089

Cen, H., Wan, L., Zhu, J., Li, Y., Li, X., Zhu, Y., Weng, H., Wu, W., Yin, W., Xu, C., Bao, Y., Feng, L., Shou, J., & He, Y. (2019). Dynamic monitoring of biomass of rice under different nitrogen treatments using a lightweight UAV with dual image-frame snapshot cameras. *Plant Methods*, *15*(1). https://doi.org/10.1186/s13007-019-0418-8

Chassagnon, G., Vakalopoulou, M., Régent, A., Zacharaki, E. I., Aviram, G., Martin, C., Marini, R., Bus, N., Jerjir, N., Mekinian, A., Hua-Huy, T., Monnier-Cholley, L., Benmostefa, N., Mouthon, L., Dinh-Xuan, A.-T., Paragios, N., & Revel, M.-P. (2020). Deep learning–based approach for automated assessment of interstitial lung disease in systemic sclerosis on CT images. *Radiology: Artificial Intelligence*, *2*(4). https://doi.org/10.1148/ryai.2020190006

Clark, J. R. (2000). *Coastal Zone Management Handbook*. Lewis Publishers.

Collin, A., Dubois, S., James, D., & Houet, T. (2019). Improving intertidal Reef mapping Using uav surface, Red edge, and near-infrared data. *Drones*, *3*(3), 67. https://doi.org/10.3390/drones3030067

Colomina, I., & Molina, P. (2014). Unmanned aerial systems for photogrammetry and Remote Sensing: A Review. *ISPRS Journal of Photogrammetry and Remote Sensing*, *92*, 79–97. https://doi.org/10.1016/j.isprsjprs.2014.02.013

Congalton, R.; Oderwald, R. G.; Mead, R. (1983). Assessing Landsat classification accuracy using discrete multivariate statistical techniques. *Photogrammetric Engineering and Remote Sensing*, 1671–1678.

Dai, W., Li, H., Chen, X., Xu, F., Zhou, Z., & Zhang, C. (2020). Saltmarsh expansion in response to morphodynamic evolution: Field observations in the Jiangsu Coast using UAV. *Journal of Coastal Research*, *95*(sp1), 433. https://doi.org/10.2112/si95-084.1

Dale, J., Burgess, H. M., Berg, M. J., Strong, C. J., & Burnside, N. G. (2021). Morphological evolution of a non-engineered managed realignment site following tidal inundation.

Estuarine, Coastal and Shelf Science, *260*, 107510. https://doi.org/10.1016/j.ecss.2021.107510

Dale, J., Burnside, N. G., Hill-Butler, C., Berg, M. J., Strong, C. J., & Burgess, H. M. (2020). The Use of Unmanned Aerial Vehicles to Determine Differences in Vegetation Cover: A Tool for Monitoring Coastal Wetland Restoration Schemes. *Remote Sensing*, *12*(24), 4022. https://doi.org/10.3390/rs12244022

Dang, K. B., Nguyen, M. H., Nguyen, D. A., Phan, T. T., Giang, T. L., Pham, H. H., Nguyen, T. N., Tran, T. T., & Bui, D. T. (2020). Coastal wetland classification with deep U-Net Convolutional Networks and sentinel-2 imagery: A case study at the Tien Yen Estuary of Vietnam. *Remote Sensing*, *12*(19), 3270. https://doi.org/10.3390/rs12193270

Datta, A., Maharaj, S., Prabhu, G. N., Bhowmik, D., Marino, A., Akbari, V., Rupavatharam, S., Sujeetha, J. A., Anantrao, G. G., Poduvattil, V. K., Kumar, S., & Kleczkowski, A. (2021). Monitoring the spread of water hyacinth (pontederia crassipes): Challenges and future developments. *Frontiers in Ecology and Evolution*, *9*. https://doi.org/10.3389/fevo.2021.631338

Davis, D. National Agriculture Imagery Program (NAIP) Information Sheet. (2017). https://www.fsa.usda.gov/Assets/USDA-FSA-Public/usdafiles/APFO/support-documents/pdfs/naip_infosheet_2016.pdf.

Davis, J. L., Currin, C. A., O'Brien, C., Raffenburg, C., & Davis, A. (2015). Living Shorelines: Coastal Resilience with a Blue Carbon Benefit. *PLOS ONE*, *10*(11). https://doi.org/10.1371/journal.pone.0142595

Davis, J., Currin, C., & Morris, J. T. (2017). Impacts of Fertilization and Tidal Inundation on Elevation Change in Microtidal, Low Relief Salt Marshes. *Estuaries and Coasts*, *40*(6), 1677–1687. https://doi.org/10.1007/s12237-017-0251-0

Dehouck, A., Lafon, V., Baghdadi, N., & Marieu, V. (2012). Use of optical and radar data in synergy for mapping intertidal flats and coastal salt-marshes (arcachon lagoon, France).

2012 IEEE International Geoscience and Remote Sensing Symposium. https://doi.org/10.1109/igarss.2012.6350837

DeLancey, E. R., Simms, J. F., Mahdianpari, M., Brisco, B., Mahoney, C., & Kariyeva, J. (2019). Comparing deep learning and shallow learning for large-scale wetland classification in Alberta, Canada. *Remote Sensing*, *12*(1), 2. https://doi.org/10.3390/rs12010002

Difebo, A., Richardson, M., & Price, J. (2015). Fusion of Multispectral Imagery and LiDAR Digital Terrain Derivatives for Ecosystem Mapping and Morphological Characterization of a Northern Peatland Complex. In *Remote Sensing of Wetlands: Applications and Advances* 1st ed.; R.W. Tiner, M.W. Lang & V.V. Klemas (Eds.); CRC Press, pp. 399-412.

DiGiacomo, A. E., Bird, C. N., Pan, V. G., Dobroski, K., Atkins-Davis, C., Johnston, D. W., & Ridge, J. T. (2020). Modeling Salt Marsh Vegetation Height Using Unoccupied Aircraft Systems and Structure from Motion. *Remote Sensing*, *12*(14), 2333. https://doi.org/10.3390/rs12142333

Digital Coast Data. (n.d.). Available online: https://coast.noaa.gov/digitalcoast/data/home.html (accessed on 20 March 2021).

DJI - official website. DJI Official. (n.d.). Retrieved June 17, 2021, from https://www.dji.com/

Doughty, C. L., Ambrose, R. F., Okin, G. S., & Cavanaugh, K. C. (2021). Characterizing spatial variability in coastal wetland biomass across multiple scales using UAV and satellite imagery. *Remote Sensing in Ecology and Conservation*. https://doi.org/10.1002/rse2.198

Doughty, C., & Cavanaugh, K. (2019). Mapping Coastal Wetland Biomass from High Resolution Unmanned Aerial Vehicle (UAV) Imagery. *Remote Sensing*, *11*(5), 540. https://doi.org/10.3390/rs11050540

Download Seamless Wetlands Data by State. Available online: https://www.fws.gov/wetlands/data/State-Downloads.html (accessed on (20 Nov 2021)

Doyle, T. (2016, May 11). *Effect of hurricane wrack deposition on coastal marsh surface elevation change*. U.S. Geological Survey. Retrieved July 3, 2020, from https://www.usgs.gov/centers/wetland-and-aquatic-research-center/science/effect-hurricane-wrack-deposition-coastal-marsh

Du, L., McCarty, G. W., Zhang, X., Lang, M. W., Vanderhoof, M. K., Li, X., Huang, C., Lee, S., & Zou, Z. (2020). Mapping forested wetland inundation in the Delmarva Peninsula, USA using deep convolutional Neural Networks. *Remote Sensing*, *12*(4), 644. https://doi.org/10.3390/rs12040644

Durgan, S. D., Zhang, C., & Duecaster, A. (2020a). Evaluation and enhancement of unmanned aircraft system photogrammetric data quality for coastal wetlands. *GIScience & Remote Sensing*, *57*(7), 865–881. https://doi.org/10.1080/15481603.2020.1819720

Durgan, S. D., Zhang, C., Duecaster, A., Fourney, F., & Su, H. (2020b). Unmanned aircraft system photogrammetry for mapping diverse vegetation species in a heterogeneous coastal wetland. *Wetlands*, *40*(6), 2621–2633. https://doi.org/10.1007/s13157-020-01373-7

Ebee x fixed-wing mapping and surveying drone. senseFly. (2021, June 14). Retrieved June 17, 2021, from https://www.sensefly.com/drone/ebee-x-fixed-wing-drone/.

Enwright, N., Wang, L., Borchert, S., Day, R., Feher, L., & Osland, M. (2017). The Impact of Lidar Elevation Uncertainty on Mapping Intertidal Habitats on Barrier Islands. *Remote Sensing*, *10*(2), 5. https://doi.org/10.3390/rs10010005

Fairley, I., Mendzil, A., Togneri, M., & Reeve, D. (2018). The use of unmanned aerial systems to Map Intertidal Sediment. *Remote Sensing*, *10*(12), 1918. https://doi.org/10.3390/rs10121918

Fallati, L., Saponari, L., Savini, A., Marchese, F., Corselli, C., & Galli, P. (2020). Multi-Temporal UAV data and Object-Based image Analysis (obia) for estimation of Substrate

changes in A Post-bleaching scenario on a Maldivian Reef. *Remote Sensing*, *12*(13), 2093. https://doi.org/10.3390/rs12132093

Farris, A. S., Defne, Z., & Ganju, N. K. (2019). Identifying salt marsh shorelines from remotely sensed elevation data and imagery. *Remote Sensing*, *11*(15), 1795. https://doi.org/10.3390/rs11151795

Fischer, J. M., Reed-Andersen, T., Klug, J. L., & Chalmers, A. G. (2000). Spatial pattern of localized disturbance along a southeastern salt marsh tidal creek. *Estuaries*, *23*(4), 565. https://doi.org/10.2307/1353146

Gallant, A. (2015). The challenges of remote monitoring of wetlands. *Remote Sensing*, *7*(8), 10938–10950. https://doi.org/10.3390/rs70810938

Gao, Z., Wang, Q., Cao, X., & Gao, W. (2014). The responses of vegetation water Content (EWT) and assessment of drought monitoring along a coastal region using remote sensing. *GIScience & Remote Sensing*, *51*(1), 1–16. https://doi.org/10.1080/15481603.2014.882564

García-López, S., Ruiz-Ortiz, V., Barbero, L., & Sánchez-Bellón, Á. (2018). Contribution of the UAS to the determination of the water budget in a Coastal Wetland: A case study in the natural park of the Bay of Cádiz (sw spain). *European Journal of Remote Sensing*, *51*(1), 965–977. https://doi.org/10.1080/22797254.2018.1522602

Ghorbanzadeh, O., Blaschke, T., Gholamnia, K., Meena, S., Tiede, D., & Aryal, J. (2019). Evaluation of different machine learning methods and deep-learning convolutional neural networks for landslide detection. *Remote Sensing*, *11*(2), 196. https://doi.org/10.3390/rs11020196

Gross, M.F., Klemas, V., Levasseur, J. E. (1988). Remote sensing of biomass of salt marsh vegetation in France. *International Journal of Remote Sensing*, *9*(3), 397–408. https://doi.org/10.1080/01431168808954863

Ha, N. T., Manley-Harris, M., Pham, T. D., & Hawes, I. (2020). A comparative assessment of Ensemble-based machine learning and maximum likelihood methods for mapping seagrass using sentinel-2 imagery in Tauranga Harbor, New Zealand. *Remote Sensing*, *12*(3), 355. https://doi.org/10.3390/rs12030355

Hanson, A., Johnson, R., Wigand, C., Oczkowski, A., Davey, E., & Markham, E. (2016). Responses of Spartina alterniflora to Multiple Stressors: Changing Precipitation Patterns, Accelerated Sea Level Rise, and Nutrient Enrichment. *Estuaries and Coasts*, *39*(5), 1376–1385. https://doi.org/10.1007/s12237-016-0090-4

Hardin, P. J., & Jensen, R. R. (2011). Small-scale unmanned aerial vehicles in environmental remote sensing: Challenges and opportunities. *GIScience & Remote Sensing*, *48*(1), 99–111. https://doi.org/10.2747/1548-1603.48.1.99

Hardisky, M. A., Klemas, V., & Daiber, F. C. (1983). Remote sensing salt marsh biomass and stress detection. *Advances in Space Research*, *2*(8), 219–229. https://doi.org/10.1016/0273-1177(82)90243-5

Hardisky, M.; Smart, R.; Klemas, V. (1983). Seasonal spectral characteristics and aboveground biomass of the tidal marsh plant Spartina alterniflora. *Remote Sens. Environ.*, *49*, 85–92.

Hardisky, M., Gross, M. F., & Klemas, V. (1986). Remote Sensing of Coastal Wetlands. *BioScience, 36*(7), 453-460. doi:10.2307/1310341

Hartling, S., Sagan, V., Sidike, P., Maimaitijiang, M., & Carron, J. (2019). Urban tree species classification using a worldview-2/3 and lidar data fusion approach and Deep Learning. *Sensors*, *19*(6), 1284. https://doi.org/10.3390/s19061284

Haskins, J., Endris, C., Thomsen, A. S., Gerbl, F., Fountain, M. C., & Wasson, K. (2021). Uav to inform restoration: A case study from a california tidal marsh. *Frontiers in Environmental Science*, *9*. https://doi.org/10.3389/fenvs.2021.642906

Hinton, G., Deng, L., Yu, D., Dahl, G., Mohamed, A.-rahman, Jaitly, N., Senior, A., Vanhoucke, V., Nguyen, P., Sainath, T., & Kingsbury, B. (2012). Deep neural networks for acoustic

modeling in speech recognition: The shared views of four research groups. *IEEE Signal Processing Magazine*, *29*(6), 82–97. https://doi.org/10.1109/msp.2012.2205597

Hodgson, M. E.; Sella-Villa, D. (2021) State-level statutes governing unmanned aerial vehicle use in academic research in the United States. *International Journal of Remote Sensing*, *42*, 5366–5395.

Hong, S.-K., Koh, C.-H., Harris, R. R., Kim, J.-E., Lee, J.-S., & Ihm, B.-S. (2008). Land use in Korean tidal wetlands: Impacts and management strategies. *Environmental Management*, *45*(5), 1014–1026. https://doi.org/10.1007/s00267-006-0164-3

Hopkinson, C.; Chasmer, L.E.; Zsigovics, G.; Creed, I.F.; Sitar, M.; Treitz, P.; Maher, V. (2004). Errors in lidar ground elevation and wetland vegetation height estimates. *Int. Arch. Photogramm. Remote Sens. Spat. Inf. Sci.*, *36*, 108–113.

Huang, X., Wang, C., Li, Z., & Ning, H. (2020). A 100 m population grid in the CONUS by disaggregating census data with open-source Microsoft Building Footprints. *Big Earth Data*, *5*(1), 112–133. https://doi.org/10.1080/20964471.2020.1776200

Hugenholtz, C. H., Moorman, B. J., Riddell, K., & Whitehead, K. (2012). Small unmanned aircraft systems for Remote Sensing and earth science research. *Eos, Transactions American Geophysical Union*, *93*(25), 236–236. https://doi.org/10.1029/2012eo250005

Hugenholtz, C. H., Whitehead, K., Brown, O. W., Barchyn, T. E., Moorman, B. J., LeClair, A., Riddell, K., & Hamilton, T. (2013). Geomorphological mapping with a small unmanned aircraft system (SUAS): Feature Detection and Accuracy Assessment of a photogrammetrically-derived digital terrain model. *Geomorphology*, *194*, 16–24. https://doi.org/10.1016/j.geomorph.2013.03.023

Hunt, E.R.; Doraiswamy, P.C.; McMurtrey, J.E.; Daughtry, C.; Perry, E.M.; Akhmedov, B. (2013). A visible band index for remote sensing leaf chlorophyll content at the canopy scale. *Int. J. Appl. Earth Obs. Geoinf.*, *21*, 103–112, doi:10.1016/j.jag.2012.07.020.

Hänsch, R., Schulz, K., & Sörgel, U. (2018). Machine learning methods for Remote Sensing Applications: An overview. *Earth Resources and Environmental Remote Sensing/GIS Applications IX*. https://doi.org/10.1117/12.2503653

Jamali, A. (2019). A fit-for-purpose algorithm for environmental monitoring based on maximum likelihood, support vector machine and Random Forest. *The International Archives of the Photogrammetry, Remote Sensing and Spatial Information Sciences*, *XLII-3/W7*, 25–32. https://doi.org/10.5194/isprs-archives-xlii-3-w7-25-2019

James, G., Witten, D., Hastie, T., & Tibshirani, R. (2013). *An introduction to statistical learning: With applications in R*. Springer.

Jensen, J. R. (2016). *Introductory digital image processing: A remote sensing perspective*, 4th ed.; Pearson Education: Glenview, IL, USA.

Jensen, J. R. (2018). *Drone Aerial Photography and Videography: Data Collection and Image Interpretation* (Kindle ed.). Amazon Digital Services LLC.

Jensen, J. R., Cowen, D. J., Althausen, J. D., Narumalani, S., & Weatherbee, O. (1993). An Evaluation of the CoastWatch Change Detection Protocol in South Carolina. *Photogrammetric Engineering & Remote Sensing, 59*(6), 1039-1046.

Jensen, J. R., Coombs, C., Porter, D., Jones, B., Schill, S., & White, D. (1998). Extraction of smooth cordgrass(spartina alterniflora)biomass and leaf area index parameters from high resolution imagery. *Geocarto International*, *13*(4), 25–34. https://doi.org/10.1080/10106049809354661

Jensen, J. R., Olson, G., Schill, S. R., Porter, D. E., & Morris, J. (2002). Remote Sensing of Biomass, Leaf-Area-Index, and ChlorophyllaandbContent in the ACE Basin National Estuarine Research Reserve Using Sub-meter Digital Camera Imagery. *Geocarto International*, *17*(3), 27–36. https://doi.org/10.1080/10106040208542241

Jing, R., Gong, Z., Zhao, W., Pu, R., & Deng, L. (2017). Above-bottom biomass retrieval of aquatic plants with regression models and SfM data acquired by a UAV platform – A

case study in Wild Duck Lake Wetland, Beijing, China. *ISPRS Journal of Photogrammetry and Remote Sensing*, *134*, 122–134. https://doi.org/10.1016/j.isprsjprs.2017.11.002

Johnson, B. J., Manby, R., & Devine, G. J. (2020). Performance of an aerially applied liquid bacillus thuringiensis var. Israelensis formulation (strain AM65-52) against mosquitoes in mixed saltmarsh–mangrove systems and fine-scale mapping of Mangrove Canopy cover using affordable drone-based imagery. *Pest Management Science*, *76*(11), 3822–3831. https://doi.org/10.1002/ps.5933

Jozdani, S. E., Johnson, B. A., & Chen, D. (2019). Comparing deep neural networks, ensemble classifiers, and support vector machine algorithms for object-based urban land use/land cover classification. *Remote Sensing*, *11*(14), 1713. https://doi.org/10.3390/rs11141713

Kennish, M. J. (2002). Environmental threats and environmental future of Estuaries. *Environmental Conservation*, *29*(1), 78–107. https://doi.org/10.1017/s0376892902000061

Kirwan, M. L., & Megonigal, J. P. (2013). Tidal wetland stability in the face of human impacts and sea-level rise. *Nature*, *504*(7478), 53–60. https://doi.org/10.1038/nature12856

Kislik, C., Dronova, I., & Kelly, M. (2018). UAVs in support of algal BLOOM research: A review of current applications and future opportunities. *Drones*, *2*(4), 35. https://doi.org/10.3390/drones2040035

Klemas, V. (2013). Remote Sensing of Coastal Wetland Biomass: An Overview. *Journal of Coastal Research*, *290*, 1016–1028. https://doi.org/10.2112/jcoastres-d-12-00237.1

Klemas, V. V. (2015). Coastal and environmental remote sensing from Unmanned Aerial Vehicles: An overview. *Journal of Coastal Research*, *315*, 1260–1267. https://doi.org/10.2112/jcoastres-d-15-00005.1

Koh, L. P., & Wich, S. A. (2012). Dawn of Drone Ecology: Low-cost autonomous aerial vehicles for conservation. *Tropical Conservation Science*, *5*(2), 121–132. https://doi.org/10.1177/194008291200500202

Lang, M.W., Purkis, S., Klemas, V.V., & Tiner R.W. (2015). Promising Developments and Future Challenges for Remote Sensing of Wetlands. In *Remote Sensing of Wetlands: Applications and Advances* 1st ed.; R.W. Tiner, M.W. Lang & V.V. Klemas (Eds.); CRC Press, pp. 533-544.

Lary, D. J., Alavi, A. H., Gandomi, A. H., & Walker, A. L. (2016). Machine learning in geosciences and remote sensing. *Geoscience Frontiers*, *7*(1), 3–10. https://doi.org/10.1016/j.gsf.2015.07.003

Leahy, M. G., Jollineau, M. Y., Howarth, P. J., & Gillespie, A. R. (2005). The use of Landsat data for investigating the long-term trends in wetland change at Long Point, Ontario. *Canadian Journal of Remote Sensing, 31*(3), 240-254. doi:10.5589/m05-012

Li, H., Wang, C., Cui, Y., & Hodgson, M. (2021). Mapping salt marsh along coastal South Carolina using U-Net. *ISPRS Journal of Photogrammetry and Remote Sensing*, *179*, 121–132. https://doi.org/10.1016/j.isprsjprs.2021.07.011

Li, W., Fu, H., Yu, L., Gong, P., Feng, D., Li, C., & Clinton, N. (2016). Stacked autoencoder-based deep learning for remote-sensing image classification: A case study of african land-cover mapping. *International Journal of Remote Sensing*, *37*(23), 5632–5646. https://doi.org/10.1080/01431161.2016.1246775

Li, X., & Shao, G. (2014). Object-based land-cover mapping with high resolution aerial photography at a county scale in Midwestern USA. *Remote Sensing*, *6*(11), 11372–11390. https://doi.org/10.3390/rs61111372

Lishawa, S. C., Carson, B. D., Brandt, J. S., Tallant, J. M., Reo, N. J., Albert, D. A., Monks, A. M., Lautenbach, J. M., & Clark, E. (2017). Mechanical harvesting effectively controls

young typha spp. invasion and unmanned aerial vehicle data enhances post-treatment monitoring. *Frontiers in Plant Science*, *8*. https://doi.org/10.3389/fpls.2017.00619

Litjens, G., Kooi, T., Bejnordi, B. E., Setio, A. A., Ciompi, F., Ghafoorian, M., van der Laak, J. A. W. M., van Ginneken, B., & Sánchez, C. I. (2017). A survey on Deep Learning in medical image analysis. *Medical Image Analysis*, *42*, 60–88. https://doi.org/10.1016/j.media.2017.07.005

Liu, P., Choo, K.-K. R., Wang, L., & Huang, F. (2016). SVM or Deep Learning? A comparative study on Remote Sensing Image Classification. *Soft Computing*, *21*(23), 7053–7065. https://doi.org/10.1007/s00500-016-2247-2

Liu, S.; Hodgson, M. E. (2016) Satellite image collection modeling for large area hazard emergency response. *ISPRS Journal of Photogrammetry and Remote Sensing*, *118*, 13–21.

Liu, T., Abd-Elrahman, A., Morton, J., & Wilhelm, V. L. (2018). Comparing fully convolutional networks, random forest, support vector machine, and patch-based deep convolutional neural networks for object-based wetland mapping using images from small unmanned aircraft system. *GIScience & Remote Sensing*, *55*(2), 243–264. https://doi.org/10.1080/15481603.2018.1426091

Liu, Y., Chen, X., Wang, Z., Wang, Z. J., Ward, R. K., & Wang, X. (2018). Deep learning for pixel-level image fusion: Recent advances and future prospects. *Information Fusion*, *42*, 158–173. https://doi.org/10.1016/j.inffus.2017.10.007

Loomis, M. J., & Craft, C. B. (2010). Carbon Sequestration and Nutrient (Nitrogen, Phosphorus) Accumulation in River-Dominated Tidal Marshes, Georgia, USA. *Soil Science Society of America Journal*, *74*(3), 1028–1036. https://doi.org/10.2136/sssaj2009.0171

Ma, L., Liu, Y., Zhang, X., Ye, Y., Yin, G., & Johnson, B. A. (2019). Deep learning in remote sensing applications: A Meta-analysis and Review. *ISPRS Journal of Photogrammetry and Remote Sensing*, *152*, 166–177. https://doi.org/10.1016/j.isprsjprs.2019.04.015

Mahdianpari, M., Rezaee, M., Zhang, Y., & Salehi, B. (2018). Wetland classification using Deep Convolutional Neural Network. *IGARSS 2018 - 2018 IEEE International Geoscience and Remote Sensing Symposium*. https://doi.org/10.1109/igarss.2018.8517919

Maimaitijiang, M., Sagan, V., Sidike, P., Maimaitiyiming, M., Hartling, S., Peterson, K. T., Maw, M. J. W., Shakoor, N., Mockler, T., & Fritschi, F. B. (2019). Vegetation Index Weighted Canopy Volume Model (CVMVI) for soybean biomass estimation from Unmanned Aerial System-based RGB imagery. *ISPRS Journal of Photogrammetry and Remote Sensing*, *151*, 27–41. https://doi.org/10.1016/j.isprsjprs.2019.03.003

Marcaccio, J. V., Markle, C. E., & Chow-Fraser, P. (2016). Use of fixed-wing and multi-rotor unmanned aerial vehicles to map dynamic changes in a freshwater marsh. *Journal of Unmanned Vehicle Systems*, *4*(3), 193–202. https://doi.org/10.1139/juvs-2015-0016

Maxwell, A. E., Warner, T. A., & Fang, F. (2018). Implementation of machine-learning classification in Remote Sensing: An applied review. *International Journal of Remote Sensing*, *39*(9), 2784–2817. https://doi.org/10.1080/01431161.2018.1433343

McGlinchy, J., Johnson, B., Muller, B., Joseph, M., & Diaz, J. (2019). Application of unet fully convolutional neural network to impervious surface segmentation in urban environment from high resolution satellite imagery. *IGARSS 2019 - 2019 IEEE International Geoscience and Remote Sensing Symposium*. https://doi.org/10.1109/igarss.2019.8900453

Mehvar, S., Filatova, T., Dastgheib, A., de Ruyter van Steveninck, E., & Ranasinghe, R. (2018). Quantifying economic value of coastal ecosystem services: A review. *Journal of Marine Science and Engineering*, *6*(1), 5. https://doi.org/10.3390/jmse6010005

Meng, X., Shang, N., Zhang, X., Li, C., Zhao, K., Qiu, X., & Weeks, E. (2017). Photogrammetric UAV mapping of terrain under Dense Coastal Vegetation: An Object-Oriented Classification Ensemble algorithm for classification and Terrain Correction. *Remote Sensing*, *9*(11), 1187. https://doi.org/10.3390/rs9111187

Michez, A., Bauwens, S., Brostaux, Y., Hiel, M.-P., Garré, S., Lejeune, P., & Dumont, B. (2018). How Far Can Consumer-Grade UAV RGB Imagery Describe Crop Production? A 3D and Multitemporal Modeling Approach Applied to Zea mays. *Remote Sensing*, *10*(11), 1798. https://doi.org/10.3390/rs10111798

Microsoft. (n.d.). *Microsoft/USBUILDINGFOOTPRINTS: Computer generated building footprints for the United States*. GitHub. Retrieved November 20, 2021, from https://github.com/Microsoft/USBuildingFootprints

Miller, G. J., Morris, J. T., & Wang, C. (2019). Estimating Aboveground Biomass and Its Spatial Distribution in Coastal Wetlands Utilizing Planet Multispectral Imagery. *Remote Sensing*, *11*(17), 2020. https://doi.org/10.3390/rs11172020

Minchinton, T. E. (2002). Disturbance by wrack facilitates spread of Phragmites australis in a Coastal Marsh. *Journal of Experimental Marine Biology and Ecology*, *281*(1-2), 89–107. https://doi.org/10.1016/s0022-0981(02)00438-0

Mo, Y., Kearney, M. S., & Turner, R. E. (2019). Feedback of coastal marshes to climate change: Long-term phenological shifts. *Ecology and Evolution, 9*(12), 6785-6797. doi:10.1002/ece3.5215

Montemayor, D. I., Canepuccia, A. D., Farina, J., Addino, M., Valiñas, M., & Iribarne, O. O. (2019). Effects of Spartina wrack on surface-active arthropod assemblage under different environmental contexts in southwest Atlantic Salt Marshes. *Estuaries and Coasts*, *42*(4), 1104–1126. https://doi.org/10.1007/s12237-018-00509-7

Morgan, G. R., & Hodgson, M. E. (2021). A Post-Classification Change Detection Model with Confidences in High Resolution Multi-Date sUAS Imagery in Coastal South Carolina. *International Journal of Remote Sensing*, *42*(11), 4309–4336. https://doi.org/10.1080/01431161.2021.1890266

Morgan, G. R., Wang, C., & Morris, J. T. (2021). RGB indices and canopy height modelling for mapping tidal marsh biomass from a small unmanned aerial system. *Remote Sensing*, *13*(17), 3406. https://doi.org/10.3390/rs13173406

Morganello, K., & Rose, L. (2013, November 23). Life Along the Salt Marsh: Protecting Tidal Creeks with Vegetative Buffers. Retrieved February 02, 2021, from https://hgic.clemson.edu/factsheet/life-along-the-salt-marsh-protecting-tidal-creeks-with-vegetative-buffers/

Morris, J. T., & Haskin, B. (1990). A 5-yr Record of Aerial Primary Production and Stand Characteristics of Spartina Alterniflora. *Ecology*, *71*(6), 2209–2217. https://doi.org/10.2307/1938633

Morris, J. T., Porter, D., Neet, M., Noble, P. A., Schmidt, L., Lapine, L. A., & Jensen, J. R. (2005). Integrating LIDAR elevation data, multi-spectral imagery and neural network modelling for marsh characterization. *International Journal of Remote Sensing*, *26*(23), 5221–5234. https://doi.org/10.1080/01431160500219018

Morris, J.; Sundberg, K. (2021) Environmental Data Initiative. LTREB: Aboveground Biomass, Plant Density, Annual Aboveground Productivity, and Plant Heights in Control and Fertilized Plots in a Spartina Alterniflora-Dominated Salt Marsh, North Inlet, Georgetown, SC: 1984–2020. Ver 5. Available online: https://doi.org/10.6073/pasta/5d94cd77d20121090c72bb81154ac302 (Accessed on 8 July 2021).

Mountrakis, G., Im, J., & Ogole, C. (2011). Support Vector Machines in remote sensing: A Review. *ISPRS Journal of Photogrammetry and Remote Sensing*, *66*(3), 247–259. https://doi.org/10.1016/j.isprsjprs.2010.11.001

Narayan, S., Beck, M. W., Wilson, P., Thomas, C. J., Guerrero, A., Shepard, C. C., Reguero, B. G., Franco, G., Ingram, J. C., & Trespalacios, D. (2017). The value of coastal wetlands

for flood damage reduction in the northeastern usa. *Scientific Reports*, *7*(1). https://doi.org/10.1038/s41598-017-09269-z

Negrin, V. L., Trilla, G. G., Kandus, P., & Marcovecchio, J. E. (2012). Decomposition and nutrient dynamics in a Spartina alterniflora marsh of the Bahia Blanca Estuary, Argentina. *Brazilian Journal of Oceanography*, *60*(2), 259–263. https://doi.org/10.1590/s1679-87592012000200016

Nijhawan, R., Sharma, H., Sahni, H., & Batra, A. (2017). A deep learning hybrid CNN framework approach for vegetation cover mapping using deep features. *2017 13th International Conference on Signal-Image Technology & Internet-Based Systems (SITIS)*. https://doi.org/10.1109/sitis.2017.41

Otukei, J. R., & Blaschke, T. (2010). Land cover change assessment using decision trees, support vector machines and maximum likelihood classification algorithms. *International Journal of Applied Earth Observation and Geoinformation*, *12*. https://doi.org/10.1016/j.jag.2009.11.002

Ouyang, Z.-T., Zhang, M.-Q., Xie, X., Shen, Q., Guo, H.-Q., & Zhao, B. (2011). A comparison of pixel-based and object-oriented approaches to VHR imagery for mapping saltmarsh plants. *Ecological Informatics*, *6*(2), 136–146. https://doi.org/10.1016/j.ecoinf.2011.01.002

O'Donnell, J., & Schalles, J. (2016). Examination of abiotic drivers and their influence on Spartina alterniflora biomass over a twenty-eight year period using Landsat 5 TM satellite imagery of the central Georgia coast. *Remote Sensing*, *8*(6), 477. https://doi.org/10.3390/rs8060477

Pal, M. (2005). Random forest classifier for remote sensing classification. *International Journal of Remote Sensing*, *26*(1), 217–222. https://doi.org/10.1080/01431160412331269698

Pal, M., & Mather, P. M. (2005). Support vector machines for classification in remote sensing. *International Journal of Remote Sensing*, *26*(5), 1007–1011. https://doi.org/10.1080/01431160512331314083

Pashaei, M., Kamangir, H., Starek, M. J., & Tissot, P. (2020). Review and Evaluation of Deep Learning Architectures for Efficient Land Cover Mapping with UAS Hyper-Spatial Imagery: A Case Study Over a Wetland. *Remote Sensing, 12*(6), 959. doi:10.3390/rs12060959

Pennings, S. C., & Richards, C. L. (1998). Effects of wrack burial in salt-stressed habitats: Batis maritima in a southwest Atlantic Salt Marsh. *Ecography*, *21*(6), 630–638. https://doi.org/10.1111/j.1600-0587.1998.tb00556.x

Peterson, G. W., & Turner, R. E. (1994). The value of salt Marsh edge vs interior as a habitat for fish AND decapod crustaceans in a Louisiana tidal marsh. *Estuaries*, *17*(1), 235. https://doi.org/10.2307/1352573

Peña, J., Gutiérrez, P., Hervás-Martínez, C., Six, J., Plant, R., & López-Granados, F. (2014). Object-based image classification of summer crops with machine learning methods. *Remote Sensing*, *6*(6), 5019–5041. https://doi.org/10.3390/rs6065019

Phinn, S.R. (1998). A framework for selecting appropriate remotely sensed data dimensions for environmental monitoring and management. *International Journal of Remote Sensing, 19,* 3457 3463.

Pinton, D., Canestrelli, A., & Fantuzzi, L. (2020). A UAV-based dye-tracking technique to measure Surface Velocities Over Tidal channels and salt marshes. *Journal of Marine Science and Engineering*, *8*(5), 364. https://doi.org/10.3390/jmse8050364

Pinton, D., Canestrelli, A., Wilkinson, B., Ifju, P., & Ortega, A. (2020). A new algorithm for estimating ground elevation and vegetation characteristics in coastal salt marshes from high-resolution uav-based lidar point clouds. *Earth Surface Processes and Landforms*, *45*(14), 3687–3701. https://doi.org/10.1002/esp.4992

Pix4D. (2016, April 20). *Improved accuracy for rolling shutter cameras*. Pix4D. Retrieved January 3, 2022, from https://www.pix4d.com/blog/rolling-shutter-correction

Platt, W. J., Joseph, D., & Ellair, D. P. (2014). Hurricane Wrack generates landscape-level heterogeneity in coastal Pine Savanna. *Ecography*, *38*(1), 63–73. https://doi.org/10.1111/ecog.00731

Poley, L., & J. McDermid, G. (2020). A Systematic Review of the Factors Influencing the Estimation of Vegetation Aboveground Biomass Using Unmanned Aerial Systems. *Remote Sensing*, *12*(7), 1052. https://doi.org/10.3390/rs12071052

Port Royal Sound. Available online: https://www.lowcountryinstitute.org/prs (accessed on 20 Nov 2021).

Possoch, M., Bieker, S., Hoffmeister, D., Bolten, A., Schellberg, J., & Bareth, G. (2016). Multi-temporal Crop Surface Models Combined with the RGB Vegetation Index from UAV-based Images for Forage Monitoring in Grassland. *ISPRS - International Archives of the Photogrammetry, Remote Sensing and Spatial Information Sciences*, *XLI-B1*, 991–998. https://doi.org/10.5194/isprsarchives-xli-b1-991-2016

Pouliot, D., Latifovic, R., Pasher, J., & Duffe, J. (2019). Assessment of Convolution Neural Networks for Wetland Mapping with Landsat in the Central Canadian Boreal Forest Region. *Remote Sensing, 11*(7), 772. doi:10.3390/rs11070772

Purcell, A. D., Khanal, P., Straka, T., & Willis, D. B. (2020). Valuing ecosystem services of coastal marshes and wetlands. *Land-Grant Press by Clemson Extension*. https://doi.org/10.34068/report4

Ramsey III, E., & Rangoonwala, A. (2015). Radar and Optical Image Fusion and Mapping of Wetland Resources. In *Remote Sensing of Wetlands: Applications and Advances* 1st ed.; R.W. Tiner, M.W. Lang & V.V. Klemas (Eds.); CRC Press, pp. 155-174.

Reidenbaugh, T. G., & Banta, W. C. (1980). Origins and effects of Spartina Wrack in a virginia salt marsh. *Gulf Research Reports*, *6*. https://doi.org/10.18785/grr.0604.07

Rhee, D. S., Kim, Y. D., Kang, B., & Kim, D. (2017). Applications of unmanned aerial vehicles in fluvial remote sensing: An overview of recent achievements. *KSCE Journal of Civil Engineering*, *22*(2), 588–602. https://doi.org/10.1007/s12205-017-1862-5

Ridge, J. T., & Johnston, D. W. (2020). Unoccupied aircraft Systems (uas) for marine ecosystem restoration. *Frontiers in Marine Science*, *7*. https://doi.org/10.3389/fmars.2020.00438

Rimal, B., Rijal, S., & Kunwar, R. (2019). Comparing support vector machines and maximum likelihood classifiers for mapping of urbanization. *Journal of the Indian Society of Remote Sensing*, *48*(1), 71–79. https://doi.org/10.1007/s12524-019-01056-9

Rogers, J. N., Parrish, C. E., Ward, L. G., & Burdick, D. M. (2016). Assessment of Elevation Uncertainty in Salt Marsh Environments using Discrete-Return and Full-Waveform Lidar. *Journal of Coastal Research*, *76*, 107–122. https://doi.org/10.2112/si76-010

Ronneberger, O., Fischer, P., & Brox, T. (2015). U-Net: Convolutional Networks for Biomedical Image Segmentation. *Lecture Notes in Computer Science*, 234–241. https://doi.org/10.1007/978-3-319-24574-4_28

Rupasinghe, P. A., & Chow-Fraser, P. (2019). Identification of most Spectrally Distinguishable Phenological stage of Invasive Phragmites australis in Lake Erie Wetlands (Canada) for accurate mapping Using multispectral satellite imagery. *Wetlands Ecology and Management*, *27*(4), 513–538. https://doi.org/10.1007/s11273-019-09675-2

Rupasinghe, P. A., Simic Milas, A., Arend, K., Simonson, M. A., Mayer, C., & Mackey, S. (2018). Classification of shoreline vegetation in the Western basin of Lake Erie using Airborne Hyperspectral Imager HSI2, Pleiades and UAV data. *International Journal of Remote Sensing*, *40*(8), 3008–3028. https://doi.org/10.1080/01431161.2018.1539267

Samiappan, S., Turnage, G., Hathcock, L. A., & Moorhead, R. (2016). Mapping of invasive Phragmites (common reed) in Gulf of Mexico coastal wetlands Using Multispectral imagery and small unmanned aerial systems. *International Journal of Remote Sensing*, *38*(8-10), 2861–2882. https://doi.org/10.1080/01431161.2016.1271480

Sanger, D., Blair, A., DiDonato, G., Washburn, T., Jones, S., Riekerk, G., Wirth, E., Stewart, J., White, D., Vandiver, L., & Holland, A. F. (2013). Impacts of coastal development on the ecology of Tidal Creek ecosystems of the US southeast including consequences to humans. *Estuaries and Coasts*, *38*(S1), 49–66. https://doi.org/10.1007/s12237-013-9635-y

Santos Santana, L., Araújo E Silva Ferraz, G., Bedin Marin, D., Dienevam Souza Barbosa, B., Mendes Dos Santos, L., Ferreira Ponciano Ferraz, P., Conti, L., Camiciottoli, S., & Rossi, G. (2021). Influence of flight altitude and control points in the georeferencing of images obtained by Unmanned Aerial Vehicle. *European Journal of Remote Sensing*, *54*(1), 59–71. https://doi.org/10.1080/22797254.2020.1845104

SCDHEC. (2019). The South Carolina Coastal Zone Management Program. Retrieved January 21, 2022, from https://scdhec.gov/environment/your-water-coast/ocean-coastal-resource-management/coastal-zone-management/south

Schill, S. R., & Jensen, J. R. (2000). Predicting the impact of coastal development on water quality using remote sensing and gis-assisted hydrologic modeling techniques. *Geocarto International*, *15*(4), 7–16. https://doi.org/10.1080/10106040008542168

Sea Level Rise Adaptation Report Beaufort County, South Carolina. (2015) *SC Sea Grant Consortium Product #SCSGC-T-15-02*.

Shang, X., & Chisholm, L. A. (2014). Classification of Australian native forest species using hyperspectral remote sensing and machine-learning classification algorithms. *IEEE Journal of Selected Topics in Applied Earth Observations and Remote Sensing*, *7*(6), 2481–2489. https://doi.org/10.1109/jstars.2013.2282166

Stalter, R., Jung, A., Starosta, A., Baden, J., & Byer, M. D. (2006). Effect of wrack accumulation on salt marsh vegetation, Baruch Institute, Georgetown County, South Carolina. *WIT Transactions on Ecology and the Environment, Vol 88*. https://doi.org/10.2495/cenv060291

Stary, K.; Jelinek, Z.; Kumhalova, J.; Chyba, J.; Balazova, K. (2020). Comparing RGB—Based vegetation indices from UAV imageries to estimate hops canopy area. *Agron. Res.*, *18*, 2592–2601.

State wetland protection: Status, trends and model approaches. A 50-state study. (2008). Washington (DC): Environmental Law Institute. [accessed 2022 January 5]. https://www.eli.org/sites/default/files/docs/core_states/South_Carolina.pdf

Taddia, Y., Pellegrinelli, A., Corbau, C., Franchi, G., Staver, L. W., Stevenson, J. C., & Nardin, W. (2021). High-Resolution monitoring of TIDAL systems Using uav: A case study on Poplar Island, md (usa). *Remote Sensing*, *13*(7), 1364. https://doi.org/10.3390/rs13071364

Tait, L., Bind, J., Charan-Dixon, H., Hawes, I., Pirker, J., & Schiel, D. (2019). Unmanned aerial Vehicles (UAVs) for Monitoring Macroalgal Biodiversity: Comparison of RGB and Multispectral imaging sensors for Biodiversity Assessments. *Remote Sensing*, *11*(19), 2332. https://doi.org/10.3390/rs11192332

Terwilliger, B., Vincenzi, D., & Ison, D. (2015). Unmanned aerial systems: Collaborative Innovation to support emergency response. *Journal of Unmanned Vehicle Systems*, *3*(2), 31–34. https://doi.org/10.1139/juvs-2015-0004

Thorne, K., MacDonald, G., Guntenspergen, G., Ambrose, R., Buffington, K., Dugger, B., Freeman, C., Janousek, C., Brown, L., Rosencranz, J., Holmquist, J., Smol, J., Hargan, K., & Takekawa, J. (2018). U.S. Pacific coastal wetland resilience and vulnerability to sea-level rise. *Science Advances*, *4*(2). https://doi.org/10.1126/sciadv.aao3270

Tiner, R. W., Lang, M. W., & Klemas, V. (2015). *Remote sensing of wetlands: Applications and advances*. CRC Press.

Tiner, R.W. (2015) Introduction to Wetland Mapping and Its Challenges. In *Remote Sensing of Wetlands: Applications and Advances* 1st ed.; R.W. Tiner, M.W. Lang & V.V. Klemas (Eds.); CRC Press, pp. 43-65.

Tolley, P. M., & Christian, R. R. (1999). Effects of increased inundation and wrack deposition on a high salt marsh plant community. *Estuaries*, *22*(4), 944. https://doi.org/10.2307/1353074

Topodrone. (2020, March). *Correction of the rolling shutter distortion and processing survey data from Topodrone DJI Mavic 2 pro L1/L2 RTK/PPK*. Topodrone. Retrieved January 3, 2022, from https://topodrone.org/news/article/rolling-shutter-distortion-correction/

Train random trees classifier (spatial analyst). Train Random Trees Classifier (Spatial Analyst)-ArcGIS Pro | Documentation. (n.d.). Retrieved November 20, 2021, from https://pro.arcgis.com/en/pro-app/latest/tool-reference/spatial-analyst/train-random-trees-classifier.htm

Train Support Vector Machine classifier (spatial analyst). Train Support Vector Machine Classifier (Spatial Analyst)-ArcGIS Pro | Documentation. (n.d.). Retrieved November 20, 2021, from https://pro.arcgis.com/en/pro-app/latest/tool-reference/spatial-analyst/train-support-vector-machine-classifier.htm

U.S. Census Bureau. QuickFacts: Beaufort County, South Carolina. Available online: https://www.census.gov/quickfacts/beaufortcountysouthcarolina (accessed on 20 Nov 2021).

Valiela, I., & Rietsma, C. S. (1995). Disturbance of salt marsh vegetation by wrack mats in Great Sippewissett Marsh. *Oecologia*, *102*(1), 106–112. https://doi.org/10.1007/bf00333317

Van Stan, J. T., Allen, S. T., Swanson, T., Skinner, M., & Gordon, D. A. (2020). Wrack and ruin: Legacy hydrologic effects of hurricane-deposited wrack on hardwood-hammock coastal islands. *Environmental Research Communications*, *2*(6), 061001. https://doi.org/10.1088/2515-7620/ab9527

Viehman, S., Vander Pluym, J. L., & Schellinger, J. (2011). Characterization of marine debris in North Carolina Salt Marshes. *Marine Pollution Bulletin*, *62*(12), 2771–2779. https://doi.org/10.1016/j.marpolbul.2011.09.010

Wan, J., & Ma, Y. (2020). Multi-scale spectral-spatial remote sensing classification of coral reef habitats using CNN-SVM. *Journal of Coastal Research*, *102*(sp1). https://doi.org/10.2112/si102-002.1

Wang, C. (2021). At-sensor radiometric correction of a multispectral camera (RedEdge) for SUAS vegetation mapping. *Sensors*, *21*(24), 8224. https://doi.org/10.3390/s21248224

Wang, C., Morgan, G., & Hodgson, M. E. (2021). sUAS for 3D Tree Surveying: Comparative Experiments on a Closed-Canopy Earthen Dam. *Forests*, *12*(6), 659. https://doi.org/10.3390/f12060659

Wedge, M., Anderson, C. J., & DeVries, D. (2015). Evaluating the effects of urban land use on the condition of resident salt marsh fish. *Estuaries and Coasts*, *38*(6), 2355–2365. https://doi.org/10.1007/s12237-015-9942-6

Westoby, M. J., Brasington, J., Glasser, N. F., Hambrey, M. J., & Reynolds, J. M. (2012). 'Structure-from-Motion' photogrammetry: A low-cost, effective tool for geoscience applications. *Geomorphology*, *179*, 300–314. https://doi.org/10.1016/j.geomorph.2012.08.021

White, L., Ryerson, R. A., Pasher, J., & Duffe, J. (2020). State of science assessment of remote sensing of great lakes coastal wetlands: Responding to an operational requirement. *Remote Sensing*, *12*(18), 3024. https://doi.org/10.3390/rs12183024

Whiteside, T. G., Boggs, G. S., & Maier, S. W. (2011). Comparing object-based and pixel-based classifications for mapping savannas. *International Journal of Applied Earth Observation and Geoinformation*, *13*(6), 884–893. https://doi.org/10.1016/j.jag.2011.06.008

Willis, D.B.; Straka T.J. (2016) The economic contribution of natural resources to South Carolina's economy. *Bulletin FW 13*. Clemson, SC: Clemson University Experiment Station.

Woebbecke, D.M.; Meyer, G.E.; Von Bargen, K.; Mortensen, D.A. (1995). Color Indices for Weed Identification Under Various Soil, Residue, and Lighting Conditions. *Trans. ASAE, 38*, 259–269, doi:10.13031/2013.27838.

Wyngaard, J., Barbieri, L., Thomer, A., Adams, J., Sullivan, D., Crosby, C., Parr, C., Klump, J., Raj Shrestha, S., & Bell, T. (2019). Emergent Challenges for Science sUAS Data Management: Fairness through Community Engagement and Best Practices Development. *Remote Sensing*, *11*(15), 1797. https://doi.org/10.3390/rs11151797

Yin, Z., Ling, F., Foody, G. M., Li, X., & Du, Y. (2020). Cloud detection in Landsat-8 imagery in Google Earth Engine based on a deep convolutional neural network. *Remote Sensing Letters, 11*(12), 1181-1190. doi:10.1080/2150704x.2020.1833096

Yue, J., Yang, G., Li, C., Li, Z., Wang, Y., Feng, H., & Xu, B. (2017). Estimation of Winter Wheat Above-Ground Biomass Using Unmanned Aerial Vehicle-Based Snapshot Hyperspectral Sensor and Crop Height Improved Models. *Remote Sensing*, *9*(7), 708. https://doi.org/10.3390/rs9070708

Zhang, M., Ustin, S. L., Rejmankova, E., & Sanderson, E. W. (1997). Monitoring Pacific Coast Salt Marshes using Remote Sensing. *Ecological Applications*, *7*(3), 1039–1053. https://doi.org/10.1890/1051-0761(1997)007[1039:mpcsmu]2.0.co;2

Zhang, W., Tang, P., & Zhao, L. (2021). Fast and accurate land-cover classification on medium-resolution remote-sensing images using segmentation models. *International Journal of Remote Sensing*, *42*(9), 3277–3301. https://doi.org/10.1080/01431161.2020.1871094

Zhou, Z., Yang, Y., & Chen, B. (2018). Estimating Spartina alterniflora fractional vegetation cover and aboveground biomass in a coastal wetland using Spot6 satellite and UAV Data. *Aquatic Botany*, *144*, 38–45. https://doi.org/10.1016/j.aquabot.2017.10.004

Zhu, X. X., Tuia, D., Mou, L., Xia, G.-S., Zhang, L., Xu, F., & Fraundorfer, F. (2017). Deep learning in remote sensing: A comprehensive review and list of resources. *IEEE Geoscience and Remote Sensing Magazine*, *5*(4), 8–36. https://doi.org/10.1109/mgrs.2017.2762307

APPENDIX A

MANUSCRIPT COPYRIGHT RELEASE

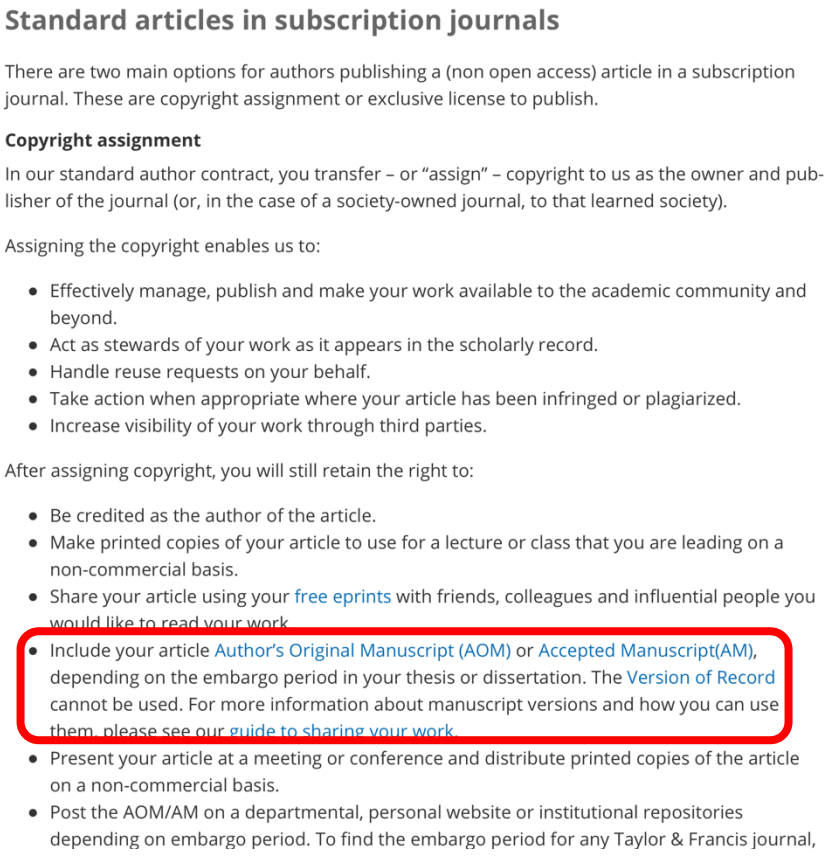

Standard articles in subscription journals

There are two main options for authors publishing a (non open access) article in a subscription journal. These are copyright assignment or exclusive license to publish.

Copyright assignment

In our standard author contract, you transfer – or "assign" – copyright to us as the owner and publisher of the journal (or, in the case of a society-owned journal, to that learned society).

Assigning the copyright enables us to:

- Effectively manage, publish and make your work available to the academic community and beyond.
- Act as stewards of your work as it appears in the scholarly record.
- Handle reuse requests on your behalf.
- Take action when appropriate where your article has been infringed or plagiarized.
- Increase visibility of your work through third parties.

After assigning copyright, you will still retain the right to:

- Be credited as the author of the article.
- Make printed copies of your article to use for a lecture or class that you are leading on a non-commercial basis.
- Share your article using your free eprints with friends, colleagues and influential people you would like to read your work.
- Include your article Author's Original Manuscript (AOM) or Accepted Manuscript(AM), depending on the embargo period in your thesis or dissertation. The Version of Record cannot be used. For more information about manuscript versions and how you can use them, please see our guide to sharing your work.
- Present your article at a meeting or conference and distribute printed copies of the article on a non-commercial basis.
- Post the AOM/AM on a departmental, personal website or institutional repositories depending on embargo period. To find the embargo period for any Taylor & Francis journal,

Figure A.1 Screenshot of Copyright Clearance from *Annals of GIS. This is an Accepted Manuscript of an article published by Taylor & Francis in Annals of GIS on January 17, 2022, available online: https://www.tandfonline.com/doi/full/10.1080/19475683.2022.2026476.*

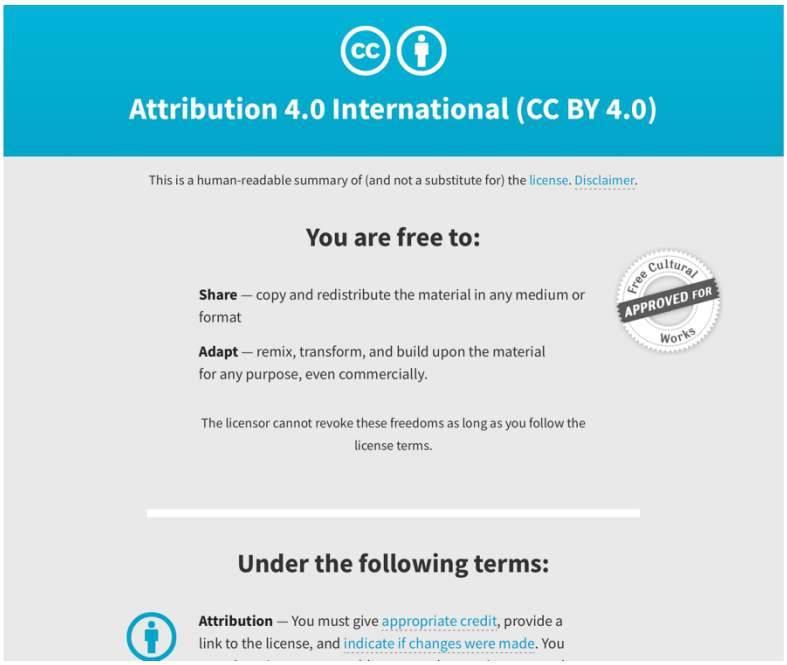

Figure A.2 Screenshot of Copyright Clearance from *Remote Sensing* due to the use of the CC BY 4.0 license.

Figure A.3 Screenshot of Copyright clearance from International Journal of Geo-Information from the use of the CC BY 4.0 license.